

## **INFORMATION TO USERS**

This manuscript has been reproduced from the microfilm master. UMI films the text directly from the original or copy submitted. Thus, some thesis and dissertation copies are in typewriter face, while others may be from any type of computer printer.

**The quality of this reproduction is dependent upon the quality of the copy submitted.** Broken or indistinct print, colored or poor quality illustrations and photographs, print bleedthrough, substandard margins, and improper alignment can adversely affect reproduction.

In the unlikely event that the author did not send UMI a complete manuscript and there are missing pages, these will be noted. Also, if unauthorized copyright material had to be removed, a note will indicate the deletion.

Oversize materials (e.g., maps, drawings, charts) are reproduced by sectioning the original, beginning at the upper left-hand corner and continuing from left to right in equal sections with small overlaps. Each original is also photographed in one exposure and is included in reduced form at the back of the book.

Photographs included in the original manuscript have been reproduced xerographically in this copy. Higher quality 6" x 9" black and white photographic prints are available for any photographs or illustrations appearing in this copy for an additional charge. Contact UMI directly to order.

**UMI**

A Bell & Howell Information Company  
300 North Zeeb Road, Ann Arbor MI 48106-1346 USA  
313/761-4700 800/521-0600



**UNIVERSITY OF MIAMI**

**GEOPHYSICAL APPLICATIONS OF THE GLOBAL POSITIONING SYSTEM**

**By**

**Ailin Mao**

**A DISSERTATION**

**Submitted to the Faculty  
of the University of Miami  
in partial fulfillment of the requirements for  
the degree of Doctor of Philosophy**

**Coral Gables, Florida**

**June 1998**

**UMI Number: 9905018**

---

**UMI Microform 9905018  
Copyright 1998, by UMI Company. All rights reserved.**

**This microform edition is protected against unauthorized  
copying under Title 17, United States Code.**

---

**UMI**  
300 North Zeeb Road  
Ann Arbor, MI 48103

UNIVERSITY OF MIAMI

A dissertation submitted in partial fulfillment of  
The requirements for the degree of  
Doctor of Philosophy

GEOPHYSICAL APPLICATIONS OF THE GLOBAL POSITIONING SYSTEM

Ailin Mao

Approved:



Dr. Timothy H. Dixon  
Professor of Marine  
Geology and Geophysics



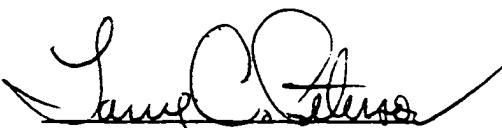
Dr. Steven G. Ullmann  
Interim Dean of the Graduate School



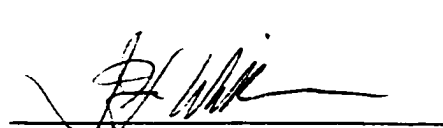
Dr. Christopher G. A. Harrison  
Professor of Marine  
Geology and Geophysics



Dr. Julie A. Hood  
Assistant Professor of  
Marine Geology and Geophysics



Dr. Larry C. Peterson  
Associate Professor of  
Marine Geology and Geophysics



Dr. Jorge F. Willemsen  
Professor of Applied  
Marine Physics

MAO, AILIN

(Ph.D., Marine Geology and Geophysics)

Geophysical Applications of the Global Positioning System

(June 1998)

Abstract of a doctoral dissertation at the University of Miami.

Dissertation supervised by Professor Timothy H. Dixon.

No. of pages in text 149.

Observation of land surface motions plays a critical role in the study of a wide range of geophysical phenomena. The Global Positioning System (GPS), designed by the US Department of Defense for military and civilian navigation and positioning, has been used to measure crustal motion. The ever expanding global network of GPS sites improves both temporal and spatial resolution of geophysical phenomena.

I assess the noise characteristics in time series of daily position estimates for 23 GPS stations with three years of data, using spectral analysis and Maximum Likelihood Estimation. A combination of white plus flicker noise can be used to model the noise characteristics of all three position components. Both white and flicker noise amplitudes are smallest in the north component and largest in the vertical component. The white noise part of the vertical component is higher for tropical stations ( $\pm 23^\circ$  latitude) compared to mid-latitude stations, which may be related to high wet tropospheric path delay and/or higher variability. Velocity error in the coordinate time series may be underestimated by factors of 5-11 if a pure white noise model is assumed.

I analyze data from 20 permanent GPS stations broadly distributed through the interior of the North American plate, and use the resulting velocities to estimate an Euler vector describing motion of "stable" North America as a single rigid plate. The site velocities fit the single plate model with a mean residual of 1.3 mm/yr. The residuals do

not appear to reflect post-glacial rebound, and tests for differential motion between eastern and western North America at the New Madrid seismic zone show no resolvable motion within uncertainties. The residuals more likely reflect observational error, and thus our estimate of the stability of the plate interior is likely an upper bound. In addition, I found that GPS velocity errors estimated with the white plus flicker noise model fit the observations significantly better than a pure white noise model.

Although the "Wilson cycle", in which continents rift apart to form new ocean basins which later close, is a vital feature of plate tectonics, the dynamics of rifting are poorly understood. Many of our ideas about continental rifting come from the best present example, the East African Rift, that separates East Africa (Somalia) from West Africa (Nubia). It is not clear whether the rift is failing, and will ultimately leave a fossil rift like those common in the geologic record, or whether it will succeed in splitting Africa into two plates separated by an ocean. To study this issue, we inverted space geodetic data to estimate an Euler vector describing relative motion between Nubia and Somalia. The Euler vector predicts extension directed between E-W and WNW-ESE at rates of 5-7 mm/yr, considerably higher than geologic estimates averaged over tens of millions of years. The rate of extension appears to have accelerated since 5-6 million years ago, when motion of the African plate changed.

To my mother.

獻給我的母亲。

## Acknowledgments

First of all, I would like to give my sincere thanks to my advisor Professor Timothy H. Dixon and his wife Jackie. Without their encouragement and great patience, it would be impossible for me to have survived the five years of Ph.D. study and life in the new world. What I learned from them is far beyond scientific research. Their good understanding and enjoyment of different cultures are impressive. I feel sorry that I am still not a frequent bar-goer as Tim expected.

During my dissertation work, members of the dissertation committee were always so helpful. Whenever I went to them with questions, they always provided me with their insightful advice on the problems I ran into. Especially, I like to thank Professor Chris Harrison for his tremendous advice and discussion. He always made my view of science harmonious.

Many people have helped me in various areas from English to Geology. Zandong Ding, Fred Farina, Edmundo Norabuena, Michael Finny, Carlos Alvarez, Phil Kramer, Hongzhi Wang, Teri Vallamor and Avis Miller in MGG division deserve my thanks. Dr. Don McNeil gave me much help in building my geological knowledge during the first two years of study. I enjoyed the time working with Lisa Leffler, John Weber and Andrew Newman from Northwestern University, and Giovanni Sella from Louisiana State University. Professor Seth Stein from Northwestern University, Dr. Jeff Freymueller from the University of Alaska, Dr. John Langbein from the USGS, Dr. Chuck DeMets from the University of Wisconsin, Dr. Hadley Johnson and Dr. Jie Zhang from the University of

California, San Diego, kindly shared their professional expertise. The GPS data analysis group in NASA Jet Propulsion Laboratory gave me a lot of assistance in using the sophisticated GPS data analysis software - GIPSY.

A lot of my old friends kept giving me great support and sympathy in the last five years. Hou Jinliang, Chengli Huang and Zhang Zhongping in Shanghai Astronomical Observatory helped me take care of my family and brought me invaluable messages from my home in China. I also enjoyed the time I spent with my Chinese folks here, which made me feel closer to my hometown.

Finally, I owe special thanks to my family: my parents, my brother Airong Mao and my wife Dan Ying. My mom is a typical Chinese woman who sacrifices everything to her children. We have a saying in Chinese: "Do not travel far away from where your parents live". I am sorry I am so far away when my parents need my care. I am definitely not a good son under the Chinese traditions. I owe too much to my wife, who had to leave her hometown, travel a long way to join me, and endure life in the totally new world.

## Table of Contents

<b>Chapter 1</b>	<b>Introduction and Background .....</b>	1
1.1	The Global Positioning System and its Geophysical Applications .....	1
1.2	This Research .....	2
1.3	GPS Background .....	4
1.4	GPS Observables and Estimation of Station Positions .....	7
1.5	Signals and Noise in GPS Observations .....	10
1.5.1	Satellite Orbits .....	10
1.5.2	Signal Propagation .....	11
1.5.3	Clocks in Satellites and Receivers .....	15
1.5.4	Ambiguity Resolution and Cycle Slips .....	15
1.5.5	Multipath and Variations of Antenna Phase Center .....	17
1.5.6	Modeling the Site Motions .....	19
1.5.7	Reference Frames for GPS Data Analysis .....	20
<b>Chapter 2</b>	<b>GPS Data Analysis .....</b>	22
2.1	GPS Data Collection and Analysis at UM/RSMAS Geodesy Lab .....	22
2.1.1	Overview of GPS Applications and Data Collection at UM/RSMAS Geodesy Lab .....	22
2.1.2	Data Analysis with GIPSY Software .....	25
2.1.3	Analysis Strategy .....	26
2.1.4	Precise Orbits and Point Positioning .....	28
2.2	Defining the GPS Results in the International Terrestrial Reference Frame .....	30
2.2.1	Introduction .....	30
2.2.2	International Terrestrial Reference Frame .....	31
2.2.3	No-Fiducial GPS Data Analysis .....	32
2.2.4	Helmert Transformation of Cartesian Coordinate Systems .....	34
2.2.5	Estimation of Site Velocities in ITRF from No-Fiducial Solutions .....	37
2.3	Postprocessing .....	39
<b>Chapter 3: Noise in GPS Time Series .....</b>	40	
3.1	Introduction .....	40
3.2	Data Analysis .....	43
3.2.1	Spectral Analysis .....	43
3.2.2	Maximum Likelihood Estimation .....	52
3.3	Results and Discussion .....	55
3.3.1	Spectral Index and Noise Amplitude .....	55
3.3.2	Regional and Other Correlations .....	70
3.3.3	Effect of Time Correlated Noise on Velocity Estimation .....	71
3.4	Conclusions .....	75

<b>Chapter 4: Rigidity of the Interior North America Plate .....</b>	<b>76</b>
4.1    Introduction .....	76
4.2    Data Analysis .....	78
4.2.1    Site Velocity and Accuracy Evaluation .....	78
4.2.2    Estimation of Plate Motion and Regional Deformation .....	86
4.2.3 <i>F</i> -Test of Splitting a One-Plate Model into a Two-Plate Model	89
4.2.4    Corrections of Site Velocities for Postglacial Rebound .....	90
4.3    Results .....	92
4.3.1    Overall Rigidity of the North American Plate Interior .....	94
4.3.2    Predicted Relative Motion at New Madrid Seismic Zone .....	113
4.4    Conclusions .....	118
<b>Chapter 5: Present-Day Motion across the East African Rift .....</b>	<b>120</b>
5.1    Introduction .....	120
5.2    Relative Motion Derived from Space Geodetic Measurements .....	121
5.3    Discussion and Conclusions .....	126
<b>Chapter 6: Future Directions and Summary .....</b>	<b>131</b>
6.1    Prospects for Observing Absolute Sea Level Change and Coastal Subsidence with GPS .....	131
6.1.1    Absolute Sea Level Change .....	131
6.1.2    Coastal Land Subsidence in the Mississippi Delta Area .....	133
6.1.3    Preliminary Results from GPS Network for Measurement of Absolute Sea Level Change and Coastal Subsidence .....	134
6.2    Summary .....	138
<b>Appendix: Acronyms .....</b>	<b>140</b>
<b>References .....</b>	<b>141</b>
<b>Vita</b>	

## List of Figures

Figure 1.1	Diagram shows the positioning concept of GPS, the signal and noise in pseudorange observations, and the GPS geophysical applications.	8
Figure 2.1	Two GPS time series are generated routinely at the Geodesy Lab. One uses precise orbits from JPL and includes reference sites (or optional sites if primary sites are not available) and sites of geologic interest. The other uses reference frame sites and additional sites to estimate the orbits along with site positions for near real-time analysis (mainly for volcano monitoring). Numbered boxes show the locations of some projects in which I have been involved - see text for details.	23
Figure 3.1	Distribution of GPS stations used in this study. ....	42
Figure 3.2	Power spectrum computed from complete time series (solid line) compared with spectrum computed with 30% of data are randomly removed. Data are 73 years of monthly mean tide gauge data from Boston. An annual and semi-annual term stand out above the noise. Frequency is in cycles/year. ....	50
Figure 3.3	GPS coordinate time series used in this study. Abscissa is CE years - 1900. Ordinate is north, east and vertical components (offset by a nominal value) in mm. ....	58
Figure 3.4	Power spectra of the GPS time series shown in Figure 3.3. $\alpha$ is estimated spectral index. Abscissa is period in days. Ordinate is in $\text{mm}^2$ . ....	61
Figure 3.5	White noise vs. flicker noise amplitude for the 23 GPS time series. ..	68
Figure 3.6	Comparison of spectral index ( $\alpha$ ) and amplitude of white and flicker noise computed for 3 year time series (this study) and 6 year time series [Heflin, 1997] for sites where both are available. Solid line has slope of 1.00. 1- $\sigma$ error bars are also shown in figures. ....	69
Figure 3.7	White and flicker noise as a function of latitude. ....	71

<b>Figure 3.8</b>	Velocity errors for time series with different lengths or sampling intervals. In addition to time series of pure white noise, flicker noise and random walk noise, the table also shows the best case ( $\sigma_w = \pm 3\text{mm}$ and $\sigma_f = \pm 5\text{mm}$ ) and worst case ( $\sigma_w = \pm 3\text{mm}$ , $\sigma_f = \pm 5\text{mm}$ and $\sigma_{rw} = \pm 2\text{mm}/\sqrt{\text{yr}}$ ) based on Table 3.5 and <i>Langbein and Johnson [1997]</i> . .....	73
<b>Figure 4.1</b>	Stations used in this study, their GPS-derived velocities in ITRF96 and 95% confidence ellipses. Major tectonic features discussed in text are also shown. RGR is Rio Grande Rift; NMSZ in New Madrid Seismic Zone. Note general rotation of sites about an Euler pole in northwestern South America (Figure 4.11). .....	78
<b>Figure 4.2</b>	GPS coordinate time series used in this study. The horizontal axes are CE years - 1900. The vertical axes are east and north components (offset by a nominal value) in mm. .....	82
<b>Figure 4.3</b>	Velocity residuals and 95% confidence error ellipses from estimation scheme 0. WES2 is shown for comparison only. .....	98
<b>Figure 4.4</b>	Velocity residuals and 95% confidence error ellipses from estimation scheme 1. WES2 is shown for comparison only. Major tectonic features are described in Figure 4.1. .....	101
<b>Figure 4.5</b>	Velocity residuals and 95% confidence error ellipses from estimation scheme 2. Major tectonic features are described in Figure 4.1. .....	103
<b>Figure 4.6</b>	Velocity residuals and 95% confidence error ellipses from estimation scheme 3. Major tectonic features are described in Figure 4.1. .....	105
<b>Figure 4.7</b>	Velocity residuals and 95% confidence error ellipses from estimation scheme 4. Major tectonic features are described in Figure 4.1. .....	107
<b>Figure 4.8</b>	Velocity residuals and 95% confidence error ellipses from estimation scheme 5. Major tectonic features are described in Figure 4.1. .....	109
<b>Figure 4.9</b>	Correlation between predicted PGR motions and GPS velocity residuals without PGR corrections, based on 12 sites for which we have PGR velocity predictions. .....	110
<b>Figure 4.10</b>	Velocity residuals and 95% confidence error ellipses from estimation scheme 6. Major tectonic features are described in Figure 4.1. .....	111

Figure 4.11	Euler pole positions and 39% error ellipses (one standard error) derived from different noise models and site sets. Estimation schemes are described in Table 4.3. ....	112
Figure 4.12	Euler pole positions and 95% error ellipses for eastern and western North America Relative to ITRF96. Estimation schemes are described in Table 4.11. ....	116
Figure 4.13	Predicted relative velocity and 95% error ellipses at New Madrid Seismic Zone (West relative to East). Numbers indicate the estimation schemes detailed in Table 4.11 and Table 4.3. ....	118
Figure 5.1	Topography, shallow seismicity (<50 km, $M \geq 3.0$ , red dots) and lithospheric plates within and adjacent to Africa, and location of space geodetic sites used in this study. Predicted motion and error ellipse (one standard error) for Somalia relative to Nubia from space geodesy are shown at three locations along the East African Rift, outlined by high topography and diffuse seismicity. ....	124
Figure 5.2	Comparison of extension rates and azimuths across the East African Rift, predicted from this study (present) and <i>Chu's</i> [1995] model (0-3 Ma). Error bars are one standard deviations. ....	127
Figure 5.3	Extension rate across the East African Rift near the equator as a function of time. Data from <i>Hendrie et al.</i> [1994] (5-25 Ma; 0-5 Ma), <i>Chu</i> [1995] (0-3 Ma), and this study (present day). Vertical bars represent one standard error for rate estimate, horizontal bars represent averaging period. Vertical arrows show (right) time of change in absolute motion of African plate (6 Ma) [ <i>Pollitz</i> , 1991] and (left) age of earliest known bipedal hominid (4.2 Ma) [ <i>Leakey et al.</i> , 1995]. ....	129
Figure 6.1	GPS sites and tide gauges in the Southeastern U.S. ....	135

## List of Tables

<b>Table 1.1</b>	<b>Navstar GPS Constellation Status .....</b>	<b>5</b>
<b>Table 3.1</b>	<b>Test Results of Spectral Analysis on Synthetic Time Series .....</b>	<b>51</b>
<b>Table 3.2</b>	<b>Station Description .....</b>	<b>56</b>
<b>Table 3.3</b>	<b>Station Time Series: Length and Spectral Index Estimates .....</b>	<b>57</b>
<b>Table 3.4</b>	<b>Log Maximum Likelihood for Three Noise Models .....</b>	<b>65</b>
<b>Table 3.5</b>	<b>Noise Amplitude (mm) .....</b>	<b>67</b>
<b>Table 3.6</b>	<b>Velocity Error Estimates for White and White plus Flicker Noise Models (mm/yr) .....</b>	<b>74</b>
<b>Table 4.1</b>	<b>Site Description for the Data Period .....</b>	<b>77</b>
<b>Table 4.2</b>	<b>North, East and Vertical GPS Site Velocities and Errors (mm/yr, ITRF96) .....</b>	<b>93</b>
<b>Table 4.3a</b>	<b>Description of Estimation Schemes .....</b>	<b>95</b>
<b>Table 4.3b</b>	<b>Euler Vectors for North America Relative to ITRF96 .....</b>	<b>96</b>
<b>Table 4.4</b>	<b>Predicted and Residual Site Velocities from Estimation Scheme 0 (mm/yr) .....</b>	<b>97</b>
<b>Table 4.5</b>	<b>Predicted and Residual Site Velocities from Estimation Scheme 1 (mm/yr) .....</b>	<b>100</b>
<b>Table 4.6</b>	<b>Predicted and Residual Site Velocities from Estimation Scheme 2 (mm/yr) .....</b>	<b>102</b>
<b>Table 4.7</b>	<b>Predicted and Residual Site Velocities from Estimation Scheme 3 (mm/yr) .....</b>	<b>104</b>
<b>Table 4.8</b>	<b>Predicted and Residual Site Velocities from Estimation Scheme 4 (mm/yr) .....</b>	<b>106</b>
<b>Table 4.9</b>	<b>Predicted and Residual Site Velocities from Estimation Scheme 5 (mm/yr) .....</b>	<b>108</b>

<b>Table 4.10</b>	<b>Predicted and Residual Site Velocities from Estimation Scheme 6 (mm/yr) .....</b>	<b>111</b>
<b>Table 4.11</b>	<b>Euler Vectors for Eastern and Western North America Relative to ITRF96 .....</b>	<b>115</b>
<b>Table 4.12</b>	<b>Predicted Relative Velocity at New Madrid Seismic Zone (West relative to East) .....</b>	<b>117</b>
<b>Table 5.1</b>	<b>Site Velocities (ITRF-96, mm/yr) .....</b>	<b>122</b>
<b>Table 5.2</b>	<b>Euler Vectors Describing Relative Motion Between Nubia and Somalia .....</b>	<b>124</b>
<b>Table 5.3</b>	<b>Predicted Motions across the Rift (Somalia Relative to Nubia) (mm/yr) .....</b>	<b>124</b>
<b>Table 6.1</b>	<b>North, East and Vertical Velocities and Errors of Permanent GPS Sites .....</b>	<b>136</b>
<b>Table 6.2</b>	<b>Site Positions and Errors Estimated from GPS measurements in 1997</b>	<b>137</b>

## **CHAPTER 1      Introduction and Background**

### **1.1    The Global Positioning System and its Geophysical Applications**

Observations of land surface motions play a critical role in the study of a wide range of geophysical phenomena. Previously, traditional triangulation, trilateration and leveling were used to measure crustal motion. These techniques are usually limited to small regions, and suffer from low accuracy if extended to larger areas. Such measurements are also labor intensive. Beginning in the 1970's, Very Long Baseline Interferometry (VLBI) and Satellite Laser Ranging (SLR) provide three dimensional positions with centimeter to millimeter precision over a global scale. VLBI measures the difference of arrival times of signals from extra-terrestrial radio sources at two or more radio telescopes, while SLR measures the light travel time or distance between a SLR station and an earth-orbiting satellite. Because they require large facilities and are relatively costly, only a limited number of such stations have been established around the world.

The Global Positioning System (GPS), designed by the US Department of Defense for military and civilian navigation and positioning, makes it possible for a user with a portable, relatively inexpensive receiver to obtain a three-dimensional position estimate accurate to about one centimeter with a single day of observation. GPS observations can be made under all weather conditions, and do not require intervisibility between sites, which makes site selection very flexible. The ever decreasing receiver cost

makes it accessible to a great number of research groups, and has enabled a large global network of permanent sites to be established. The increasing density of sites has enormous impact. It increases the accuracy of the satellite orbit determinations, refines the global terrestrial reference frame, and improves both temporal and spatial resolution of geophysical phenomena. GPS measurements have been used to investigate plate motion [*Argus and Heflin, 1995; Larson & Freymueller, 1997; Dixon and Mao, 1997b*], plate boundary zone deformation [*Dixon et al., 1996; Norabuena et al., 1998*], deformation around active volcanoes [*Dixon et al., 1997a*], preseismic, coseismic and postseismic deformation [*Wdowinski et al., 1997*], and Post Glacial Rebound (PGR). When combined with tide gauge data, GPS can also be used to monitor global sea level change.

## 1.2 This Research

In this chapter, I briefly summarize my research goals, and review the background of the Global Positioning System, its observables, and the signals and noise in GPS observables, especially for high precision applications. Chapter 2 describes the GPS data analysis strategies and procedures I developed at the UM/RSMAS (The University of Miami, Rosenstiel School of Marine and Atmospheric Sciences) Geodesy Lab. A key result is the way in which results are transferred to a stable and accurate global reference frame.

Chapter 3 discusses the noise properties of GPS time series. Geophysical studies using geodetic measurements of the surface velocity or strain field require not only

accurate estimates of these parameters, but also accurate error estimates in order to assess statistical significance. Analysis of GPS noise is important for evaluation and improvement of GPS measurement accuracy. Spectral analysis and Maximum Likelihood Estimation are used to characterize the noise. After the magnitudes of white noise and time-correlated noise are estimated, I investigate the impact of time-correlated noise on estimation of velocity errors. Because of the nature and magnitude of time-correlated noise, it will take a much longer time than we initially expected to achieve the requisite accuracy for some applications, such as global sea level change.

Chapter 4 discusses the rigidity of the interior North American plate based on GPS measurements. This chapter follows our previously published research [*Dixon et al., 1996*] with more data and improved analysis methods. We use 20 sites on the interior of North America to see if there is significant relative motion on a continental scale, a possible explanation for seismicity in the New Madrid Seismic Zone, the site of very large earthquakes in 1811-1812. I will show that a single rigid plate model adequately explains the current GPS data. The measured residual velocities more likely reflect observational errors rather than intraplate motion; thus continental scale motion cannot explain New Madrid seismicity, unless such motion is below our detection limit (about 1 mm/yr).

Chapter 5 shows the present-day motion across the East African Rift. The East African Rift is the Earth's longest active continental rift. The diffuse nature of the rift zone makes it difficult to measure the relative motion across the rift. The relative motion is not constrained by the most recent plate motion models such as NUVEL-1 [*DeMets et*

*al.*, 1990]. Because only four GPS sites have adequate data on the African plate, other space geodetic data (VLBI, SLR and DORIS) are also used in this investigation. I show that the extension rate predicted from space geodetic data is considerably higher than geologic estimates averaged over tens of millions of years.

Chapter 6 summarizes results to date of our GPS networks for tide gauge calibration and coastal subsidence investigation. Because of the short time span of measurements (all sites less than 3 years) and noise levels (Chapter 3), I report only the data, without interpretation, for most sites.

### **1.3 GPS Background**

GPS is a satellite-based radio navigation system. The full constellation of GPS consists of 21 satellites plus three active spares, which are placed in six almost circular orbits, with an orbital inclination of 55 degrees and a semi-major axis of about 26,600 km. The orbit period is exactly 12 hours of sidereal time. With the completion of the 24-satellite constellation in July 1992, three-dimensional positioning capacity was extended to virtually all parts of the globe. At least four satellite are simultaneously visible above the horizon anywhere on the earth at any time. New generation GPS satellites (Block IIR, which started to replace the old satellites in 1997) can cross-range with each other, which will greatly improve GPS orbit determination.

Table 1.1 Navstar GPS Constellation Status

Blk II Seq #	SVN	PRN Code	Orbit Plane	Launch Date	Clock	Available	Decommissioned
<i>Block I</i>							
-	01	04	-	78-02-22	-	78-03-29	85-07-17
-	02	07	-	78-05-13	-	78-07-14	81-07-16
-	03	06	-	78-10-06	-	78-11-13	92-05-18
-	04	08	-	78-12-10	-	79-01-08	89-10-14
-	05	05	-	80-02-09	-	80-02-27	83-11-28
-	06	09	-	80-04-26	-	80-05-16	91-03-06
-	07	-	-	81-12-18	Launch failure		
-	08	11	-	83-07-14	-	83-08-10	93-05-04
-	09	13	-	84-06-13	-	84-07-19	94-06-20
-	10	12	-	84-09-08	-	84-10-03	95-11-18
-	11	03	-	85-10-09	-	85-10-30	94-04-13
<i>Block II</i>							
II-1	14	14	E-1	89-02-14	Cs	89-04-15	
II-2	13	02	B-3	89-06-10	Cs	89-08-10	
II-3	16	16	E-5	89-08-18	Cs	89-10-14	
II-4	19	19	A-4	89-10-21	Rb	89-11-23	
II-5	17	17	D-3	89-12-11	Cs	90-01-06	
II-6	18	18	F-3	90-01-24	Cs	90-02-14	
II-7	20	20	-	90-03-26	-	90-04-18	96-05-10
II-8	21	21	E-2	90-08-02	Cs	90-08-22	
II-9	15	15	D-2	90-10-01	Cs	90-10-15	
<i>Block IIA</i>							
II-10	23	23	E-4	90-11-26	Cs	90-12-10	
II-11	24	24	D-1	91-07-04	Rb	91-08-30	
II-12	25	25	A-2	92-02-23	Cs	92-03-24	
II-13	28	28	-	92-04-10	-	92-04-25	97-05
II-14	26	26	F-2	92-07-07	Cs	92-07-23	
II-15	27	27	A-3	92-09-09	Cs	92-09-30	
II-16	32	01	F-1	92-11-22	Cs	92-12-11	
II-17	29	29	F-4	92-12-18	Rb	93-01-05	
II-18	22	22	B-1	93-02-03	Cs	93-04-04	
II-19	31	31	C-3	93-03-30	Cs	93-04-13	
II-20	37	07	C-4	93-05-13	Cs	93-06-12	
II-21	39	09	A-1	93-06-26	Cs	93-07-20	
II-22	35	05	B-4	93-08-30	Cs	93-09-28	
II-23	34	04	D-4	93-10-26	Cs	93-11-22	
II-24	36	06	C-1	94-03-10	Cs	94-03-28	
II-25	33	03	C-2	96-03-28	Cs	96-04-09	
II-26	40	10	E-3	96-07-16	Cs	96-08-15	
II-27	30	30	B-2	96-09-12	Cs	96-10-01	
II-28	38	08	A-5	97-11-06			
<i>Block IIR</i>							
IIR-1	42	12	-	97-01-17	Launch failure		
IIR-2	43	13	F-5	97-07-23	Rb		

1. As of November 06, 1997. SVN refers to space vehicle number; PRN refers to unique pseudorandom noise code of satellite.
2. No orbital plane position = satellite no longer operational.
3. Clock: Rb = Rubidium; Cs = Cesium.
4. Selective Availability (S/A) was enabled on Block II satellites during part of 1990; S/A off between about 10 August 1990 and 1 July 1991 due to the Gulf crisis; standard level re-implemented on 15 November 1991; occasionally off for test and other purposes. Currently, PRN15 appears to have little or no S/A imposed.
5. Anti-spoofing (A-S) was activated on 94-01-31 at 00:00 UT on all Block II satellites; occasionally off for test and other purposes.
6. PRN number of SVN32 was changed from 32 to 01 on 93-01-28.
7. PRN31's active clock was switched from a rubidium clock to a cesium clock on 23 July 1997.
8. From *Langley* [1997].

GPS satellites transmit two carrier frequencies, L<sub>1</sub> ( $f = 1575.42$  MHz,  $\lambda = 19.05$  cm ), L<sub>2</sub> ( $f = 1227.60$  MHz,  $\lambda = 24.45$  cm ), which are modulated by the navigation signals (pseudo random noise) and the navigation and system data (satellite health, ephemerides, and other housekeeping information). The L<sub>1</sub> carrier is modulated with the precise P-code ( $f = 10.23$  MHz,  $\lambda = 29.31$  m) and the less precise C/A-code ( $f = 1.023$  MHz,  $\lambda = 293.1$  m), while the L<sub>2</sub> carrier is modulated only with P-code. Navigation messages are also broadcasted on L<sub>1</sub>.

The primary goal of GPS is real-time navigation for military forces with meter level accuracy, which is mainly limited by uncertainties in clocks, orbits, and atmospheric effects. High-precision geodetic measurements have been made by post-processing carrier phase measurements with differential techniques and/or the use of a global GPS tracking network. With improved satellite parameters estimated by post-processing data from global GPS sites, high precision is also achievable with point positioning techniques. The International GPS Service for Geodynamics (IGS), which

became operational on January 1, 1994, supports GPS geodesy with a global network of permanent GPS stations, data archive and analysis centers. High-accuracy GPS ephemerides (orbits), satellite clock information and other products are routinely available within several days after data acquisition [*Kouba and Mireault, 1997; Jefferson et al., 1997*].

#### **1.4 GPS Observables and Estimation of Station Positions**

The fundamental observable of GPS is the signal travel time from the satellite antenna to the receiver antenna, obtained by measuring the difference between the transmit ( $T_s$ ) and receive ( $T_r$ ) times. The range  $R$  is obtained through the knowledge of the light speed ( $c$ ) in vacuum,  $R = c(T_r - T_s)$ . Errors in receiver or satellite clocks are present in the range estimate  $R$ , which for this reason is referred to as pseudorange.

$$R = |X_r - X_s| + c(dT_r - dT_s + dT_p) + e \quad (1.1)$$

Where  $dT_r$  is the receiver clock offset from a reference clock,  $dT_s$  is the satellite clock offset,  $dT_p$  is the delay associated with propagation, mainly due to the atmosphere and ionosphere,  $X_r$  and  $X_s$  are positions of receiver and satellite in the geocentric inertial coordinate, and  $e$  is the observation error. Figure 1.1 shows the positioning concept of GPS.

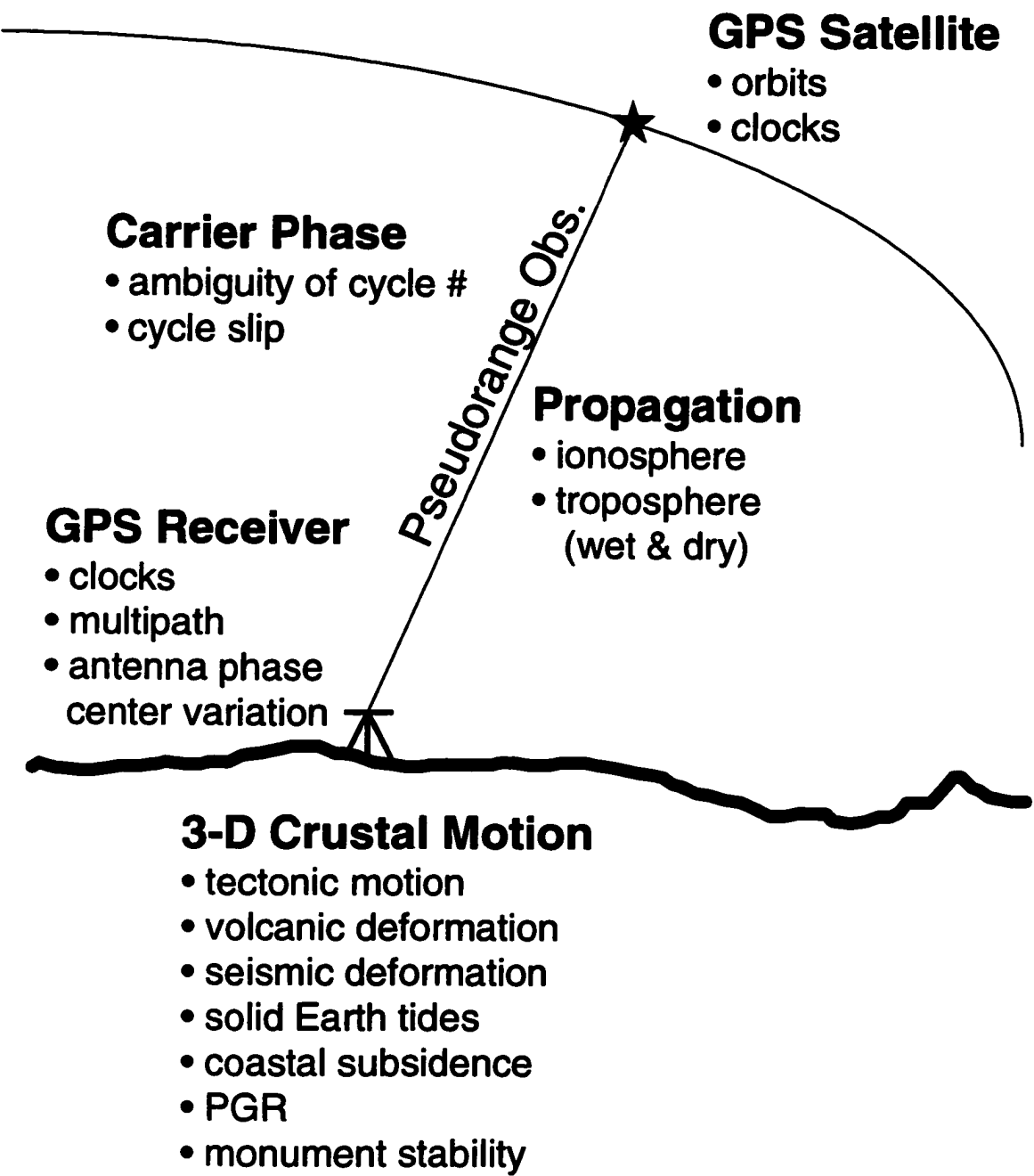


Figure 1.1 Diagram shows the positioning concept of GPS, the signal and noise in pseudorange observations, and the GPS geophysical applications.

The signal travel time can be determined by correlating the C/A (Coarse Code) or P-code (Precise Code) sequence, generated in the receiver, and the code sequence received from the satellite. Measurements obtained with C/A or P-code are usually called pseudorange. It is also possible to obtain distance information through phase measurements on the carrier signal itself by keeping track of the cycle number after signal acquisition.

$$R = |X_r - X_s| + c(dT_r - dT_s + dT_p) + n\lambda + e \quad (1.2)$$

Although the phase measurements have ambiguities in the initial integer number of wavelengths, and cycle slips which are caused by discontinuities of phase tracking, it is much more precise than a pseudorange measurement, because of its short wavelength. The carrier phase can be recovered by code-correlating when code information is available. When P-code is unavailable (e.g., under Anti-Spoofing policy), one of the techniques to recover L<sub>2</sub> carrier phase is signal squaring, which reduces effective wavelength to half, making cycle ambiguity resolution of the carrier phase more difficult. The most recent method is to cross-correlate carrier phase L<sub>2</sub> with L<sub>1</sub>, assuming P-code on L<sub>1</sub> and L<sub>2</sub> are identical [Seeber, 1993]. In either method, the overall signal-to-noise ratio (SNR) of phase observations is reduced.

Security features on GPS have complicated civilian applications. "Selective Availability" (S/A) policy reduces the accuracy of the broadcast ephemeris with pseudo-random noise, and dithers the clock frequency. Although the frequency dithering

introduces noise to the carrier phase measurements, S/A does not have a serious impact on high-precision geodetic applications with differencing techniques or the global tracking network. The effect can be completely removed in differential operation, if observations are made at exactly identical observation epochs, implying that synchronization is critical. The US government has stated that the use of S/A is to be discontinued within the next decade. "Anti-Spoofing" (A-S) guards against jamming (fake transmissions of GPS data) by encrypting the P-code to form Y-code. It was officially implemented on January 31, 1994. Under A-S policy, most receivers have no P-code observations, which makes it more difficult to recover the carrier phase on L<sub>2</sub> frequency and to resolve integer phase ambiguity.

## 1.5 Signals and Noise in GPS Observation

Here we describe various signals or noises in GPS observables as shown in equation (1.2). The separation of signal and noise is relative, depending on the particular research interest or application.

### 1.5.1 Satellite Orbits

Satellite orbits can be described with six parameters (initial position and velocity in a Cartesian coordinate, or equivalently six Keplerian elements) and a force model to define the time evolution. The following gravitational forces are modeled: (1) point mass gravity due to the Earth, Sun, and Moon, (2) oblateness of the Earth and lower degree

spherical harmonic term of the Earth's gravitational field, (3) solid Earth tides due to the Sun and Moon, (4) ocean tides, and (5) pole tide.

Since the GPS satellite solar panels have a large ratio of surface area to mass, solar radiation pressure produces significant acceleration. Normal models usually estimate solar radiation pressure and Y-bias due to thermal imbalance and solar panel misalignment along with orbit parameters. The accuracy of orbit modeling may degrade when satellites pass through the Earth's shadow periodically during the eclipse season, two months every year, because there are unpredictable yaw variations when the satellites lose their sun sensors. Such yaw bias can be modeled and estimated in data analysis [Bar-Server *et al.*, 1996]. Atmospheric drag can be neglected because of the GPS satellites' high altitude.

### 1.5.2 Signal Propagation

#### *Ionosphere*

The propagation delay in the ionosphere (between about 50 km and 1000 km above the Earth's surface) depends on the electron content, frequency, geographic location, and time. For GPS frequencies, the resulting range error can vary from less than 1 meter to several tens of meters and is approximately proportional to  $1/f^2$ . Dual frequency receivers make use of the fact that the L1 and L2 signals experience different propagation delays in the ionosphere and thus can eliminate the major ionosphere effect.

An ionosphere-free phase observable ( $L_c$ ) can be formed from the linear combinations of phase observations on both frequencies ( $L_1, L_2$ ).

$$L_c = \frac{f_1^2 L_1 - f_2^2 L_2}{f_1^2 - f_2^2} \cong 2.5457 L_1 - 1.5457 L_2 \quad (1.3)$$

The effective wavelength of  $L_c$  is about 10.7 cm. Only the second order term is considered in equation (1.3). Neglecting the third- and higher-order terms in equation (1.3) causes several millimeters error, and can reach a few centimeters in extreme conditions. Because the ionosphere is a dispersive medium, the phase velocity (propagation of the carrier) is not the same as the group velocity (propagation of the C/A code or P-code). The ionospheric delay corrections for both observations have the same magnitude, but negative for phase observation and positive for code observation.

Because  $L_c$  is noisier than  $L_1$  or  $L_2$ , single frequency measurements are better for very short baselines (a few kilometers or less) where ionospheric effects are small. For single-frequency receivers, an attempt can be made to use an ionospheric correction model, whose coefficients are transmitted by GPS satellites. Most part of the remaining errors are canceled out by differencing between two sites over a short baseline (<10km) [Seaber, 1993].

### *Neutral Troposphere*

Tropospheric delay has wet and dry components. They are not dispersive at GPS carrier frequencies, so cannot be eliminated with dual-frequency observations. The atmospheric propagation delay  $dT_a$  is often expressed as the sum of two terms

$$dT_a(\varepsilon) = dT_d^z m_d(\varepsilon) + dT_w^z m_w(\varepsilon) \quad (1.4)$$

where  $dT_a$  is dependent on elevation angle  $\varepsilon$ , but not on azimuth,  $dT_d$  and  $dT_w$  are dry and wet zenith delay, respectively, while  $m_d$  and  $m_w$  are the mapping functions which map the zenith delay to other elevations, and are assumed to be known. The difference of various mapping functions developed by different authors is small for elevations above 10 degrees.

The dry component is about 2 meters at zenith, and varies slowly and smoothly (since it is largely determined by air pressure, and observable by surface pressure measurement). Atmospheric water vapor causes the wet component, typically in the range of about 5-25 cm at zenith, but it has random variations over a broad spatial and temporal scale (since the variations are related to turbulence). Maximal delays resulting from dry gradients are about 10-20 times larger than those from wet gradients [Dixon and Kornreich Wolf, 1990]. The wet delay is more critical when site distances are larger (>50km), or when the height differences are large, as in mountainous regions, because the local atmospheric conditions are no longer sufficiently correlated with one another. Usually, the dry zenith delay is estimated from surface pressure or assigned a nominal value. The remaining residual dry zenith delay and wet zenith delay are estimated in the

GPS data analysis with site positions and other parameters. Estimation of zenith delays from GPS data weakens the solutions of vertical components because of the correlation between these parameters and the vertical site coordinates. It is important to model these delays accurately, especially for the estimation of vertical station coordinates. However, adequate modeling still remains difficult; the wet delay is considered to be one of the most poorly controlled GPS error sources.

Alternatively, we can constrain the zenith delay to values determined by surface meteorological instruments or water vapor radiometers (WVRs). Analyses of various experiments have demonstrated that estimation of a zenith delay bias as a random walk process (e.g., a first-order Gauss-Markov process) has produced comparable results to using a WVR in a variety of regions [Dixon *et al.*, 1991b]. However, new generation WVRs are capable of significantly improving vertical component estimates [Ware *et al.*, 1997]

Sinusoidal azimuthal variations in the atmospheric propagation delay have been determined from VLBI data [Chen and Herring, 1997]. The delay due to atmospheric azimuthal asymmetry can be expressed as

$$\Delta T_{az}(\epsilon, \alpha) = \Delta T_{ns} m_{az}(\epsilon) \cos \alpha + \Delta T_{ew} m_{az}(\epsilon) \sin \alpha \quad (1.5)$$

where  $\Delta T_{ns}$ ,  $\Delta T_{ew}$  are gradient coefficients to be estimated,  $m_{az}(\epsilon)$  is a mapping function, and  $\alpha$  is the azimuth in which the observation is made. For sites in mid latitude, north-south gradient effects have average values up to 20 mm of delay at 10° elevation over

periods of months, but no significant mean east-west gradients were found [Chen and Herring, 1997]. Such azimuthal gradients can cause about 2 mm change in the north component of site positions. Modeling the atmospheric azimuthal asymmetry is more important when observations at lower elevation angle are used. For current GPS measurements with elevation cut-off of 15 degrees, the asymmetrical effects are smaller.

Because GPS signals are delayed as they pass through the earth's atmosphere, GPS observations have been used to measure the water vapor content in the atmosphere [Dixon and Kornreich Wolf, 1990; Rocken et al., 1997].

### 1.5.3 Clocks in Satellites and Receivers

Most GPS satellites carry high-quality rubidium or cesium frequency standards, while a receiver might employ a quartz oscillator with less frequency stability. But S/A policy reduces the apparent accuracy of satellite clocks in terms of the signal broadcast to civilian users. The stability of a clock is characterized with Allen variance [Dixon, 1991a] over a time interval. Clock bias can be estimated along with other unknowns from GPS data. The well-known double-difference method of eliminating clock bias allows efficient computation of the least-squares geodetic solution. But it may be difficult to form double difference over long baselines.

### 1.5.4 Ambiguity Resolution and Cycle Slips

Ambiguity resolution refers to the determination of an integer-cycle bias for each set of carrier phase measurements as shown in equation (1.2), and is essential for the best

achievable precision and accuracy. For short baselines, people used to first estimate carrier phase biases as real-valued parameters, then hold these fixed to integer values; hence the term "bias-fixing". For ambiguity resolution over long baselines, a sufficiently long arc of data and accurate modeling of the phase observables are critical. In addition, the ambiguities of the L<sub>1</sub> and L<sub>2</sub> phase are perfectly correlated. Pseudorange observations or ionospheric constraints (or both) can be used to constrain phase ambiguities. One of the approaches uses pseudorange data to resolve the "widelane" ambiguity (referring to the phase difference between L<sub>1</sub> and L<sub>2</sub> channels with longer wave length). This method of "widelaning" is model-independent, and can resolve ambiguities on baselines up to about 1000 km [Blewitt, 1989]. Without the availability of pseudorange data, ionospheric constraints have been implemented in various forms, e.g., "narrowlaning" [Blewitt, 1993]. A cycle slip is a sudden jump in the carrier phase observable by an integer number of cycles. The fractional portion of the phase is not affected by this discontinuity. They are usually detected and fixed with the assistance of pseudorange data or ionospheric constraints during data preprocessing. Some cycle slips are connected or narrowed in preprocessing, and the remaining ones are estimated with other parameters. Cycle slips can also be edited manually.

Investigators found that a mix of baseline lengths enhances the ability to resolve integer cycle ambiguities for regional geodesy [Dong and Bock, 1989]. With the sufficiently dense global network and full GPS constellation, the restrictions may be relaxed. Sometimes, integer phase ambiguities can be just estimated as real numbers instead of fixing to integer numbers.

### 1.5.5 Multipath and Variations of Antenna Phase Center

Antennas for almost all GPS receivers are omni-directional, enabling signals from several satellites to be received simultaneously. Such antennas can be susceptible to interference ("multipath") from multiple arrivals of the same signal because of reflections from nearby objects. Multipath mainly corrupts the observables with systematic, time-dependent sinusoidal signals associated with variable receiver-satellite geometry over a pass, and can be averaged out with observations over a sufficiently long time period. The effect on code observation is two orders of magnitude larger than on carrier phase observations, because code wavelengths are much longer. Under the worst conditions the code signal multipath may cause the receiver to lose phase lock, causing many cycle slips. The ground-plane is designed to reduce the effects of signals received from negative elevation angles, but such signals are not rejected completely. The "choke-ring" antenna [Yunck *et al.*, 1989] usually has less multipath effects. Multipath can also be reduced by absorbent material around the antenna base and properly mounting the antenna.

The antenna phase center may vary in different directions and in different observation environments. Typical elevation variations are in the range of 1-5 cm. Specially designed GPS experiments in the field or in an anechoic chamber can provide descriptions of variations. Several correction tables are now available to be applied in GPS data analysis, but they are still not very consistent.

If antennas of the same type are used on a short baseline within one observation session the phase center offsets and variations are largely eliminated in the differencing

process. But differencing is inadequate over long baselines in global GPS networks or if different types of antennas are used within one network. For permanent sites most of multipath and phase center variations can be eliminated by daily averaging, as receiver-satellite geometry repeats every half sidereal day. But a change of elevation cutoff angle or antenna type may cause an offset of several millimeters in the vertical component [Neill *et al.*, 1994]. Multipath, which shows some elevation angle dependence and also corrupts vertical position estimates, can be reduced by choosing the locality of the GPS sites carefully (minimizing nearby obstructions).

Objects very close to the antenna, like the pillar on which the antenna is mounted, are electromagnetically coupled to the antenna system, which may modify the antenna phase pattern. This implies that the effective phase patterns may be different for two identical antennas mounted in different fields. Such effects would not be canceled by differencing. Research at some IGS tracking sites has indicated that the “standard” IGS antenna mount, where the antenna-choke ring backplane system is mounted on a short spike about 10 cm (about one half carrier wavelength) above a metal centering plate can lead to high multipath and vertical variation in the phase center which is elevation angle dependent [Neill *et al.*, 1994]. The problems may be related to signal resonance phenomena between the base of the choke ring and the metal centering plate. Since we always use a constant elevation angle cut-off ( $15^\circ$ ) in our analyses, systematic error associated with the phase center variation should be low. However, random and possibly systematic error associated with the multipath effect may still be present. Improved wrms

(weighted rms) has been seen at site CASA by adding a thin metal “skirt” around the base of the choke ring in late May, 1995 [Dixon *et al.*, 1997a].

### 1.5.6 Modeling the Site Motions

We are mainly concerned with the deformation of the crustal surface associated with particular geophysical phenomena. Some known site motions are modeled and corrected in GPS data analysis.

The solid earth surface can be displaced due to the tidal force of the Sun and Moon with an amplitude as large as 50 cm. Temporally varying part of solid earth tides, including Love number variation at the tide  $K_1$ , are usually modeled. Pole tides, which are displacements caused by polar motion, are also modeled with an amplitude of about 25 mm in the vertical and about 7 mm in the horizontal.

Local site displacement can be an effect of (visco-) elastic deformation of the Earth in response to time-varying surface loads, like ocean tides and temporal atmospheric variations. Ocean loading tides of east, north and vertical components at a site can be modeled as the sum of several tidal components.

$$\Delta P_i = \sum_j a_{ij} \cos(\omega_j t + \chi_j - \phi_{ij}) \quad (1.6)$$

where  $\omega$  and  $\chi$  are angular velocity and astronomical argument for each tidal term, and  $a_{ij}$  and  $\phi_{ij}$  are amplitude and phase delay for each components. The ocean loading coefficients for each site can be calculated from the global ocean tidal maps and (visco-)

elastic model of the Earth. Usually 11 major tidal components are considered. These are semi-diurnal tides  $M_2$ ,  $S_2$ ,  $N_2$ ,  $K_2$ , diurnal tides  $K_1$ ,  $O_1$ ,  $P_1$ ,  $Q_1$ , and long-period tides  $M_r$ ,  $M_m$  and  $S_{sa}$ . The coefficients suggested by the International Earth Rotation Service (IERS) were computed by H. G. Scherneck with 1066A elastic Earth model, Schwiderski ocean tidal maps for long-period waves, and TOPEX tidal maps for diurnal and semi-diurnal waves [McCarthy, 1996]. Ocean loading tides are important for sites in coastal regions.

Deformation of the Earth surface also can be caused by temporal variation in the geographic distribution of atmospheric mass load. Atmospheric pressure loading displacement is dominated by effects of loading variation within the radius of 1000-2000 km. The effect has not been widely modeled, because of the difficulty in obtaining a large volume of surface pressure data. It can cause displacement of about 10 mm with a maximum of 25 mm in the vertical and a few millimeters in the horizontal with seasonal attributes [vanDam *et al.*, 1994; Rabbel and Schuh, 1986]. The effects are larger at high latitudes due to the larger atmospheric pressure variations there.

### 1.5.7 Reference Frames for GPS Data Analysis

The equations of satellite motion and satellite to receiver propagation time are expressed in the earth-centered inertial reference frame. But receiver positions are expressed in the terrestrial (earth-fixed) reference. Transformation between the two reference frames is precisely defined by the International Astronomical Union (IAU) and its subsidiary, IERS. It is realized with the precession, nutation, UT1 (Universal Time)

and pole position values. In GPS data analysis, precession and nutation are modeled rather than estimated. GPS has no advantage to define the inertial reference frame compared to VLBI and SLR, which are used instead to maintain an inertial reference frame. The rate of UT1 change, pole position values and rates can be estimated directly from GPS data.

Other parameters (e.g., GM - geocentric gravitational constant), processes (e.g., relativity) and physical constants (e.g., c - speed of light in vacuum) required for GPS data analysis are summarized in IERS Technical Note 21 [*McCarthy, 1996*].

## **CHAPTER 2      GPS Data Analysis**

### **2.1    GPS Data Collection and Analysis at the UM/RSMAS Geodesy Lab**

#### **2.1.1 Overview of GPS applications and data collection at the UM/RSMAS Geodesy Lab**

Starting in mid-1994, we routinely analyzed GPS data from global permanent sites and campaign sites for various projects. The current number of permanent sites analyzed is about 105. GPS results have been used to monitor volcanic activities at Long Valley (California) [Mao *et al.*, 1994; Dixon *et al.*, 1997a], Popocatepl (Mexico), Arenal (Costa Rico) and Montserrat (British West Indies), and to investigate plate motions, plate rigidity and plate boundary deformation in North and South America [Dixon *et al.*, 1996; Dixon and Mao, 1997b; Leffler *et al.*, 1997; Norabuena *et al.*, 1998], which is fundamental to earthquake studies. Figure 2.1 shows the locations of GPS sites analyzed by the lab and some projects in which I have been involved: 1. Rigidity of the interior North America; 2. Monitoring volcanic activity at Long Valley, California; 3. Coastal subsidence, wet land loss and global sea level change; 4. Monitoring an active volcano near Mexico City; 5. Monitoring an active volcano in Costa Rico; 6. Tectonic motions in Caribbean; 7. Convergence across the central Andes; 8. Present-day motion across the east African rift. Most of these GPS data are available on the Internet through several institutions like IGS's global tracking network, NOAA's (National Oceanic and

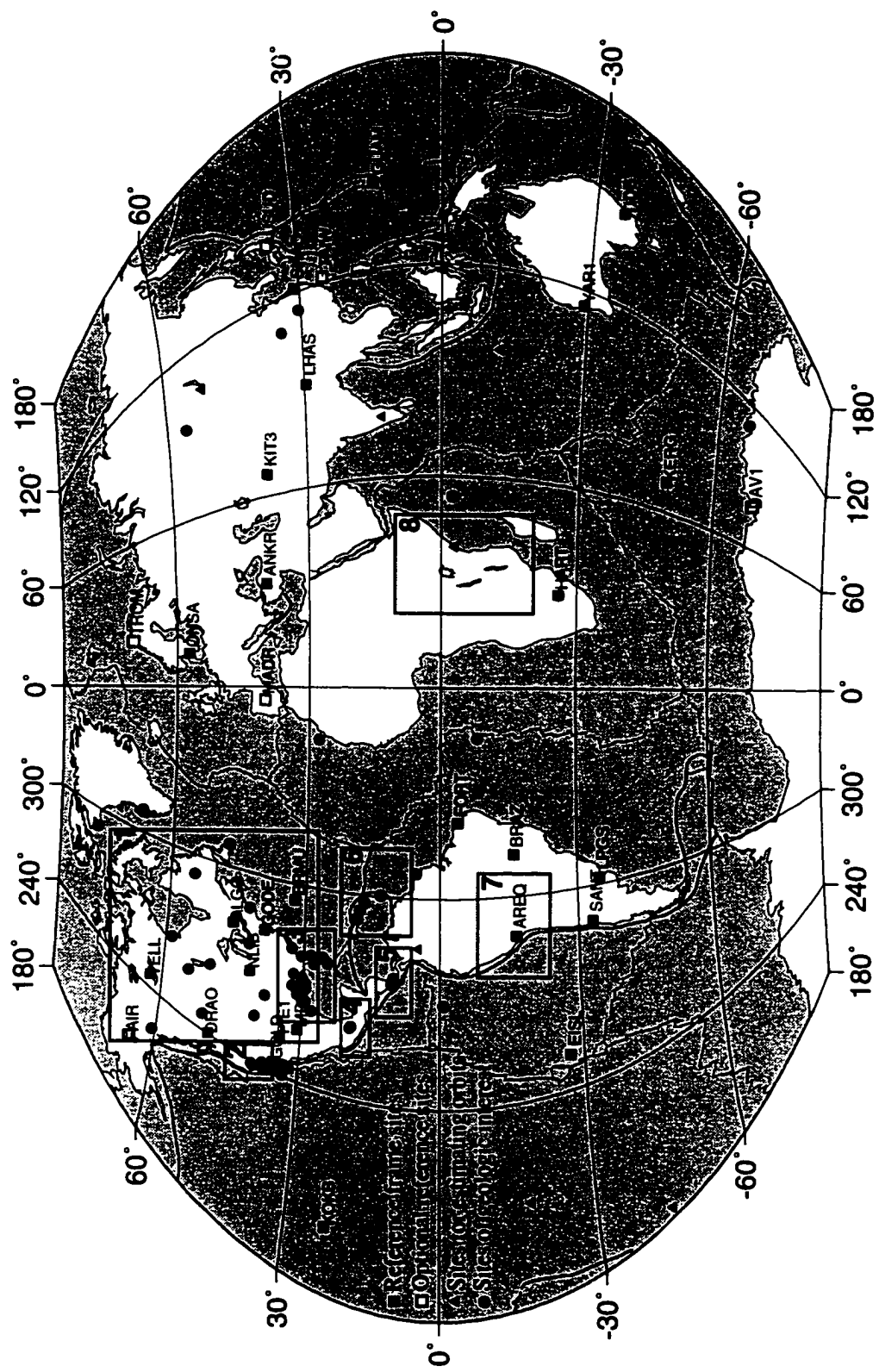


Figure 2.1 Two GPS time series are generated routinely at the Geodesy Lab. One uses precise orbits from JPL and includes reference sites (or optional sites if primary sites are not available) and sites of geologic interest. The other uses reference frame sites and additional sites to estimate the orbits along with site positions, for near real-time analysis (mainly for volcano monitoring). Numbered boxes show the locations of some projects in which I have been involved - see text for details.

Atmospheric Administration) CORS network, the BARD network around San Francisco Bay area and PGGA network in Southern California. We also installed additional GPS sites to complement existing network for our special interest.

Most of the sites are equipped with identical “TurboRogue” receivers and Dorn-Margolin antennas with a “choke ring” style backplane for multipath suppression, manufactured by Allan Osborne Associates. The receivers are dual frequency systems capable of tracking up to eight satellites simultaneously, and record both P-code and carrier phase data at 30 second intervals. Many other sites use Trimble or Ashtech receivers, some with a choke ring antenna essentially identical to the Dorn-Margolin antenna, others with standard Trimble or Ashtech antennas. Ashtech receivers and antennas are installed at most CORS sites. These CORS sites are not designed for geodetic applications, and are more susceptible to multipath and monument instability.

Two GPS time series are generated routinely at the UM/RSMAS Geodesy Lab. The first time series is based on a global network of ~25 tracking sites plus the stations in the area of interest (Figure 2.1). This time series is for time critical applications like volcano monitoring. Satellite orbits, clocks, and station positions are estimated simultaneously at UM within 36 hours of data reception. Selected results are made available to scientists and public officials via anonymous ftp (<ftp://corsica.rsmas.miami.edu/pub/>; see *Dixon et al. [1995]*), typically within 48 hours of data reception. In the second time series, site positions are estimated using the satellite ephemeris and clock information generated at JPL, available typically 1-2 weeks after data collection (Figure 2.1). The weighted root mean square (wrms) scatters for the two time series about the best fit line, a measure of precision, as well as the means of the two

time series, are very similar, differing at most by a few millimeters [Dixon *et al.*, 1997a]. The differences are within the formal errors of the results, negligible compared to the potentially large surface strain signals in an active volcanic region.

For more critical applications, near real-time analysis that employs the broadcast ephemeris, can be used for on-site data analysis with high time resolution (hours), and time delay of less than one hour.

### 2.1.2 Data Analysis with GIPSY Software

We use the GIPSY/OASIS II software developed at Jet Propulsion Laboratory (JPL) [Lichten, 1990; Webb and Zumberge, 1993] in our GPS data analysis. The primary goals of GIPSY are high accuracy and high flexibility. It uses the SRIF (Square-Root Information Filter), a Kalman filter with high numerical stability. The Kalman filter is relatively slow (about 2 times) compared to normal least squares, but it has high flexibility in parameter estimation. It can estimate satellite forces, clocks and atmospheric delay through the use of stochastic models. "Stochastic estimation" can range from the completely unpredictable behavior of white noise to models which allow time-correlated noise, polynomial behavior, or some combination of the above. The ionosphere-free combination of both undifferential carrier phase and P-code observations are used in GIPSY.

GIPSY software runs on several UNIX platforms. It contains about 400,000 lines of source code, most written in the FORTRAN programming language, with some C programming language codes and C-Shell scripts. It is R & D software, with continuous

improvements. Many investigators from different institutions have been involved in the development of GIPSY software. Because of these characteristics and the requirement of high flexibility, it lacks a consistent and user friendly interface and documentation. Extensive computer skills, GPS knowledge and special training are required to utilize it. Data processing can be controlled with command line arguments, environment variables and namelist files, which are text files containing special control information.

For routine data analysis, I have developed an automatic system, which continuously interrogates several independent GPS data sources on the Internet, selects an optimal set of GPS sites, initiates data analysis, performs quality checks, and outputs part of the results to an anonymous ftp site for public access. I have also developed several end-user programs for different analysis approaches. With the most complete end-user program, a single command can carry out all the analysis from a set of raw GPS data to the final precise site coordinates, which can ease the difficulty of GPS data analysis, especially for inexperienced users.

### 2.1.3 Analysis Strategy

We used the ionosphere-free combination of both undifferenced carrier phase and P-code pseudo-range observations (data weights of 1 cm and 3 m, respectively) decimated to five minutes, with an elevation cut-off of 15°. For the solutions involving estimated satellite orbits, we estimated receiver coordinates simultaneously with the initial position and velocity of each satellite and parameters related to the subsequent time evolution of the satellite orbits. These are the yaw rate and solar radiation pressure parameters, both employing a stochastic, Gauss-Markov model with 4 hour correlation

time (10% variation allowed over the specified time in the scale factors for the solar radiation pressure model in  $x$  and  $z$  coordinates;  $10^{-13}$  km/sec $^2$  variation allowed in the  $y$  bias). Also estimated simultaneously are the combination of wet and remaining dry zenith troposphere delay at each ground station (modeled as a random walk process with 1 cm $^2$ /hr variance; see *Dixon et al.* [1991b]; a standard dry delay was assumed based on station elevation and a standard atmosphere model), station and satellite clock offsets from a reference clock, usually Goldstone (estimated at each epoch assuming a white noise model), carrier phase cycle ambiguities (estimated as real numbers with 1 millisecond *a priori* sigma), and earth orientation parameters (EOP) except UT1-UTC, which was fixed to values given in IERS Bulletin B (*a priori* sigma 100 sec/day for UT1-UTC rate ; 5 meters for X and Y pole position; 1 meter/day for X and Y pole rate). Solid earth tide, pole tide, Love number variation at the K<sub>1</sub> frequency and ocean tidal loading are modeled. Each site position is estimated from 24 hours of GPS data. The non-fiducial approach was used, in which the coordinates of eight well defined global sites were constrained with an *a priori* uncertainty of  $\pm 10$  m. An *a priori* constraint of 1 km was applied for all other sites. These loose constraints are sufficient to avoid singularities in the GPS solutions but are not sufficient to define the reference frame.

For the time series using precise satellite orbits and clocks, the processing strategy is similar, except that 5 minute data decimation is used (to match the satellite orbit and clock time series provided by JPL) and neither satellite related parameters nor EOP are estimated. Only site related parameters (site positions, zenith tropospheric delay,

receiver clocks and phase ambiguities, sometimes including satellite clocks) are estimated.

For the time series employing the broadcast ephemeris, one site is fixed, and the positions of the others are estimated along with carrier phase ambiguities and station and satellite clocks. The zenith wet troposphere delays were modeled rather than estimated because of their high correlation on short baselines and limited data strength.

#### 2.1.4 Precise Orbits and Point Positioning

Tests show that additional GPS sites in a dense region do not significantly improve the orbit estimation, and may even lead to systematic error by overweighting [Zumberge *et al.*, 1997]. With the current global distribution of GPS sites, simultaneous analysis of about 40 well distributed sites is adequate to define the satellite orbits precisely. Thus GPS data analysis can be carried out in two steps. First, satellite related parameters (orbits and clocks) can be estimated with a subset of globally distributed GPS sites. Second, positions of additional regional GPS sites are estimated by fixing the satellite orbit and clock information generated in the first step. Sometimes, satellite clock information is not available if double differencing techniques are used in the first step.

In order to reduce the GPS analysis burden for individual groups, precise satellite orbits and clock corrections are available from several analysis centers, under the auspices of IGS (International GPS Service), within a week or so after data collection. IGS also publishes a combined orbit data from solutions submitted by individual analysis centers. Slightly less accurate data are also available more rapidly. Even predicted orbits are available. The use of these orbit products is now widespread as routine analysis of

GPS data, as it relieves the individual from computationally intensive orbit calculations, and improves the speed and in some cases the precision of GPS data analysis. The improved precision reflects the fact that: 1) IGS orbits are based on a large global network of stations, which an individual user might not be able to handle on a small computer, and 2) orbits have undergone several consistency checks before being submitted to the IGS. The accuracy of the orbits is now about 7-15 cm 3D RMS [Zumberge *et al.*, 1997]. We use JPL orbit and clock data because of their no-fiducial property. Our tests show that JPL's no-fiducial orbit and clock data yielded better repeatability of site coordinates than the IGS combined orbits.

The point positioning approach takes advantage of the independence among GPS sites when precise GPS orbit and clock information is available. Only site related parameters are estimated. It processes GPS data site by site, and assembles the coordinate solutions together at the end. The approach is very efficient for obtaining precise solutions from a large data set, which is critical for the ever expanding global GPS network. Based on our tests, it can reduce requirements of computer memory and disk storage by 80%, and CPU by 70%, compared with the regular analysis. The computational burden increases in  $O(n)$  (linearly) instead of  $O(n^3)$  with the number of sites. It is also easy to add new sites to an existing solution.

When precise orbit and clock data are used, their uncertainties are currently not accounted for. One problem of precise point positioning is that the covariance matrix may not properly represent the accuracy of estimates, as it shows no correlation between sites and the covariance matrix for each site is also independent of the site location

[Zumberge, et al., 1997]. The formal error of short baselines (less than a few kilometers) derived from such solutions is larger than derived from rigorous solutions. The formal errors of a site in a sparse area, where satellite parameters are probably not well determined, are not different from those in a dense area. The latter problem will become negligible with the improvement of the global GPS network. The second limitation is that precise satellite clock estimates are only available at data epochs with an interval of several minutes. It is almost meaningless to interpolate the clock time series, as the GPS clocks vary quickly because of S/A policy. The data to be analyzed with precise point positioning have to be decimated to coincide with epochs of available GPS clock solutions.

## 2.2 Defining the GPS Results in the International Terrestrial Reference Frame

### 2.2.1 Introduction

Without an accurate and consistent definition of the terrestrial reference system, it is impossible to detect land motion of a few mm per year over large scales. Ideally, the station positions should be expressed in an earth-fixed reference system. But there are several situations complicating the realization of such a reference system. The earth rotation axis is moving relative to the solid earth, which can be described by pole motion and UT1 change. The earth rotation axis is wobbling in the celestial reference frame, which is described by precession and nutation. Because of plate motion and tectonic deformation, different parts of the Earth's surface are moving with each other. Even the

mass center of the Earth can move by several centimeters around the geometric center [Vigue *et al.*, 1992]. IERS suggested that a conventional terrestrial reference system can be realized through a reference frame which consists of a set of stations. The coordinate accuracy of these stations will be improved with accumulation of geodetic data, so that the terrestrial reference frame is accomplished in an iterative approach.

### 2.2.2 International Terrestrial Reference Frame

The International Earth Rotation Service (IERS) publishes the International Terrestrial Reference Frame (ITRF) almost every year, which contains the epoch positions ( $X_o$ ) and velocities ( $V_o$ ) of selected geodetic monuments around the world. Here, a linear model is used for time evolution of station positions

$$X(t) = X_0 + V_0(t - t_0) \quad (2.1)$$

The newest ITRF is ITRF-96, which is obtained by combining VLBI, SLR, GPS and DORIS solutions analyzed by several groups around the world [Boucher, 1998]. All the individual solutions including velocities were orthogonally projected to the same datum. The covariance matrix of each solution was rescaled in combination depending on the quality of the solution. Available local ties of collocated sites were incorporated in the combination to align different techniques. Velocities for all points at one site were constrained to be identical. The datum of ITRF-96 is aligned with its predecessor ITRF-94 and defined in the following way: the origin is a weighted average of a selection of

SLR and GPS solutions; the scale is a weighted average of a selection of VLBI, SLR and GPS solutions, modified in order to take into account the fact that the solutions use TAI and not TCG as a time scale; the orientation is consistent with the ITRF-94 at epoch 1993.0; and the time evolution is consistent with the no-net-rotation plate motion model NNR-NUVEL1A [Boucher, 1998]. ITRF-96 is believed to be accurate to the centimeter level, and is the most accurate reference frame available today.

### 2.2.3 Non-Fiducial GPS Data Analysis

Traditionally, the reference frame of a solution is defined during GPS data analysis by fixing the coordinates of a set of fiducial sites. The disadvantage of this fiducial approach is that position errors of the fiducial sites can distort the GPS solutions. Such position errors can come from inconsistency between the reference frame and individual solution. The improved satellite coverage and density of global permanent GPS sites enabled us to analyze the GPS data with the so-called “no-fiducial approach”, in which no site positions are held fixed [Heflin *et al.*, 1992; Blewitt *et al.*, 1992]. This approach treats the global GPS network as a rigid closed polyhedron constructed with GPS sites as apexes. GPS data alone can precisely constrain the polyhedron or relative positions of GPS sites, which should not be affected by fiducial errors. To avoid the consequences of distortion caused by fiducial error, a priori uncertainties are set to arbitrarily large values (e.g., 1 km for most sites, 10 m for some well measured sites). The resulting non-fiducial solution is in a poorly defined reference frame and can be transformed to a particular reference frame with a Helmert transformation. It is also

convenient to define the results in any new reference frame when ITRF is updated in future by simply re-transforming the data, which is much less cumbersome than full re-analysis.

The “no-fiducial” approach outlined above is readily implemented when satellite orbits are estimated. However, if precise orbits are used in the analysis to reduce processing time, the individual user may lose some flexibility in the choice of reference frame, as the result may be in a reference frame defined by the orbits and the accompanied Earth Orientation Parameters (EOP). Care must be taken in the choice of reference frame applied to the orbits. Orbit data derived with the fiducial approach or in a fixed reference frame may corrupt the resulting site position/velocity estimates if the results are compared to other data derived in a different reference frame. For example, when using some standard orbit products we observed offsets of up to several centimeters in the “absolute” coordinates of sites in the southern hemisphere for time series spanning January 1, 1995, when IGS orbit products were updated from ITRF-92 to ITRF-93 (northern hemisphere offsets were smaller, probably reflecting the fact that the southern hemisphere was more poorly defined in the ITRF-92). While the chances of misinterpreting a reference frame update in terms of a geologic signal are small (the updates are well advertised, and relative, as opposed to absolute, positions on baselines less than about a hundred kilometers in length are much less affected), a more serious problem is the corruption of velocity estimates for periods spanning the break, especially if absolute coordinates are used. Since early 1995, JPL has supplied reference frame-free orbit data obtained with the no fiducial approach, and these are used in our analysis.

### 2.2.4 Helmert Transformation of Cartesian Coordinate Systems

The transformation from one reference system  $(x_1, y_1, z_1)^T$  to another reference system  $(x_2, y_2, z_2)^T$  can be performed with the following equation of Helmert (similarity or orthogonal) transformation which includes rotations, translations and a scale factor

$$\begin{pmatrix} x_2 \\ y_2 \\ z_2 \end{pmatrix} = \begin{pmatrix} x_1 \\ y_1 \\ z_1 \end{pmatrix} + \begin{pmatrix} T_x \\ T_y \\ T_z \end{pmatrix} + \begin{pmatrix} S & -\theta_z & \theta_y \\ \theta_z & S & -\theta_x \\ -\theta_y & \theta_x & S \end{pmatrix} \begin{pmatrix} x_1 \\ y_1 \\ z_1 \end{pmatrix} \quad (2.2)$$

where,  $(T_x, T_y, T_z)^T$  is the translations of the two reference systems,  $S$  is the scale factor, and  $\theta_x, \theta_y, \theta_z$  are the rotations. For the above linearized equation to be valid,  $\theta_x, \theta_y, \theta_z$  and  $S$  must be small ( $<<1$ ), which is ensured in GPS data analysis by applying weak constraints of 10 m for some well determined sites to *a priori* station coordinates. Velocities also can be transformed by introducing seven additional transformation parameters and combining a transform equation which is the differentiation of equation (2.2).

The transformation parameters can be estimated based on a minimization of coordinate differences of some common sites available in both reference frames with the following observation equation:

$$\Delta = A\theta + v \text{ with covariance matrix } Q_{\Delta\Delta} = Q_{11} + Q_{22} \quad (2.3)$$

where

$$\Delta = \begin{pmatrix} x_2^i - x_1^i \\ y_2^i - y_1^i \\ z_2^i - z_1^i \\ \vdots \end{pmatrix} \quad (2.4)$$

is the vector of coordinate differences for sites appeared in both reference frames, and

$$A = \begin{pmatrix} 1 & 0 & 0 & x_1^i & 0 & z_1^i & -y_1^i \\ 0 & 1 & 0 & y_1^i & -z_1^i & 0 & x_1^i \\ 0 & 0 & 1 & z_1^i & y_1^i & -x_1^i & 0 \\ \vdots & \vdots & \vdots & \vdots & \vdots & \vdots & \vdots \end{pmatrix} \quad (2.5)$$

The superscripts indicate the site number,  $\theta = (T_x, T_y, T_z, S, \theta_x, \theta_y, \theta_z)^T$  represents the transformation parameters, and  $v$  is the measurement error.

Before the no-fiducial solution is transformed to ITRF, an orthogonal projection (operator) is also applied to the covariance matrix of the no-fiducial solution to remove components of formal error that are correlated with reference frame orientation, origin, and scale (applying minimal internal constraints). The constrained covariance matrix  $Q_{xx}$  is computed from the no-fiducial covariance matrix  $Q_{nn}$  using [Heflin et al., 1992; Blewitt et al., 1992]

$$Q_{xx}^{-1} = (Q_{nn}^{-1} + B^T Q_{nn}^{-1} B) \quad (2.6)$$

Where  $B = (A^T A)^{-1} A^T$ , and matrix  $A$  is defined in equation (2.5).

Individual solutions can be combined to yield a global set of positions  $X_0$  and velocities  $V_0$  at epoch  $t_0$  with the following linear model:

$$\begin{pmatrix} X_i^j \\ V_i^j \end{pmatrix} = \begin{pmatrix} I & (t_i - t_0)I \\ 0 & I \end{pmatrix} \begin{pmatrix} X_0^j \\ V_0^j \end{pmatrix} + v \quad (2.7)$$

where  $I$  is an unit matrix and  $v$  is the measurement error. Such an observation equation can be established for each measured site  $j$  at every epoch  $i$   $\begin{pmatrix} X_i \\ V_i \end{pmatrix}$ .

Sometimes, the covariance matrix of a solution has been constrained (too small) because of some assumptions made during data analysis, even though the solution has not been fixed to any precise reference frame. In this case, the covariance matrix may be loosened (enlarged) with following equation:

$$Q_{nn} = Q_{xx} + A Q_{\theta\theta} A^T \quad (2.8)$$

where  $Q_{\theta\theta}$  is the covariance matrix of the transformation parameters. For most space geodetic data we can set  $Q_{\theta\theta}$  as a diagonal matrix with its diagonal elements equal to (10m, 10m, 10m,  $10^{-6}$ ,  $10^{-6}$  rad,  $10^{-6}$  rad,  $10^{-6}$  rad).

### 2.2.5 Estimation of Site Velocities in ITRF from No-Fiducial Solutions

There are several ways to estimate site velocities in ITRF from no-fiducial daily solutions. In order to characterize the noise in individual coordinate components and investigate possible problems relating to transformation, we used the first method in our data analysis. Nevertheless, other transformation approaches are described here.

The seven transformation parameters for each daily GPS solution can be estimated with equation (2.3) based on data from a subset of tracking sites whose positions are defined in the ITRF. Then the daily GPS solutions can be transformed into ITRF. The velocity can be estimated by fitting a straight line to the entire time series for an individual site, or combined to fit a linear model as in equation (2.1) for all sites. Unfortunately, the realization of the reference frame may be slightly different for each day because of data outages at some reference sites.

Another way is first to estimate the velocities and epoch positions of all sites by combining the unconstrained daily solutions with equation (2.1). The combined solution, like the daily solutions, is also loosely constrained. Transformations of both position and velocity can be applied on the combined solution by using the published ITRF positions and velocities for selected reference sites. First, the daily solutions are combined into a linear model (three dimensional position at epoch plus velocity for each station) without fiducial constraints using weighted least squares. Second, this combined linear model is transformed to ITRF or other reference frame using a Helmert transformation following the procedure described above. A projection operator as equation (2.6) is also applied to the covariance matrix of the combined solution to remove those components of the formal error that are correlated with reference frame origin, orientation, and scale.

Detecting outliers is a little complicated with this approach. Because GPS results are highly correlated over periods of several days [King *et al.*, 1995], and tectonic motion in several days is negligible, solutions of several days can be combined first with proper covariance rescale and outlier check.

There may be some inconsistency between the ITRF and global GPS reference frame (e.g., errors in tie surveying and antenna heights). In addition, different sets of global tracking sites may be used on different days based on the data availability of each day. This kind of reference frame inconsistency may introduce some noise into the site position time series, when daily no-fiducial solutions are transformed directly into ITRF. We can use the combined linear model obtained above as a global GPS terrestrial reference frame, which is easily updated with the accumulation of GPS observations and improvement of ITRF. Each of the daily no-fiducial solutions are projected and transformed into the GPS terrestrial reference frame with a similar procedure as shown above. Finally, the original daily solutions with minimal constraints are now transformed to produce the best estimate of daily position in the ITRF, by minimizing their coordinate differences with the GPS terrestrial reference frame produced above.

The quality of the transformation will depend on the accuracy of the coordinates and velocities of the reference stations which are used to derive the transformation and on the geographic distribution of those stations. The reference sites used to transform the no-fiducial solutions should be globally distributed as evenly as possible and have similar weights, although the exact distribution and number of sites are not critical. This can avoid the domination of any particular area (e.g., North America) in the definition of the reference frame. The motions of these stations should also be constant in time (no

unstable sites, no earthquakes). We have developed an algorithm that automatically selects about 18 optimal sites from the ensemble of all ITRF sites available on a given day based on geographic distribution, coordinate accuracy and data availability.

When we estimate site velocities with linear regression, data outliers (defined as lying more than three standard deviations from the best fit line) are flagged but not removed, and the user has the option of incorporating them in the velocity fit. This philosophy reflects the difficulty of distinguishing signal from noise where the signal (e.g., volcanic deformation) may be highly variable in time.

### **2.3 Postprocessing**

The manner in which the three orthogonal site velocities are used depends on the problem to be solved. In Section 4.2, I will discuss one method for using the horizontal components to investigate plate motion and plate rigidity, which involves a least squares inversion techniques to estimate Euler vectors from the GPS velocity data.

## CHAPTER 3      Noise in GPS Time Series

### 3.1    Introduction

Geophysical studies requiring geodetic measurements of surface velocity or strain require not only accurate estimates of these parameters, but also accurate error estimates. Geodetic measurements of displacement differ in two important ways from other types of geophysical data, and these differences complicate error estimation.

First, we generally require a long time series of measurements, often several years or more, in order to obtain accurate site velocity estimates. This means that a variety of errors with different time scales can corrupt our data. Even an individual error source may change with time, for example the instrument may improve. It is convenient to characterize errors as white (no time dependence) and colored (time-correlated). While the effect of white noise can be greatly reduced through frequent measurements and averaging, this is not so useful for time-correlated noise because of the positive correlation among neighboring data points.

Second, while we generally seek to infer the motion of large crustal units, what we actually measure is the motion of one or more antenna phase centers, set up in a way that hopefully bears some consistent relation to a mark or monument in or near the ground surface. Spurious motion of the mark (monument noise) unrelated to motion of the larger crustal units of interest has been identified as an important noise source for many geodetic measurements [*Johnson and Agnew, 1995*]. Analysis of long (decade or more) time series

of high precision two color EDM (Electronic Distance Measuring) data from sites in California suggests that monument noise can be modeled as a random walk, a type of time-correlated noise [*Langbein and Johnson, 1997*].

For geodetic data acquired with the Global Positioning System (GPS), a variety of time-correlated processes in addition to monument noise corrupt velocity estimates, and in fact likely dominate the error budget at the present time. In other words, GPS velocity estimates are not yet accurate enough to observe monument noise except in extreme cases. Possible sources of time-correlated noise include mis-modeled satellite orbits, other reference frame effects (e.g., earth orientation), mis-modeled atmospheric effects, and mis-modeled or unmodeled antenna phase center effects, which may vary with satellite elevation and environmental factors.

Studies of time-correlated noise in GPS time series have been hampered by the relatively short time that high quality time series have been available. Rigorous analysis of time-correlated noise in GPS may well require decade or longer time series, but high precision results from continuously operating stations are available only since about 1992 or 1993. The present study reports the noise characteristics of 23 globally distributed GPS sites that have operated more or less continuously for approximately 3 years.

### *Previous Work*

*Zhang et al. [1997]* performed a thorough analysis of 19 months of essentially continuous daily measurements from 10 sites in southern California. They were able to reduce regionally correlated noise (probably dominated by orbit errors) by use of a

filtering algorithm that subtracted common mode, non-tectonic signals from the GPS time series [Wdowinski *et al.*, 1997]. This method is applicable wherever data from a relatively dense network are available, but may not be possible for many global sites, which are relatively isolated. Noise in the residual time series studied by Zhang *et al.* [1997] was characterized as flicker noise or fractal white noise.

This study differs in several ways from the study of Zhang *et al.* [1997]. First, longer time series (3.0 years) are now available. This is important in assessing long period time-correlated noise. Second, we study a global distribution of sites (Figure 3.1), which allows us to assess regional differences in noise. This is important for GPS, where orbit and reference frame errors are likely to be important and may exhibit regional differences.

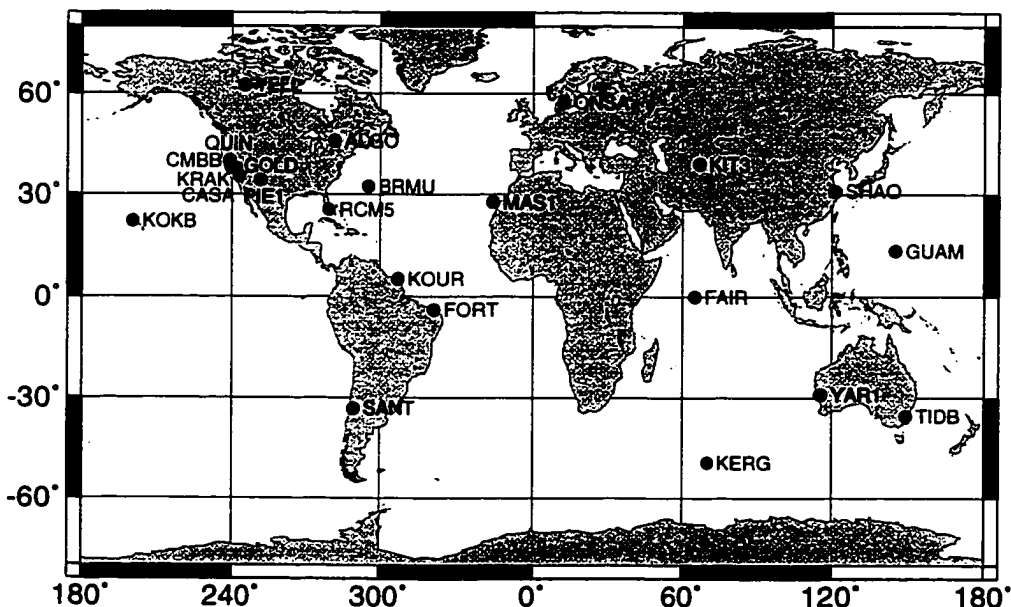


Figure 3.1 Distribution of GPS stations used in this study.

Third, we have studied "raw" GPS time series, as opposed to the data with orbit and reference frame errors reduced or eliminated through common mode techniques. Thus our results should be applicable to GPS coordinate time series from any site, no matter how isolated. Relative baseline data can be expected to be less noisy than results presented here, depending on baseline length.

### 3.2 Data Analysis

Beginning in 1994, GPS data from a number of continuously operating stations (currently 85) have been analyzed in the Geodesy Laboratory of the University of Miami to study various geophysical phenomena. To save computer time, we use satellite orbit and clock files provided by the Jet Propulsion Laboratory (JPL) [Zumberge *et al.*, 1997]. The resulting daily station coordinates are transformed into global reference frame ITRF-94 [Boucher *et al.*, 1996]. Analysis procedures are described in Dixon *et al.* [1997a].

We used two methods, spectral analysis and Maximum Likelihood Estimation (MLE), to assess time-correlated noise in these time series. We used spectral analysis to estimate the spectral indices of noise, while MLE was used to characterize stochastic processes with integer spectral indices.

#### 3.2.1 Spectral Analysis

The power spectra,  $P$ , of many geophysical phenomena are well approximated by a power-law dependence on frequency  $f$  of the form [Agnew, 1992]:

$$P(f) = P_0 f^{-\alpha} \quad (3.1)$$

where  $\alpha$  is the spectral index and  $P_0$  is a normalizing constant. Larger  $\alpha$  implies a more correlated process, and more power at lower frequencies. White noise has a spectral index of 0, flicker noise has a spectral index of 1, and a random walk process has a spectral index of 2.

Spectral indices are not limited to integer values. Geophysical phenomena and noise may have fractional spectral indices in the range  $1 < \alpha < 3$  and are termed “fractal random walk”, while indices in the range  $-1 < \alpha < 1$  are “fractal white noise” [Agnew, 1992]. Noise processes with  $-1 < \alpha < 1$  are stationary, while processes with spectral index larger than 1 are non-stationary. A stationary random process is one whose statistical properties (e.g., mean and covariance) are invariant in time.

Following *Langbein and Johnson* [1997], the spectrum of a set of measurements can be modeled as the sum of white noise and colored noise:

$$P(f) = P_0 (f^{-\alpha} + f_0^{-\alpha}) \quad (3.2)$$

where  $f_0$  is the cross-over frequency of the power spectrum defined as the point at which two noises have the equivalent power levels. Although  $f_0^{-\alpha}$  can be treated as one unknown, we express it in this way to make  $f_0$  equal to the cross-over frequency.  $\alpha$ ,  $P_0$  and  $f_0$  can be determined by fitting a curve to the power spectrum. A non-linear least-squares method

has been used to estimate these parameters, in which the minimization must proceed iteratively. In order to speed the convergence, we apply the natural logarithm to both sides

$$\ln P(f) = \ln P_0 + \ln(f^{-\alpha} + f_0^{-\alpha}) \quad (3.3)$$

The differential form of this equation can be written:

$$d\{\ln[P(f)]\} = d\ln(P_0) - \frac{\alpha f_0^{-\alpha-1}}{f^{-\alpha} + f_0^{-\alpha}} df_0 + \frac{f^{-\alpha} \ln f + f_0^{-\alpha} \ln f_0}{f^{-\alpha} + f_0^{-\alpha}} d\alpha \quad (3.4)$$

With the relation between parameters and measurements in (4), we can form observation equations for individual frequencies,  $AX = V$ , where  $X = [\ln(P_0), f_0, \alpha]^T$  is the parameter vector, and  $V = O-C$ . A normal equation can be created based on least-squares in the form

$$NX = L \quad (3.5)$$

where normal matrix  $N = A^T A = [n_{ij}]$  and vector  $L = A^T L = [l_i]$ . The Levenber-Marquardt method [Press et al., 1992] is used to solve the non-linear problem. The normal matrix here gives only the slope at a particular point, but not how far that slope extends. We can replace the normal matrix  $N$  in (5) with a new matrix  $N' = [n'_{ij}]$  defined by the following rules:

$$n'_{ij} = \begin{cases} n_{ij}(1+\lambda) & i=j \\ n_{ij} & i \neq j \end{cases} \quad (3.6)$$

When  $\lambda$  is very large, the matrix  $N'$  is forced to be nearly diagonal, and the step by which the solution is approached is reduced because the diagonal elements of the normal matrix are enlarged. On the other hand, as  $\lambda$  approaches zero,  $N'$  will be close to the real normal matrix  $N$ .

Given an initial guess for the set of fitted parameters  $X$ , we use the following iterative steps modified from the Levenber-Marquardt method:

- (1) Pick a modest value for  $\lambda$ , say  $\lambda = 0.001$
- (2) Compute normal matrix  $N$ ,  $L$  and  $\chi^2(X)$
- (3) Modify the normal matrix as in equation (3.6) and solve the modified normal equation (3.5) for  $\delta X$  and evaluate  $\chi^2(X + \delta X)$
- (4) If  $\chi^2(X + \delta X) \geq \chi^2(X)$ , increase  $\lambda$  by a factor of 10 and go back to step (3)
- (5) If  $\chi^2(X + \delta X) < \chi^2(X)$ , update the trial solution with  $X + \delta X$ , decrease  $\lambda$  by a factor of 10 and go back to step (2)

The iteration can be stopped when  $\chi^2(X + \delta X)$  decreases by a negligible amount for  $\lambda \leq 0.01$ . There is some chance that the parameter will lie near a local minimum instead of converging to the best estimate. For our case,  $\alpha$  and  $P_0$  vary by less than 10, while  $f_0$  is much more variable and may cause convergence problems.

When  $\alpha = 2$ , equation (3.2) approaches  $P_0/f^2$  at low frequencies, which corresponds to a random walk, and approaches a constant  $P_0/f_0^2$  at high frequencies, which corresponds to white noise. The white noise and random-walk noise components can be calculated from estimated values of  $P_0$  and  $f_0$ . Noise components estimated in this way are less precise than those derived with the Maximum Likelihood Estimation techniques described later.

We have two ways to estimate the periodogram of a time series, depending on whether data are evenly spaced or not. For a series of  $N$  discrete observations  $x_j$ , ( $j = 1, N$ ) at equal spacing, the power spectrum by means of a periodogram is defined from the discrete Fourier transform as [Scarge, 1982]

$$P(f_n) = \frac{1}{N} \left[ \left( \sum_{j=1}^N x_j \cos 2\pi j f_n \right)^2 + \left( \sum_{j=1}^N x_j \sin 2\pi j f_n \right)^2 \right] \quad (3.7)$$

where  $f_n = n/T$ , where  $T$  is the fundamental period and  $n = 1, \dots, N/2$ . If  $x_j$  is pure white noise,  $P(f_n)$  is an exponentially distributed random variable with an expectation equal to the variance of the white noise. The amplitudes of the spectrum at these natural frequencies  $f_n$  are strictly independent.

From our tests, windowing can artificially enhance the power at low frequencies, which is undesirable. Windowing is not applied in our analysis, as we are interested in the overall profile of the power spectrum instead of signals at particular frequencies, where

resolution is a major concern. Sidelobes can be reduced when most known strong signals (e.g., annual term) are removed before spectral estimation.

For many situations evenly spaced data cannot be obtained. There are some ways to modify unevenly spaced time series to simulate evenly spaced ones. Interpolation is one approach, but most interpolation techniques perform poorly for large gaps, a problem at some of the GPS sites. *Lomb* [1976] estimated the spectrum by fitting sine waves directly to the data. Given a set of  $N$  observations  $x_j$  with zero mean at  $t_j$ , we can set up the following model at a given frequency  $f$ :

$$x_j + \varepsilon_j = a \cos 2\pi(t_j - \tau)f + b \sin 2\pi(t_j - \tau)f \quad (3.8)$$

where the errors  $\varepsilon_j$  are independent, have zero mean and common variance;  $a$ ,  $b$  are unknowns and  $\tau$  is introduced for simplification, defined by

$$\tan(4\pi f\tau) = \sum_{j=1}^N \sin 4\pi t_j f / \sum_{j=1}^N \cos 4\pi t_j f \quad (3.9)$$

Then the periodogram can be derived as follows:

$$P(f) = \frac{1}{2} \left\{ \frac{\left[ \sum_{j=1}^N x_j \cos 2\pi(t_j - \tau)f \right]^2}{\sum_{j=1}^N \cos^2 2\pi(t_j - \tau)f} + \frac{\left[ \sum_{j=1}^N x_j \sin 2\pi(t_j - \tau)f \right]^2}{\sum_{j=1}^N \sin^2 2\pi(t_j - \tau)f} \right\} \quad (3.10)$$

*Scarge* [1982] proved that the resulting periodogram has exactly the same exponential probability distribution as for evenly spaced data. Windowing techniques can also be applied. While this expression can be evaluated at any frequency, it is typically evaluated only at a natural set of evenly spaced frequencies similar to the Fourier spectrum, defined by

$$f_n = n / T \quad (n = 1, 2, \dots) \quad (3.11)$$

where  $T$  is the fundamental period.

However, the independence of the periodogram at these natural frequencies is lost for unevenly spaced data. We can prove by numerical test or derivation that the Fourier spectrum and Least-Squares estimation are equivalent, when both methods are applied on the same evenly spaced data. When we randomly take off 30% points from an evenly spaced time series, we find there is no bias in the resulting spectral profile, compared with the spectrum estimated from the original time series (Figure 3.2). We conclude that we are able to obtain robust spectral estimates of a GPS time series even when there are gaps in the data.

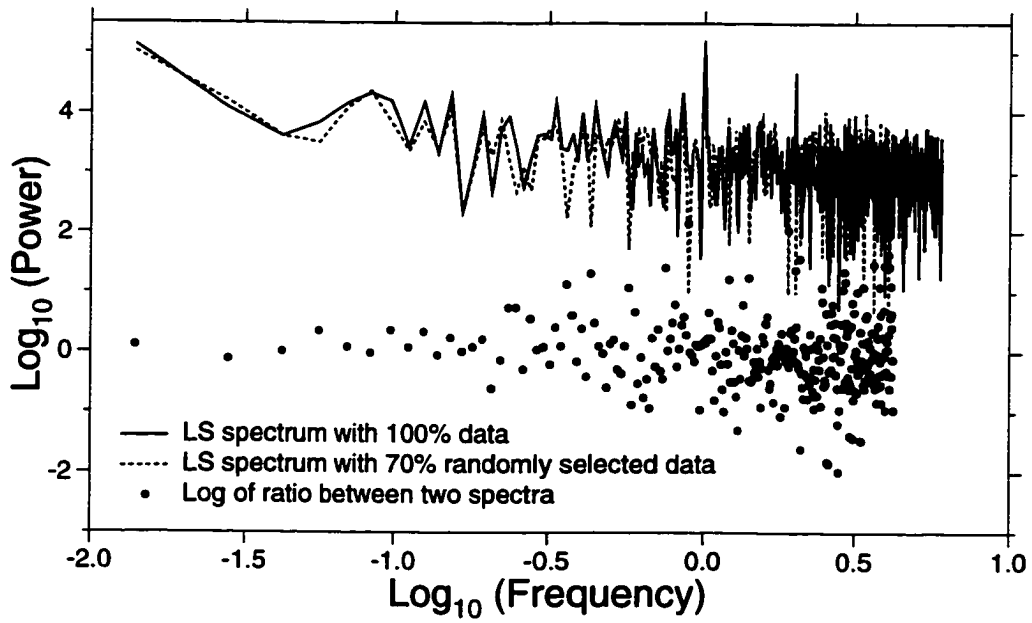


Figure 3.2 Power spectrum computed from complete time series (solid line) compared with spectrum computed with 30% of data are randomly removed. Data are 73 years of monthly mean tide gauge data from Boston. An annual and semi-annual term stand out above the noise. Frequency is in cycles/year.

For relatively short time series, the spectral index can be underestimated. We have investigated this problem in two steps. First, the non-linear estimation method was tested on theoretical power-law spectra with different lowest frequency. Both spectral indices of 2 and 1 were tested. Non-linear least squares can estimate the spectral index reliably when the length of the time series is 0.8 times longer than the cross-over period ( $1/f_0$ ) for both cases.

**Table 3.1 Test Results of Spectral Analysis on Synthetic Time Series**

Length of time series	1 yr	2 yrs	3 yrs	5 yrs	8 yrs	15 yrs
<i>Test case one: white + flicker noise</i>						
Mean $\pm$ Std dev	1.22 $\pm$ 0.50	1.12 $\pm$ 0.40	1.15 $\pm$ 0.32	1.08 $\pm$ 0.25	1.07 $\pm$ 0.15	1.10 $\pm$ 0.11
Converged solutions	29	40	40	40	40	40
<i>Test case one with annual term removed</i>						
Mean $\pm$ Std dev	0.77 $\pm$ 0.27	0.67 $\pm$ 0.25	0.82 $\pm$ 0.31	0.83 $\pm$ 0.17	0.92 $\pm$ 0.17	1.02 $\pm$ 0.00
Converged solutions	15	31	36	40	40	40
<i>Test case two: white noise + random walk noise</i>						
Mean $\pm$ Std dev	0.91 $\pm$ 0.63	1.42 $\pm$ 1.23	1.81 $\pm$ 1.41	1.48 $\pm$ 0.63	1.68 $\pm$ 0.62	1.99 $\pm$ 0.42
Converged solutions	9	16	30	34	40	40
<i>Test case two with annual term removed</i>						
Mean $\pm$ Std dev	-	0.13 $\pm$ 0.11	1.55 $\pm$ 2.09	1.52 $\pm$ 1.22	2.20 $\pm$ 1.02	2.30 $\pm$ 0.52
Converged solutions	0	3	6	13	29	39

A total of 40 simulations were tested for each solution. In test case one, the time series were simulated with 4.0 mm of white noise and 5.0 mm of flicker noise. 30% of the points are randomly taken away. The cross-over period of such a time series is about 19 days. In test case two, we simulated GPS time series with 4.5 mm of white noise and 1.5mm/ $\sqrt{\text{yr}}$  of random walk noise, whose cross-over period is about one year.

We further tested both the spectral analysis method and non-linear least squares method on synthetic time series, mixing white noise with either flicker noise or random walk noise, with similar amplitudes to current GPS time series (Table 3.1). In test case one, the time series were simulated with 4.0 mm of white noise and 5.0 mm of flicker noise. 30% of the points are randomly taken away. The cross-over period of these time series is about 20 days. We found that the spectral indices can be estimated reliably for time series longer than 2 years. Although the mean estimation is not biased for one year, many solutions failed to converge. We also found that it is more difficult to estimate the spectral index when we removed the annual term. In test case two, we simulated GPS time

series with 4.5 mm of white noise and  $1.5 \text{ mm}/\sqrt{\text{yr}}$  of random walk noise, whose cross-over period is about one year. The length of data required to accurately characterize the random walk component is usually taken to be five times the cross-over period ( $5 / f_0$ ), in this case 5 years. However, in our simulation even 5 years were inadequate. Periodic signals and other noise make it more difficult to detect random walk noise, implying that it will be some time before GPS time series can be analyzed for accurate estimates of random walk noise.

### 3.2.2 Maximum Likelihood Estimation

Assuming the observed time series  $\vec{x} = \{x_j, t_j \ (j=1, N)\}$  is comprised of only white noise with variance  $\sigma_w^2$ , random-walk noise  $\sigma_{rw}^2$  (variance over specific time, e.g. one year) and flicker noise  $\sigma_f^2$  (its scale will be defined later), the covariance matrix of observations can be written as

$$Q_{xx} = \sigma_w^2 I + \sigma_{rw}^2 R_{rw} + \sigma_f^2 R_f \quad (3.12)$$

where  $I$  is the  $N \times N$  unit matrix,  $R_{rw}$  and  $R_f$  are the matrices representing the covariance of random walk noise and flicker noise, respectively, for the data which are scaled by variance.

The random walk process is derived by integrating white noise. As we do not have any information on the random walk process before observations start, we have to assume

that random walk noise at time  $t_0$  is equal to zero. With this assumption, the observed time series over a fixed time  $T$  is stationary, and easily characterized statistically, although a random walk process itself is non-stationary. We already used this assumption in our spectral analysis. The matrix  $R$  can be expressed as the following equation [*Johnson and Wyatt, 1994*]:

$$R_{rw} = \begin{pmatrix} \Delta t_1 & \Delta t_1 & \cdots & \Delta t_1 \\ \Delta t_1 & \Delta t_2 & \cdots & \Delta t_2 \\ \vdots & \vdots & \ddots & \vdots \\ \Delta t_1 & \Delta t_2 & \cdots & \Delta t_n \end{pmatrix} \quad (3.13)$$

where  $\Delta t_j = t_j - t_0$ .

For flicker noise ( $\alpha = 1$ ), the elements of matrix  $R_f$  can be approximated by [*Zhang et al., 1997*]:

$$r_{ij} = \begin{cases} \left(\frac{3}{4}\right)^2 \times 2 & i = j \\ \left(\frac{3}{4}\right)^2 \times \left(2 - \frac{\log|t_i - t_j| / \log 2 + 2}{12}\right) & i \neq j \end{cases} \quad (3.14)$$

for most space geodetic time series ( $|t_i - t_j| \ll 2^{22}$ ). The first several elements look like:

$$R_f = \begin{pmatrix} 1.125 & 1.031 & 0.984 & \dots \\ 1.031 & 1.125 & 1.031 & \dots \\ 0.984 & 1.031 & 1.125 & \dots \\ \vdots & \vdots & \vdots & \ddots \end{pmatrix} \quad (3.15)$$

The constants in equation (3.14) are chosen such that both the flicker noise and random walk noise, with equal variance and sampling interval of one day, have equivalent power levels over a period of one year. The scale of flicker noise is also defined by equation (3.14). Here, we treat flicker noise as a stationary process, although it is actually on the boundary between stationary and non-stationary behavior.

The  $\sigma_w$ ,  $\sigma_{rw}$ , and  $\sigma_f$  can be estimated by finding those values that maximize the following likelihood function, which is the joint probability of the data set [*Langbein and Johnson, 1997*]:

$$L(\vec{x}; \sigma_w, \sigma_{rw}, \sigma_f) = (2\pi)^{-N/2} |Q_{xx}|^{-1/2} \exp\left(-\frac{1}{2} \vec{x} Q_{xx}^{-1} \vec{x}\right) \quad (3.17)$$

Applying natural logarithms to both sides, we obtain

$$\ln L(\vec{x}; \sigma_w, \sigma_{rw}, \sigma_f) = -\frac{N}{2} \ln(2\pi) - \frac{1}{2} \ln|Q_{xx}| - \frac{1}{2} \vec{x} Q_{xx}^{-1} \vec{x} \quad (3.18)$$

For most available time series, only one of  $\sigma_{rw}$  and  $\sigma_f$  can be estimated at a time. We can either use the preceding spectral analysis as a guide to an appropriate noise model

or use MLE to test several noise models. We did both. The maximum likelihood problem can solved in several ways [e.g., *Kock*, 1986; *Press et. al.*, 1992]. We selected the downhill simplex method developed by Nelder and Mead [*Press et. al.*, 1992]. The method requires only function evaluations, not derivatives, although it is not very efficient in terms of the number of function evaluations required. The algorithm starts with an initial guess of an  $N$ -vector of independent parameters, then moves down gradually through the complexity of an  $N$ -dimensional topography until reaching a minimum. Each step, which is called a reflection, moves the point of the simplex, where the function is largest or highest, through the opposite face of the simplex to a lower point.

### 3.3 Results and Discussion

#### 3.3.1 Spectral Index and Noise Amplitude

We selected 23 stations with time spans longer than 2.5 years for noise analysis (Table 3.2, Figure 3.1). Seventeen stations have 3.0 years or more of data. Table 3.3 shows the spectral index estimates for north, east and vertical components of these stations. The spectral indices range from 0.51 to 2.17, with an unweighted mean of  $1.02 \pm 0.37$ , which is bigger than 0.4 estimated by *Zhang et al.* [1997]. The most reliable estimates (uncertainty less than or equal to 0.50) lie in the range of 0.51 - 1.66. Although the mean spectral index is close to 1.0, we cannot preclude the possibility that  $\alpha < 1.0$  or  $\alpha > 1.0$  (fractal white noise or fractal random walk noise), given the uncertainties and



**Table 3.3 Station Time Series: Length and Spectral Index Estimates**

ID	Span <sup>1</sup>	pts	North ( $\alpha$ )	East ( $\alpha$ )	Vertical ( $\alpha$ )
ALGO	3.4	864	1.38±0.56	1.63±0.70	0.69±0.21
BRMU	3.6	803	- <sup>2</sup>	1.66±0.50	2.17±0.80
CASA	3.4	801	1.22±0.56	0.70±0.19	0.87±0.48
CMBB	3.3	498	0.71±0.55	-	1.17±0.43
FAIR	3.4	381	0.54±0.38	-	1.10±0.81
FORT	3.8	589	0.93±0.45	0.95±0.62	0.61±0.55
GOLD	3.6	487	-	1.06±0.45	1.06±0.54
GUAM	2.8	681	-	-	-
KERG	2.6	762	0.91±0.18	1.04±0.57	1.91±1.50
KIT3	2.7	620	0.86±0.20	0.79±0.47	1.03±0.46
KOKB	3.4	824	1.30±0.56	0.53±0.22	1.39±0.41
KOUR	3.6	627	-	0.75±0.42	0.74±0.32
KRAK	2.9	627	1.13±0.23	0.51±0.34	0.83±0.28
MAS1	3.0	581	1.47±0.62	0.55±0.31	1.04±0.25
ONSA	3.2	524	1.14±0.40	0.91±0.32	1.13±0.45
PIE1	3.6	606	-	0.75±0.40	1.24±0.59
QUIN	3.4	818	1.47±0.66	1.23±0.44	0.83±0.42
RCM5	2.7	554	-	0.52±0.59	1.34±0.64
SANT	3.6	568	0.56±0.48	0.61±0.42	1.56±0.73
SHAO	2.8	764	0.81±0.44	-	1.49±0.63
TIDB	3.4	853	1.41±0.50	0.74±0.43	1.15±0.47
YAR1	3.4	833	-	0.64±0.35	0.63±0.67
YELL	3.4	538	-	0.68±0.28	0.93±0.64

1. Span in years. 2. - Failed to estimate spectral index.

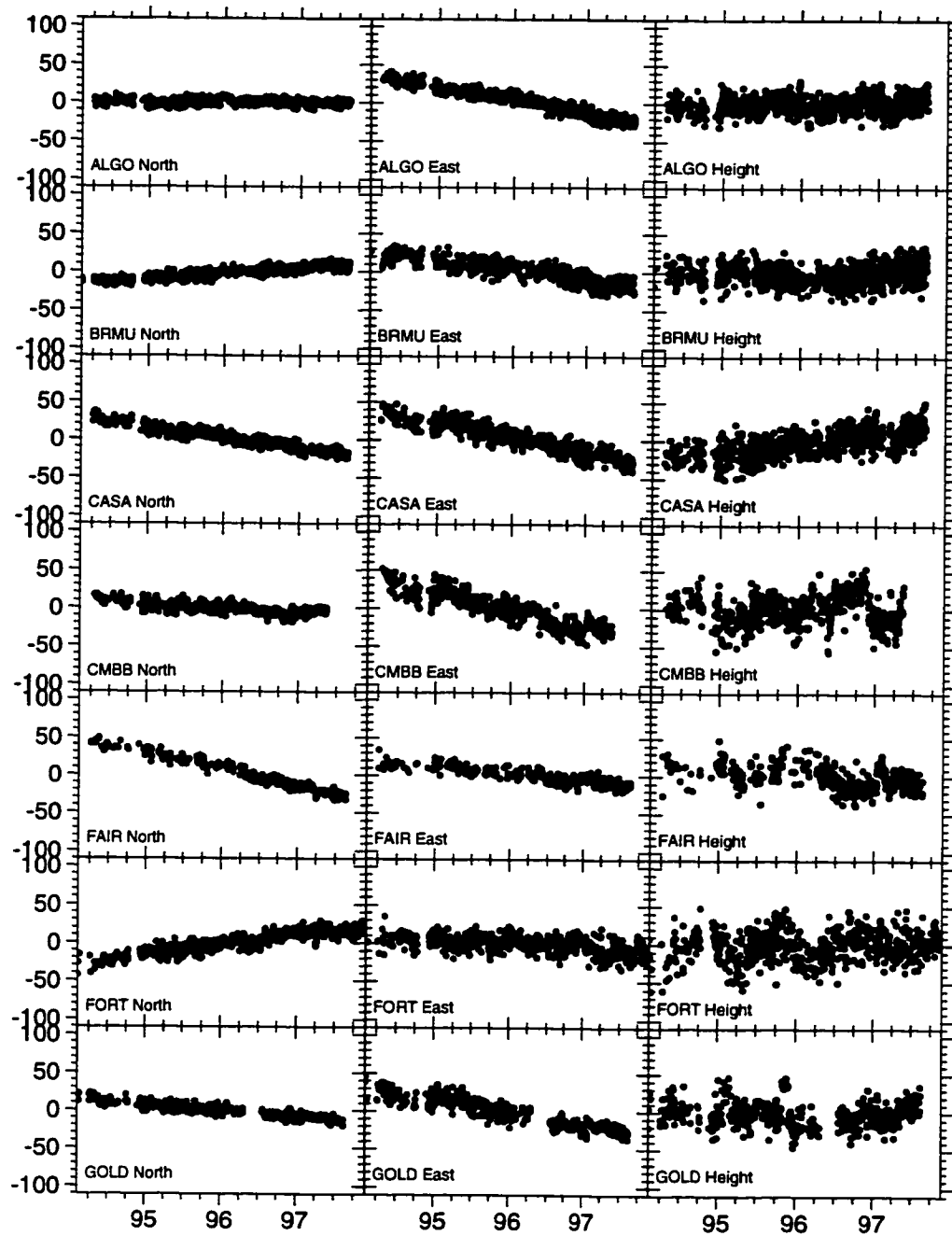


Figure 3.3 GPS coordinate time series used in this study. Abscissa is CE years -1900. Ordinate is north, east and vertical components (offset by a nominal value) in mm.

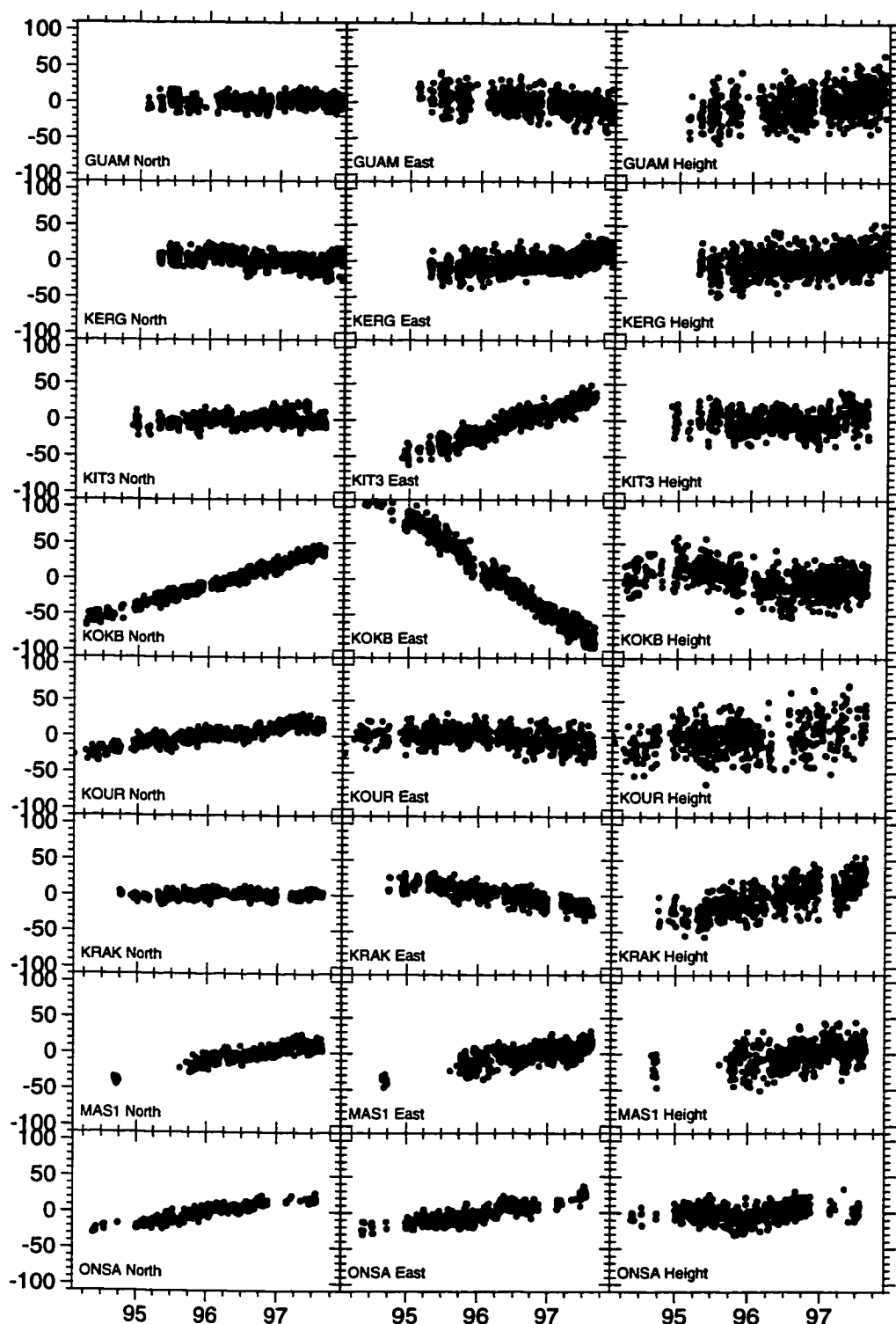


Figure 3.3 (Continued)

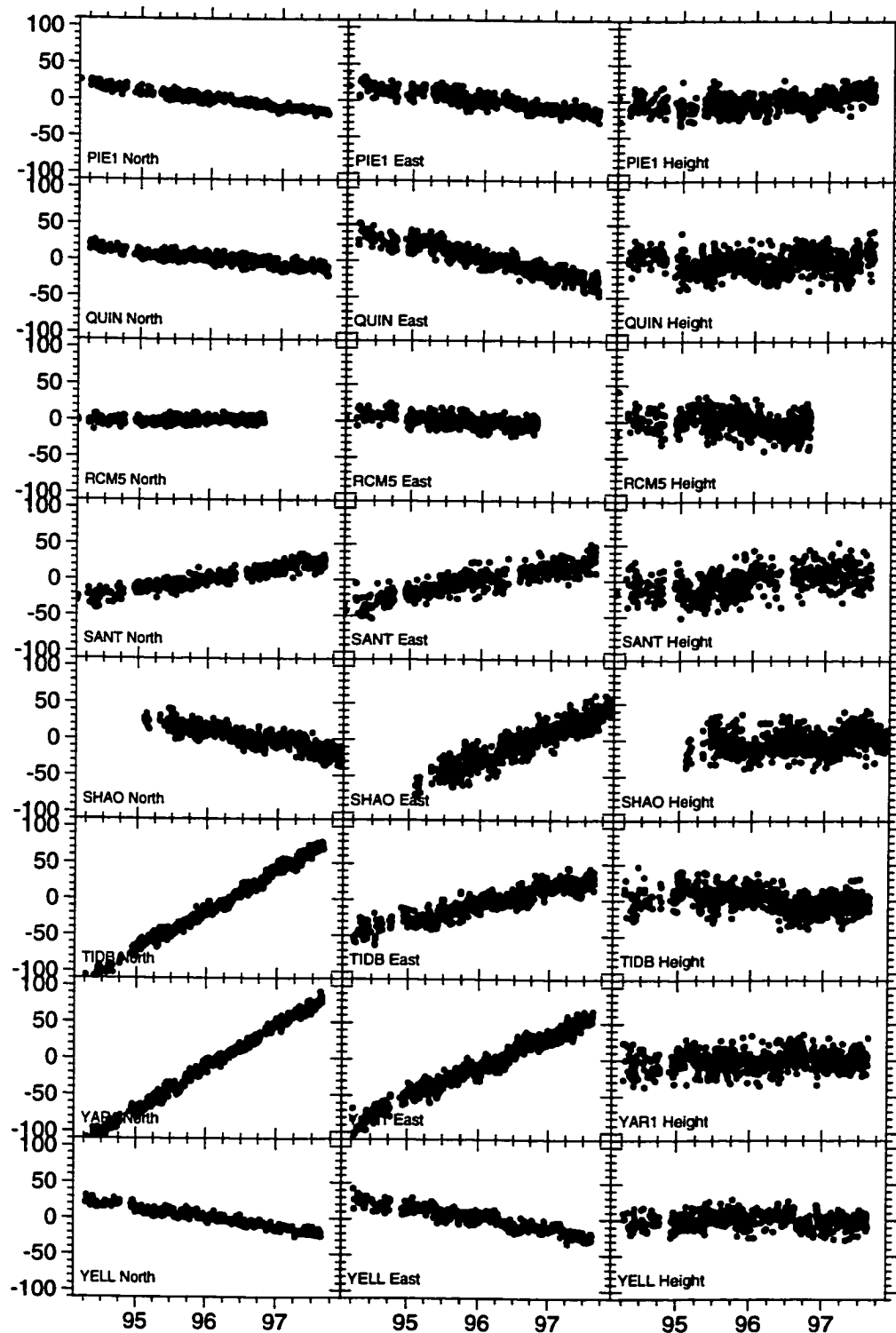


Figure 3.3 (Continued)

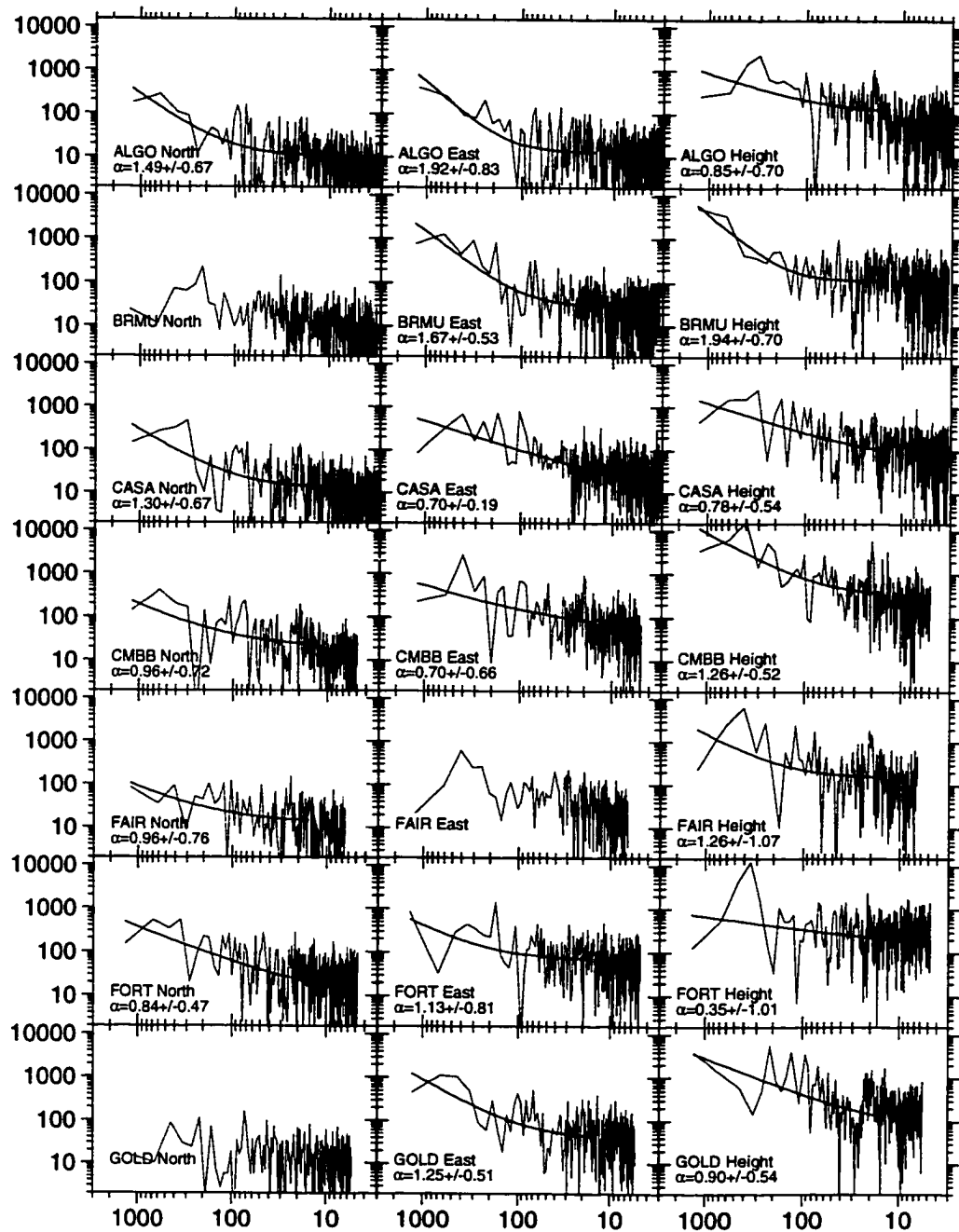


Figure 3.4 Power spectra of the GPS time series shown in Figure 3.3.  $\alpha$  is estimated spectral index. Abscissa is period in days. Ordinate is in mm<sup>2</sup>.

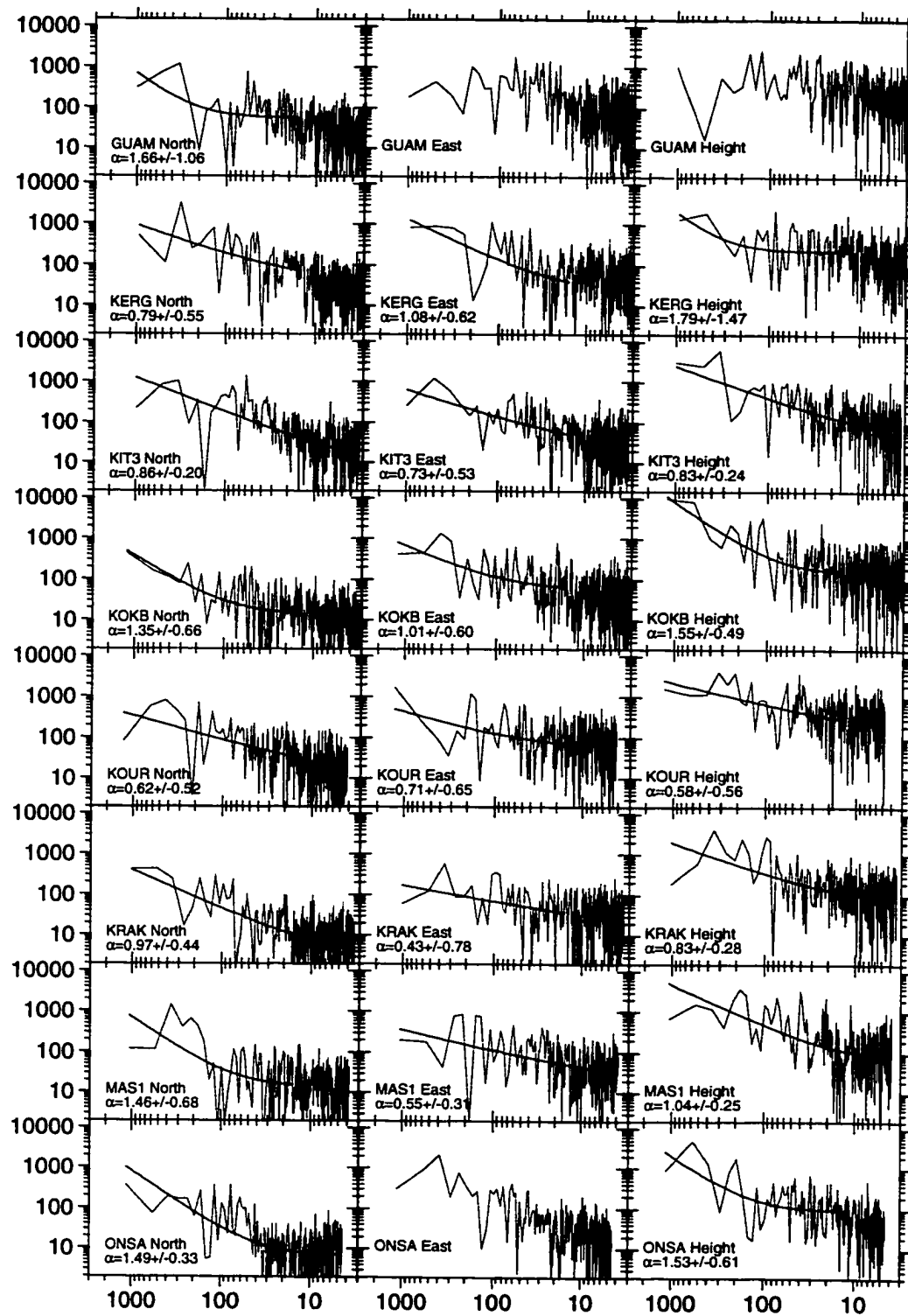


Figure 3.4 (Continued)

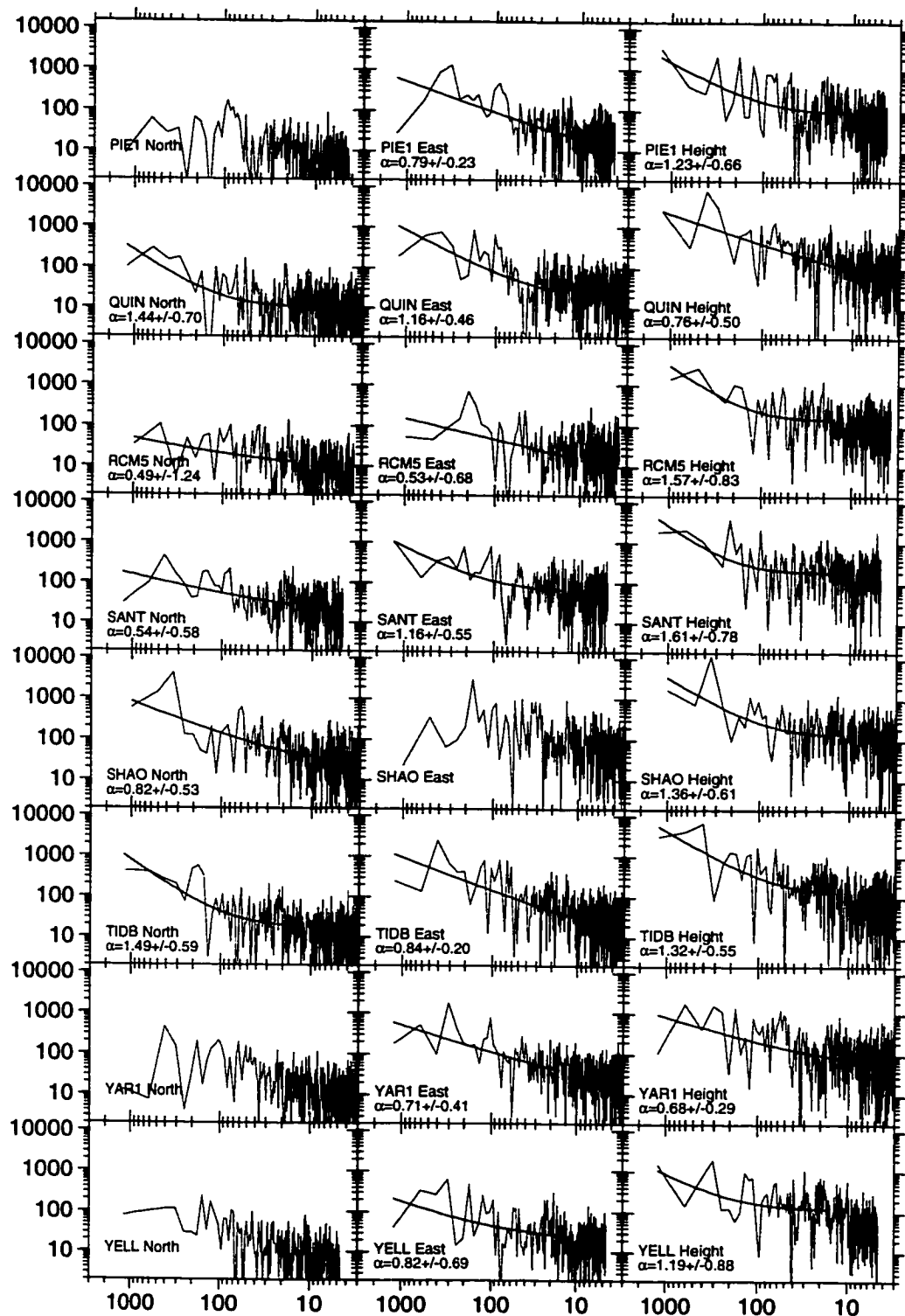


Figure 3.4 (Continued)

We tested solutions with and without an annual term removed. For most solutions the results are equivalent within errors. However, when the annual term is removed, a larger number of solutions failed to converge. For the spectral index results discussed here, we therefore retained the annual signature. However, for all other results (e.g., MLE) the annual term has been removed to avoid contaminating the low frequency part of power spectrum with a known signal, as random noise correlated over long time span is the main interest in this research.

Table 3.4 lists the log of maximum likelihood of three models, i.e. white noise, white noise plus flicker noise, and white noise plus random walk noise. For all time series, the white noise plus flicker noise model has the largest maximum likelihood, which indicates that this model is the best of three noise models studied. Thus, both the spectral analysis and Maximum Likelihood Estimation are consistent with a white plus flicker noise model.



Table 3.5 lists the noise amplitude and standard deviation of white noise and flicker noise for the various time series. The annual signal is removed before estimating the noise components. Overall, noise in the east component is slightly higher than the north component, except two sites (ALGO and KIT3). The vertical component always has the largest white noise and flicker noise magnitude. The vertical component of site CMBB has the largest flicker noise, which may be related to its older antenna (Table 3.2) and possibly higher sensitivity to multipath. For individual components, there is no significant correlation between the magnitudes of white and flicker noise, although there is a good overall correlation in the combination (Figure 3.5). The mean white noise amplitudes are 3.3, 5.9 and 10.3 mm for the north, east and vertical components. The corresponding flicker noise values are 5.7, 7.8, and 14.7 mm.



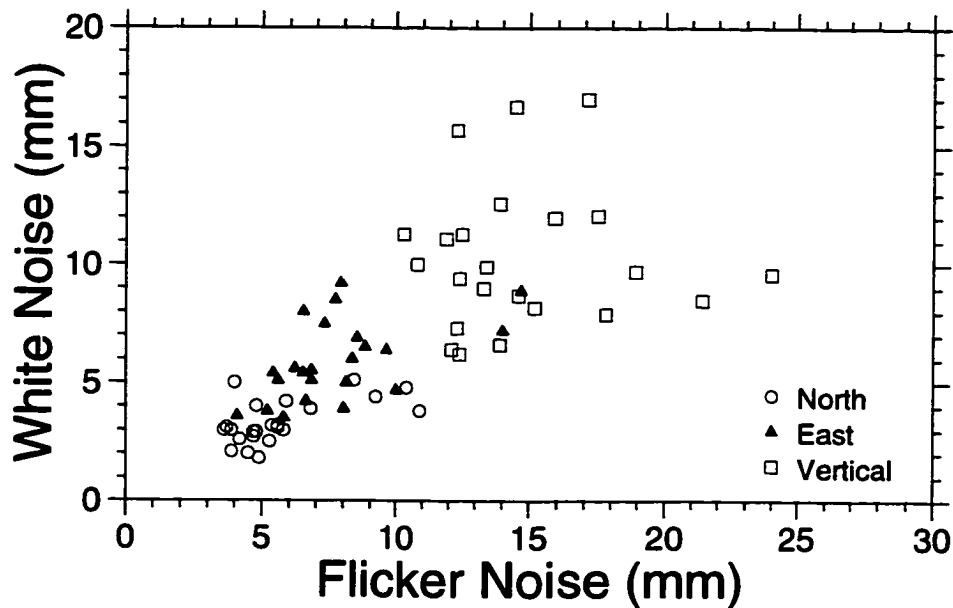
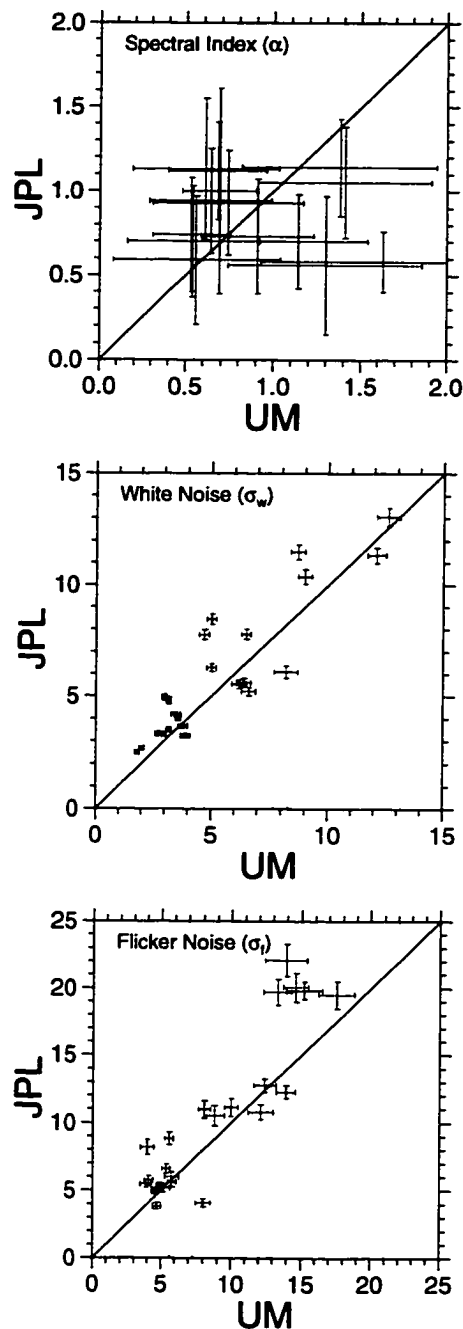


Figure 3.5 White noise vs. flicker noise amplitude for the 23 GPS time series.

In order to test the possibility that our results are biased due to time series that are too short, we applied our analysis to some GPS time series that are over 6.0 years in length [Heflin, 1997]. We found that the two results are very close for most of the sites (Figure 3.6), which suggests that our results based on 3.0 years adequately characterize the noise.



**Figure 3.6** Comparison of spectral index ( $\alpha$ ) and amplitude of white and flicker noise computed for 3 year time series (this study) and 6 year time series [Heflin, 1997] for sites where both are available. Solid line has slope of 1.00. 1- $\sigma$  error bars are also shown in figures.

### 3.3.2 Regional and Other Correlations

We expected to see some correlation between noise and general station location, e.g., tropical stations with higher vertical noise (perhaps reflecting atmospheric effects) or southern hemisphere stations with higher noise in all components (perhaps reflecting orbit/reference frame effects). Figure 3.7 plots the white and flicker noise amplitude as a function of station latitude. In general, regional effects on noise character are small and not significant. There are no obvious regional effects on flicker noise for any component. White noise increases from north to south for all 3 components, but the effect is small and not significant. Thus, southern hemisphere stations are not significantly noisier than northern hemisphere stations, implying that existing global station distribution and satellite ephemerides adequately describe spacecraft orbits and define the global reference frame given other noise sources. However, Figure 3.7 suggests that tropical stations (between  $-23^{\circ}$  and  $+23^{\circ}$  latitude) have somewhat higher levels of white noise in the vertical component. This may reflect noise related to tropospheric water vapor, which exhibits higher levels and higher variability in tropical regions [e.g., *Dixon and Kornreich Wolf, 1990*]. Since this noise is white, it is easily reduced by the frequent sampling inherent in a permanent station. This suggests that for applications requiring high quality vertical velocity, it is advantageous to have permanent stations.

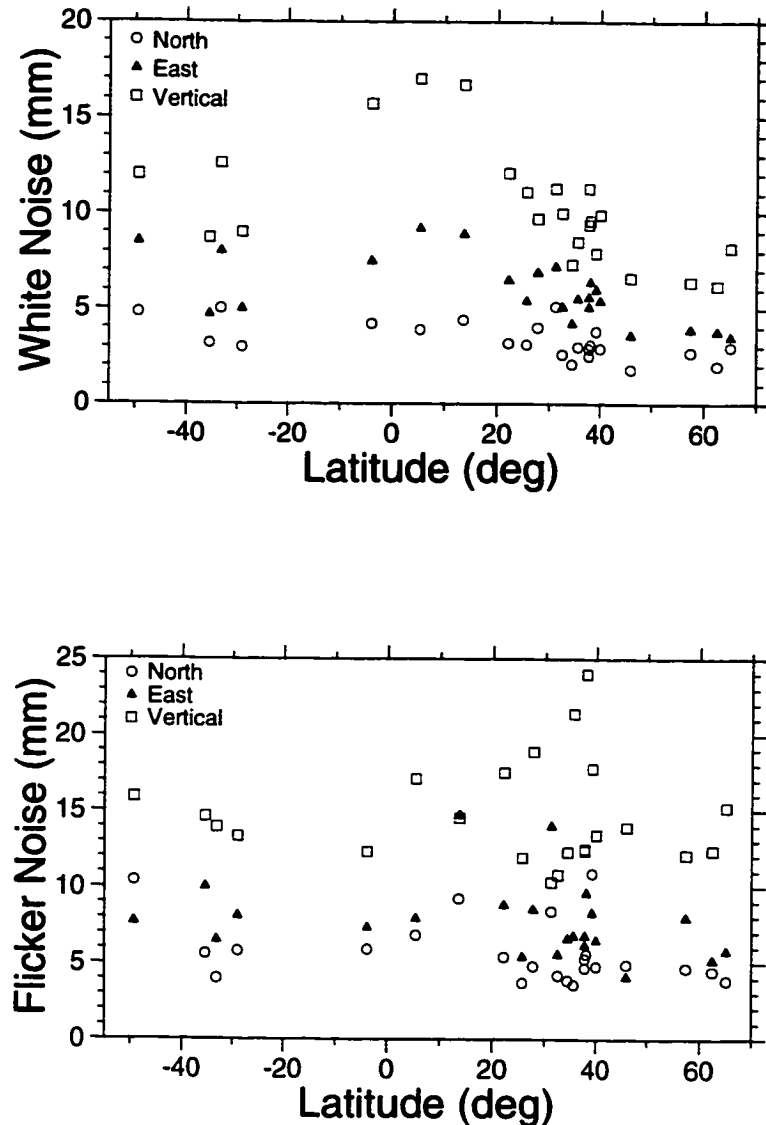


Figure 3.7 White and flicker noise as a function of latitude.

### 3.3.3 Effect of Time Correlated Noise on Velocity Estimation

The standard error of a rate ( $\sigma_r$ ) estimated in a linear regression of evenly spaced measurements can be expressed for pure white noise:

$$(\sigma_r)_w \equiv \frac{2\sqrt{3}\sigma_w}{N^{1/2}T} = \frac{2\sqrt{3}\sigma_w}{f_s^{1/2}T^{3/2}} \quad N \gg 1 \quad (3.19)$$

and for random walk noise:

$$(\sigma_r)_{rw} \equiv \frac{\sigma_{rw}}{T^{1/2}} \quad N \gg 1 \quad (3.20)$$

where  $T$  is the time span,  $f_s$  is the sampling frequency, and  $\sigma_w$  and  $\sigma_{rw}$  are the standard deviations of white and random walk noise. Thus, for purely white noise the rate error will be reduced by a factor of  $T^{3/2}$ , while for random walk noise the rate error is only reduced by a factor of  $T^{1/2}$  and not reduced by more frequent measurements. Figure 3.8a shows the effects of various combinations of white, flicker and random walk noise on rate estimation of linear regression for time series of different lengths. The rate errors decrease more slowly for time series containing significant time-correlated noise, especially for long time series. For flicker noise, the relation of rate error and time span is  $\sigma_r \sim \sigma_f/T$ . We also calculated the velocity errors of these GPS sites based on the model of white noise plus flicker noise (Table 3.6). If only white noise is assumed, velocity errors are underestimated by factors of 5-11.

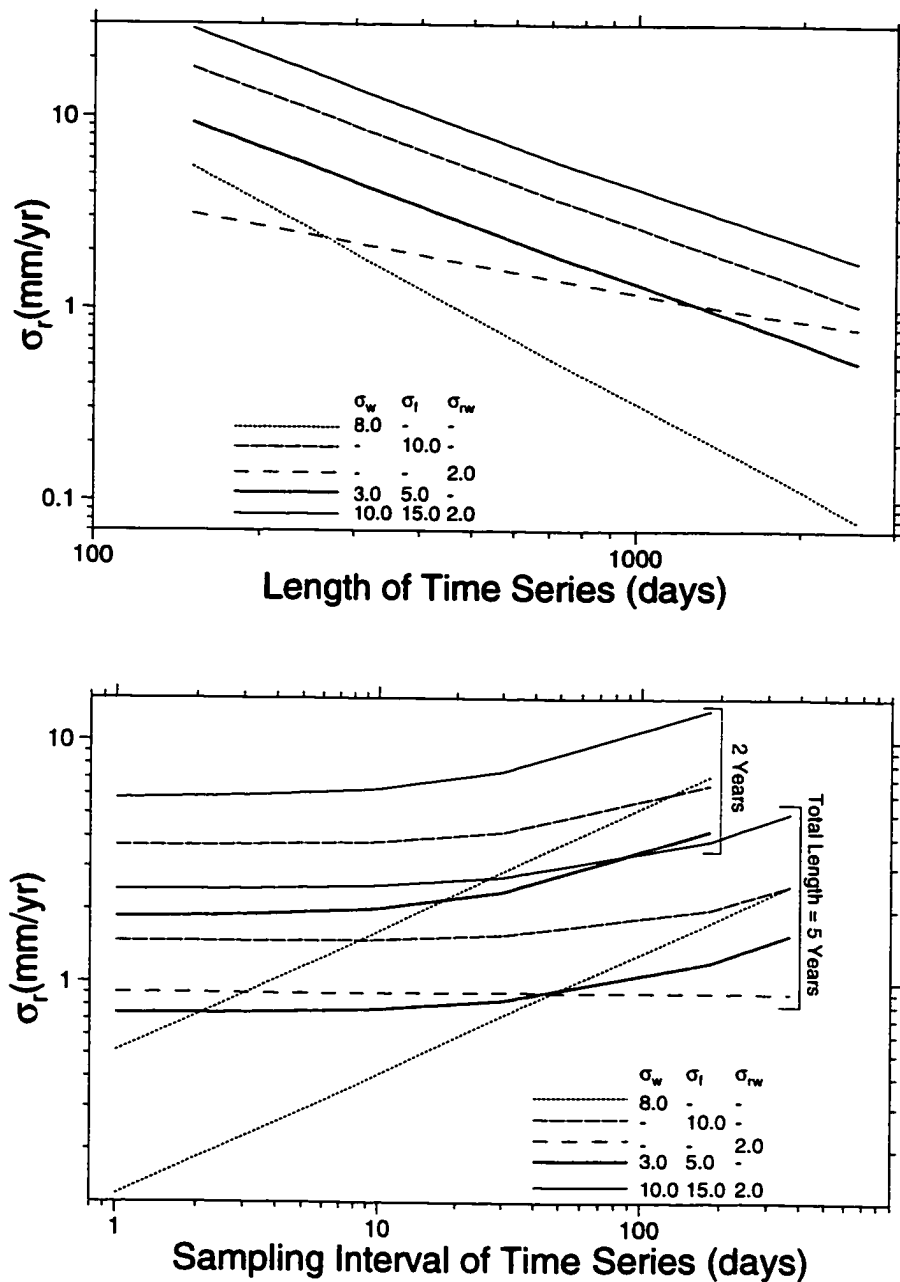


Figure 3.8 Velocity errors for time series with different lengths or sampling intervals. In addition to time series of pure white noise, flicker noise and random walk noise, the table also shows the best case ( $\sigma_w = \pm 3\text{mm}$  and  $\sigma_f = \pm 5\text{mm}$ ) and worst case ( $\sigma_w = \pm 3\text{mm}$ ,  $\sigma_f = \pm 5\text{mm}$  and  $\sigma_{rw} = \pm 2\text{mm}/\sqrt{\text{yr}}$ ) based on Table 3.5 and *Langbein and Johnson [1997]*.



white noise and flicker noise, although less efficient for the latter, but makes no change to random walk noise. Nevertheless, continuous measurements provide a time series that help us understand and evaluate monument and other time-correlated noise. Temporal correlation, whether periodic or random, can be detected, enabling correction of problem sites, whose data can be affected by weather patterns, groundwater conditions, poor monument construction, or other effects. Continuous measurements from permanent stations can also reduce the error in instrument heights and offsets due to equipment changes, difficult to detect with infrequent measurement.

### 3.4 Conclusions

1. Spectral analysis of GPS coordinate time series spanning about three years suggests that the noise characteristics of all three components can be modeled by a combination of white plus flicker noise.
2. Both white and flicker noise amplitudes increase in the order north, east and vertical.
3. The white noise part of the vertical component is higher for tropical ( $\pm 23^\circ$  latitude) stations compared to mid-latitude stations, which may be related to high wet tropospheric path delay and/or higher variability.
4. Southern hemisphere stations are not significantly noisier than northern hemisphere stations.
5. The velocity error in coordinate time series may be underestimated by factors of 5-11 if a pure white noise model is assumed.

## **CHAPTER 4      Rigidity of the North American Plate Interior**

### **4.1      Introduction**

A fundamental tenet of plate tectonics is that relative motion between plates is accommodated in narrow plate boundaries, while plate interiors are rigid. However, the occurrence of large intraplate earthquakes such as the 1811-1812 New Madrid events [Nuttli, 1982] argues that some deformation occurs within plates.

Space geodesy can rigorously test the concept of plate rigidity. The good agreement between space geodetic measurements of relative plate velocity based on a small number of sites per major plate and plate velocities predicted from a rigid plate model [DeMets *et al.*, 1994] demonstrates that on average most plate interiors are rigid at the level of a few mm/yr [Robbins *et al.*, 1993; Robaudo and Harrison, 1993]. However, several mm/yr represents a significant rate of deformation over geological time, perhaps explaining New Madrid seismicity.

The University of Miami's Geodesy Laboratory analyzes data from a global network of GPS sites for tectonic and coastal stability applications, including twenty stations on the stable interior of North America with 1.5-3.7 years of data from 1994 through 1997 (Table 4.1, Figure 4.1). We use the velocity data from these sites to investigate the rigidity of continental North America.

**Table 4.1 Site Description for the Data Period**

ID	Site Name	Start	End	Span <sup>1</sup>	Points <sup>2</sup>	Antenna history <sup>3</sup> and notes
ALGO	Algonquin	94apr05	97dec27	3.7	889	TR; TR(94may18); TR(97jan16)
ARP3	Aransas Pass	96feb01	97dec27	1.9	601	ASH; CORS site
BRMU	Bermuda	94apr05	97dec27	3.7	824	TR
CHA1	Charleston	95dec03	97dec27	2.1	608	ASH; CORS site
CHUR	Churchill	96jul04	97dec27	1.5	266	TR
DET1	Detroit	96jul04	97dec27	1.5	261	ASH; CORS site
DRAO	Penticton	96jul04	97dec27	1.5	271	TR; TR(95apr12)
FAIR	Fairbank	94apr05	97dec25	3.7	403	Rogue; TR(96apr16)
FLIN	Flin Flon	96jul04	97dec27	1.5	271	TR; add acrylic dome (97jan01)
GODE	Greenbelt	96jul08	97dec25	1.5	267	TR
MDO1	McDonald	96jul05	97dec27	1.5	270	TR
MIA1	Miami	95dec03	97dec27	2.1	630	ASH; CORS site
NLIB	North Liberty	94aug11	97dec25	3.4	366	TR
PIE1	Pietown	94apr05	97dec27	3.7	599	TR
RCM5	Richmond	94apr05	96oct09	2.5	448	TR
STJO	St. John's	94apr05	97dec27	3.7	535	TR, changed 4 times <sup>3</sup>
TMGO	Boulder	96jul04	97dec27	1.5	260	TR; TR (95apr08); TR(95oct04)
WES2	Westford	96jan02	97dec27	2.0	278	TR, changed 5 times <sup>4</sup>
WHIT	White Horse	96jul04	97dec27	1.5	261	TR; TR(97jun24);
YELL	Yellowknife	94apr10	97dec27	3.7	502	TR; TR (94oct14); TR(96aug22)

1. Spans in years.

2. Number of observation days.

3. TR = Turbo Rogue antenna; ASH = Ashtech Geodetic L1-L2 antenna.

4. Dates of antenna changes at STJO: 95feb26, 95mar02, 95nov03, 96aug01.

5. Dates of antenna changes at WES2: 96mar29, 96jun11, 96jul01, 97may22, 97jun30.

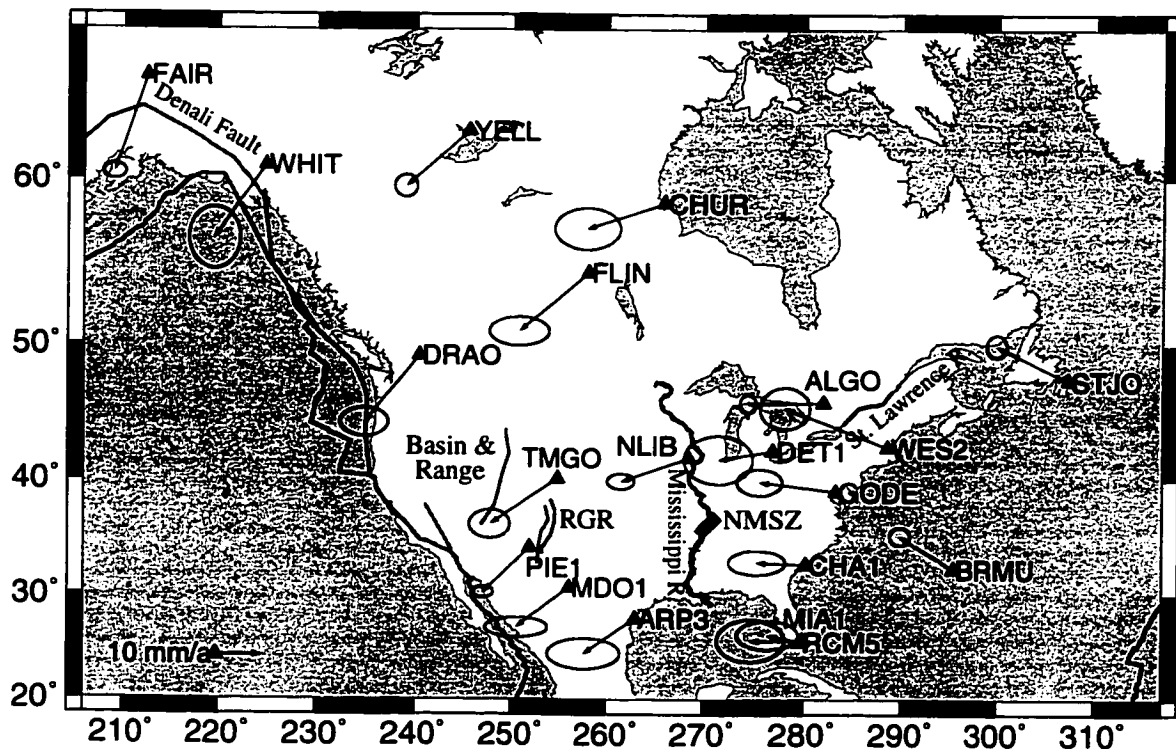


Figure 4.1 Stations used in this study, their GPS-derived velocities in ITRF96 and 95% confidence ellipses. Major tectonic features discussed in text are also shown. RGR is Rio Grande Rift; NMSZ in New Madrid Seismic Zone. Note general rotation of sites about an Euler pole in northwestern South America (Figure 4.11).

## 4.2 Data Analysis

### 4.2.1 Site Velocity and Accuracy Evaluation

Most sites are instrumented with standard IGS (International GPS Service for Geodynamics) systems, including Turbo Rogue GPS receivers sampling at 30 second rate, Dorn Margolin antennas and choke ring backplanes. Four CORS sites (ARP3, CHA1, DET1 and MIA1) are Coast Guard navigation beacons, equipped with Ashtech receivers

and antennas, and are more susceptible of multipath. Their monuments were not designed for high precision geodesy. GPS data analysis is described in Chapter 2.

Station velocities are derived from station positions (daily GPS solutions) defined in global reference frame ITRF-96 [Boucher, 1998]. For each coordinate component (north, east and vertical), a straight line is fitted to a set of  $n$  data points  $(x_i, t_i)$  with standard deviation  $\sigma_i$  (assuming data are not time-correlated):

$$x_i = a + bt_i + v_i \quad (4.1)$$

where  $a$  is the intercept,  $b$  is the slope or velocity, and  $v_i$  is measurement error. This problem is often called linear regression. The estimates of  $a$  and  $b$  based on weighted least squares can be written as [Press *et al.*, 1992]

$$a = \left( \sum_{i=1}^n t_i^2 / \sigma_i^2 \sum_{i=1}^n x_i / \sigma_i^2 - \sum_{i=1}^n t_i / \sigma_i^2 \sum_{i=1}^n t_i x_i / \sigma_i^2 \right) / \Delta \quad (4.2)$$

$$b = \left( \sum_{i=1}^n 1 / \sigma_i^2 \sum_{i=1}^n t_i x_i / \sigma_i^2 - \sum_{i=1}^n t_i / \sigma_i^2 \sum_{i=1}^n x_i / \sigma_i^2 \right) / \Delta \quad (4.3)$$

where  $\Delta = \sum_{i=1}^n 1 / \sigma_i^2 \cdot \sum_{i=1}^n t_i^2 / \sigma_i^2 - \left( \sum_{i=1}^n t_i / \sigma_i^2 \right)^2$ . The variances and correlation are

$$\sigma_a^2 = \left( \sum_{i=1}^n t_i^2 / \sigma_i^2 \right) / \Delta \quad (4.4)$$

$$\sigma_b^2 = \left( \sum_{i=1}^n 1 / \sigma_i^2 \right) / \Delta \quad (4.5)$$

$$r_{ab} = \left( - \sum_{i=1}^n t_i / \sigma_i^2 \right) / \sqrt{\sum_{i=1}^n t_i^2 / \sigma_i^2 \cdot \sum_{i=1}^n 1 / \sigma_i^2} \quad (4.6)$$

The reduced chi-squares ( $\chi_r^2$ ) shows how well the linear model agrees with the data:

$$\chi_r^2 = \frac{1}{n-2} \sum_{i=1}^n (x_i - a - bt_i)^2 / \sigma_i^2 \quad (4.7)$$

If the standard deviation of data ( $\sigma_i$ ) is correct,  $\chi_r^2$  has a mean equal to one. The square root of  $\chi_r^2$  can be used to scale the formal errors of data and estimates, if it is not equal to one. A data point whose absolute value of residual is larger than several times its standard deviation can be treated as an outlier, and removed from the linear regression. This procedure has to be done iteratively. We consider data points with absolute residual larger than 3 times of the standard deviation scaled by  $\chi_r^2$  as outliers. Fewer than 1% of data points are removed from our GPS time series with this criterion. The overall data quality can also be shown by weighted root mean square (wrms) scatters of the daily position

estimates about the best fit lines. In order to improve the numerical stability,  $t_i$  can be shifted with its mean value before estimation.

Because of the large number of processes affecting the GPS observables, the observables cannot be modeled perfectly. Especially when precise satellite orbit and clock information is used in GPS data analysis to reduce processing time (see Chapter 2), errors in the satellite orbits and clocks are currently not accounted for. The formal errors of site coordinates derived from GPS data with GIPSY software are therefore underestimated. Errors for north, east and vertical components are underestimated by different amounts, as shown by different reduced chi-squares in the linear regression analysis. Usually the north component has the largest  $\chi^2_r$ , while the vertical component has the smallest. Furthermore, as we discussed in the previous chapter, the GPS time series also contain time-correlated noise. By examination of position time series over longer spans, it is found that some time series do not evolve with a constant rate. Such changes more likely reflect measurement error and monument instability rather than tectonic motion. The rates of change for some coordinate components differ significantly over different time intervals. This problem can be illustrated by FAIR east, STJO north and east, YELL north and east components (Figure 4.2). It is therefore critical to re-evaluate the formal errors of velocities, as the following statistical tests of plate rigidity are highly dependent on the errors assigned to the site velocities.

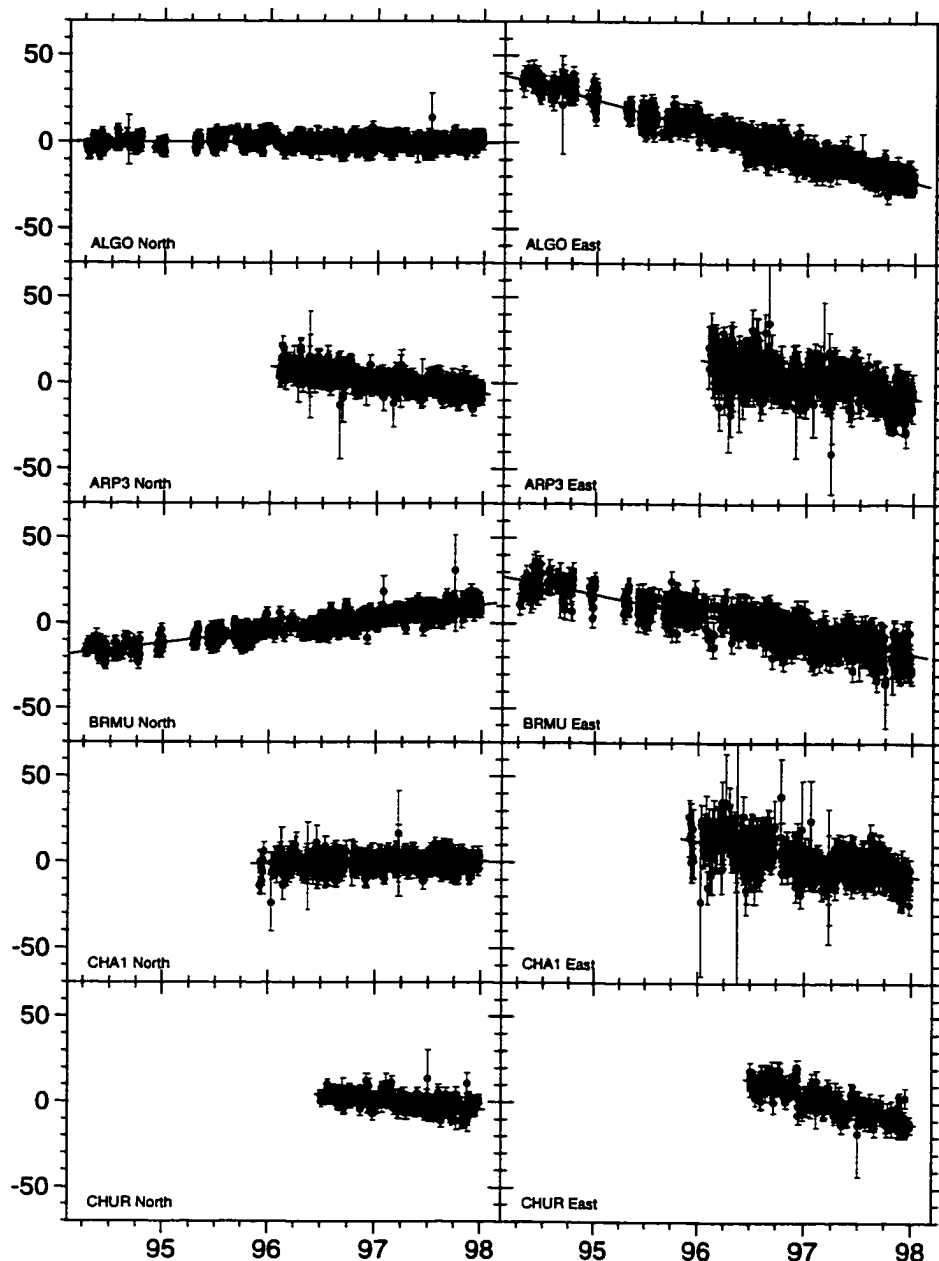


Figure 4.2 GPS coordinate time series used in this study. The horizontal axes are CE years - 1900. The vertical axes are east and north components (offset by a nominal value) in mm.

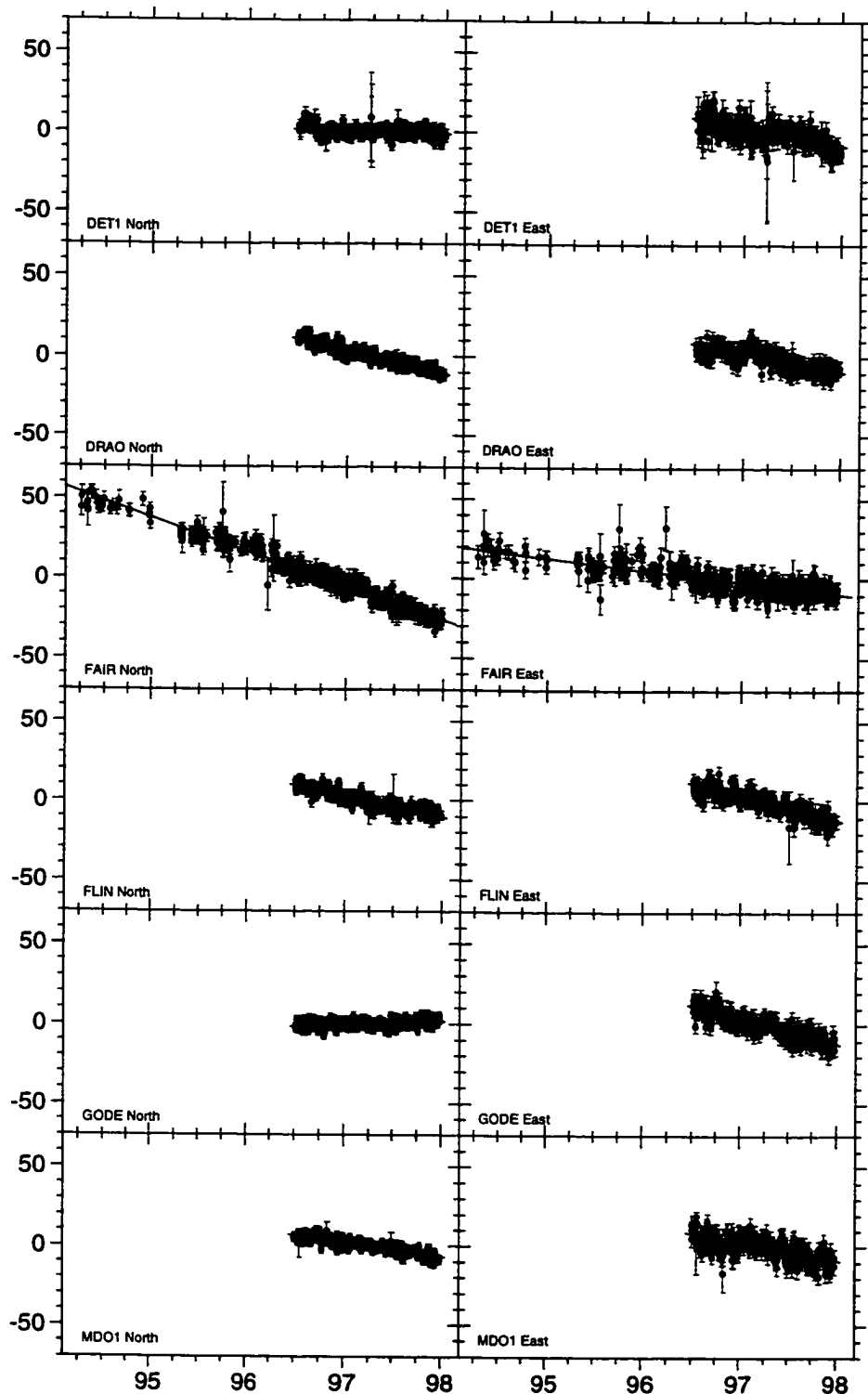


Figure 4.2 (Continued)

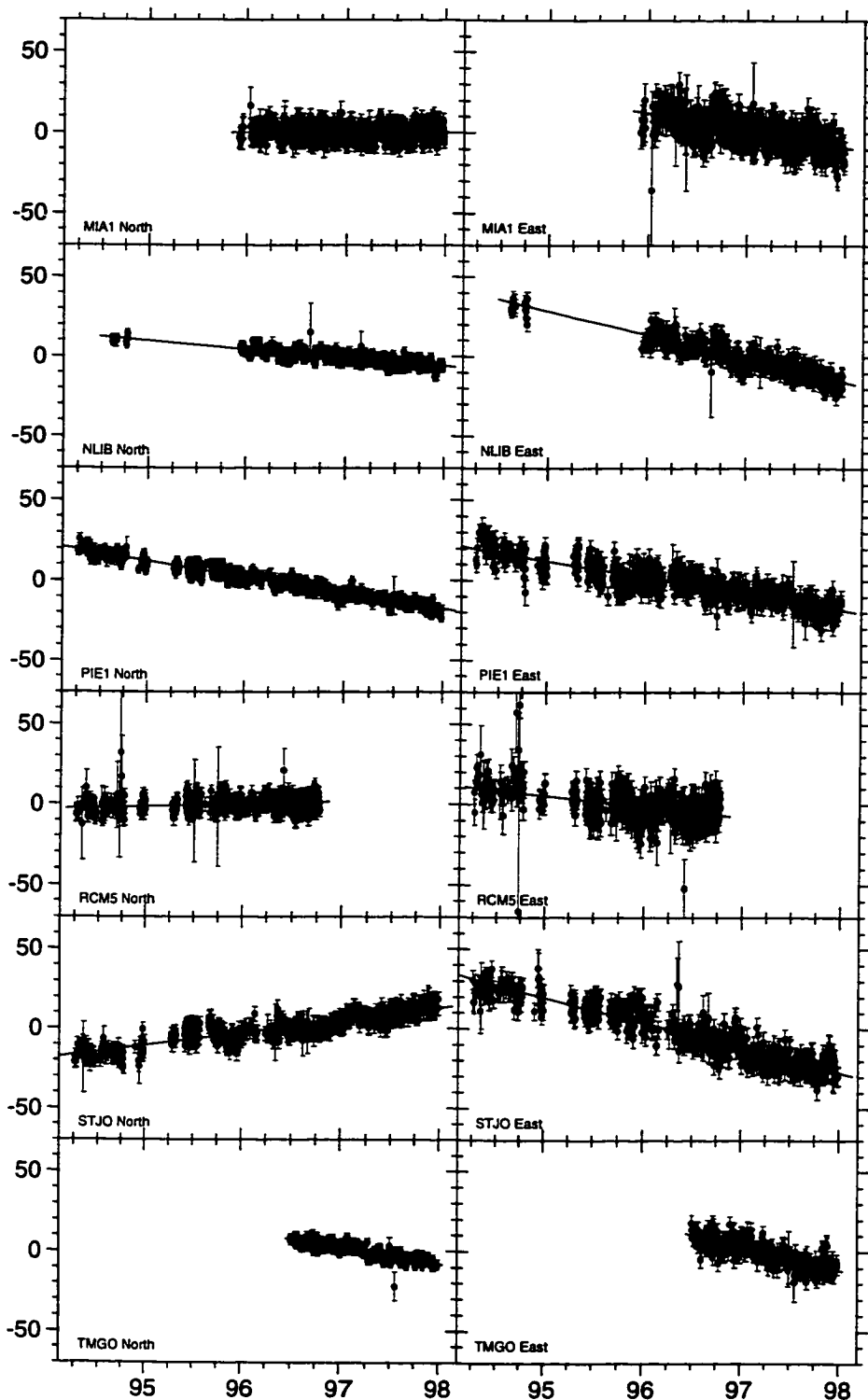


Figure 4.2 (Continued)

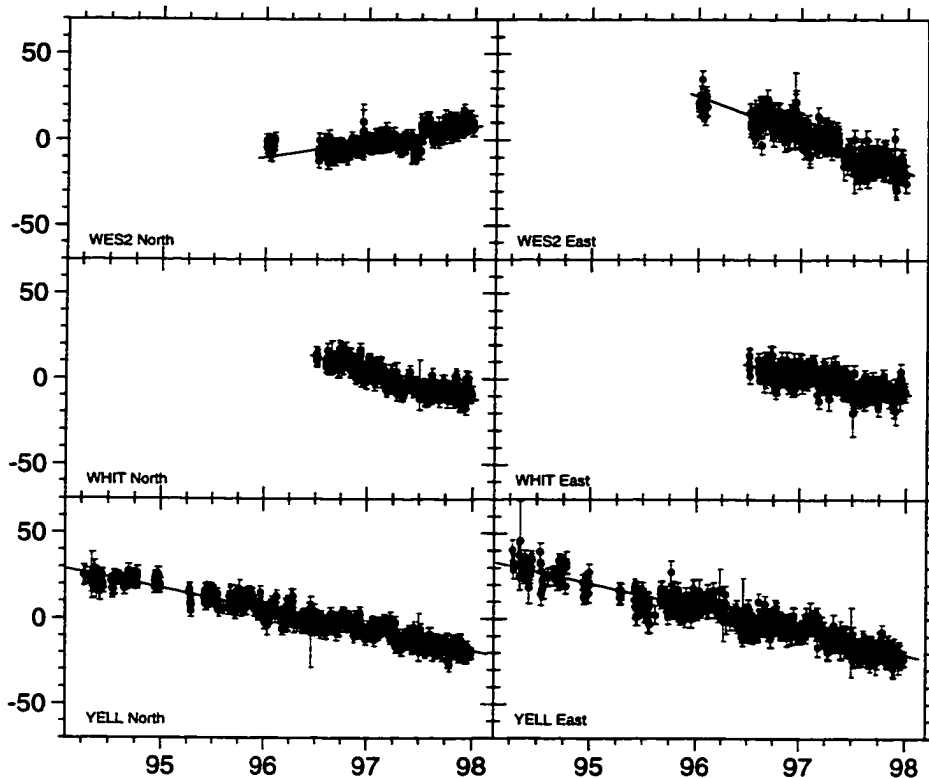


Figure 4.2 (Continued)

The strict way to evaluate the velocity errors is to characterize the noise in the time series as we showed in Chapter 3. As we found, noise in most GPS time series is close to a white plus flicker noise model. We can first estimate the magnitudes of white and flicker noise. Then a new covariance matrix of the time series is formed from the estimates of white and flicker noise components with equation (3.12), and is used to estimate velocity error. For stations with short ( $< 2$  years) time series, the estimate of colored noise may be inaccurate. For these stations, it may be advisable to use average values derived from stations with longer time series.

#### 4.2.2 Estimation of Plate Motion and Regional Deformation

For a perfectly rigid plate, there is no relative motion among sites on the plate interior. In reality, a variety of processes and errors contribute to real and apparent relative motion. Real motions include post-glacial rebound, deformation near a plate boundary, intraplate deformation on regional (>100km) scales, and local near-surface ground motion around the geodetic mark (monument instability). We define the residual velocity of a site as the velocity unexplained by motion of a perfectly rigid plate. It can be considered the vector sum of all real relative motions affecting a plate interior site and measurement errors. In discussing residuals, we consider the joint effect of monument instability and GPS errors as gaussian noise with an expectation of zero (observational error), distinguishing this from misfit due to regional scale geological processes. To test how well the GPS velocities are described by the single rigid plate model, we invert the data to find the Euler vector that best fits the GPS data, and examine how well the predicted velocities match those observed.

Because vertical site motion is assumed to be zero in plate tectonics, the Euler vector,  $\Omega=(\omega_x, \omega_y, \omega_z)^T$ , which describes the motion of a rigid plate, can be derived from the horizontal velocity of a set of sites attached to the plate with the observation equation [Ward, 1990]:

$$V = \begin{bmatrix} v_i^n \\ v_i^e \\ \vdots \end{bmatrix} = \begin{bmatrix} \hat{n}_i \cdot (\Omega \times P_i) \\ \hat{e}_i \cdot (\Omega \times P_i) \\ \vdots \end{bmatrix} + \epsilon$$

$$= \begin{bmatrix} (P_i \times \hat{n}_i)_x & (P_i \times \hat{n}_i)_y & (P_i \times \hat{n}_i)_z \\ (P_i \times \hat{e}_i)_x & (P_i \times \hat{e}_i)_y & (P_i \times \hat{e}_i)_z \\ \vdots & \vdots & \vdots \end{bmatrix} \begin{bmatrix} \omega_x \\ \omega_y \\ \omega_z \end{bmatrix} + \epsilon \quad (4.8)$$

where  $v_i^n$  and  $v_i^e$  are north and east components of velocity vector at site  $i$ ,  $P_i$  is the position vector of the site,  $\hat{n}_i$ ,  $\hat{e}_i$  are north and east directional vectors of this site and  $\epsilon$  is the observational error. The observation vector  $V$  has a covariance matrix  $Q_{vv}$ . At least two sites are required to estimate an Euler vector. The resultant Euler vector is in the same reference frame as the site velocity. The velocity at site  $P_i$ , which is attached to the plate, can be predicted from the Euler vector. The predicted velocity can be expressed explicitly with north and east components as

$$V_i^c = \Omega \times P_i = \begin{bmatrix} \hat{n}_i \cdot (\Omega \times P_i) \\ \hat{e}_i \cdot (\Omega \times P_i) \end{bmatrix} \quad (4.9)$$

If observations are made at this site, the velocity residual can be written as

$$\Delta V_i = \begin{bmatrix} v_i^n - \hat{n}_i \cdot (\Omega \times P_i) \\ v_i^e - \hat{e}_i \cdot (\Omega \times P_i) \end{bmatrix} \quad (4.10)$$

The overall quality of the rigid plate model can be measured with  $\chi^2$ , which is the sum of the squares of the differences between observations and model values, and

normalized by the covariance matrix. It can be calculated for those sites which defined the Euler vector:

$$\chi^2 = \Delta V^T Q_v^{-1} \Delta V \quad (4.11)$$

where  $\Delta V$  is the vector of north and east velocity residuals at those sites, and is equal to the difference of observed and predicted velocity. The degree of freedom is  $2n-3$ , where  $n$  is the number of sites. To show the real quality of the rigid plate model, the resultant covariance matrix of Euler vectors  $\Omega$  should be scaled by reduced chi-square:

$$\chi_r^2 = \chi^2 / (2n - 3) \quad (4.12)$$

The relative motion of two plates can be described by another Euler vector which is equal to the difference of Euler vectors of the two plates:

$$\Omega_{12} = \Omega_1 - \Omega_2 \quad (4.13)$$

Plate motion can also be described with Euler pole at latitude and longitude:

$$\varphi = \arctan(\omega_z / \sqrt{\omega_x^2 + \omega_y^2}) \quad -90^\circ < \varphi < 90^\circ \quad (4.14)$$

$$\lambda = \arctan(\omega_y / \omega_x) \quad 0^\circ < \lambda < 360^\circ \quad (4.15)$$

and angular velocity:

$$\omega = \sqrt{\omega_x^2 + \omega_y^2 + \omega_z^2} \quad (4.16)$$

#### 4.2.3 F-Test of Splitting a One-Plate Model into a Two-Plate Model

The *F*-test can be used to test if two variances are significantly different, e.g., whether  $\chi^2$  is significantly reduced simply because additional parameters are added to a model. We use it to compare how well a set of velocity observations at  $n$  sites is fitted by two different plate models, one of which has more plates than the other. The test is formed from  $\chi^2$  as defined in equation (4.11). If  $m$  data points are fit by two models with  $p$  and  $q$  parameters respectively ( $p>q$ ), the model with  $p$  parameters should fit the data better, and its  $\chi^2$  should be smaller, as the model has a lower degree of freedom ( $m-p$ ). Thus we have the following *F*-ratio [*Stein and Gordon, 1984*]:

$$F(\gamma_1, \gamma_2) = \frac{[\chi_q^2 - \chi_p^2] / \gamma_1}{\chi_p^2 / \gamma_2} \quad (4.17)$$

where  $\chi_p^2$  and  $\chi_q^2$  are chi-squares of models with  $p$  parameters and  $q$  parameters, respectively. The statistic has *F*-distribution with degrees of freedom  $\gamma_1=p-q$  and  $\gamma_2=m-p$ .

The probability of an *F*-ratio greater than the observed value with degrees of freedom  $\gamma_1$  and  $\gamma_2$  can be examined to see how reliably the model is improved. For example, if the probability is 0.01, there is only 1% risk that the improvement in fit is caused by chance. The *F*-ratios of different degrees of freedom and probability can be found in the *F*-test table of most mathematical handbooks.

In the case of adding one more plate, the number of data points is equal to  $2n$  and the degrees of freedom of the *F*-ratio in equation (4.17) are  $\gamma_1=3$  and  $\gamma_2=2n-6$ . For investigation of plate motion, the results of the *F*-test can be biased towards a model of more plates, as the additional parameters are chosen based on the residuals of data from the simpler model. From synthetic tests, the *F*-test is practical when a stringent maximum confidence level of 99% instead of 95% is used [Stein and Gordon, 1984].

#### 4.2.4 Correction of Site Velocities for Postglacial Rebound

North America is slowly adjusting from the retreat of huge continental ice sheets that covered North America at the last glaciation maximum. Three continental ice sheets (North America, Northwestern Europe, and West Antarctica) retreated after the last glaciation maximum 18,000 years ago (Late Pleistocene), significantly reducing the mass loading on these continents and leading to isostatic rebound (uplift) up to several hundred meters. However, the high viscosity of the mantle forces a slow restoration of isostasy, and the process of glacial isostatic adjustment continues even today, although the last major glacial retreat was complete more than 6000 years ago. Present-day Postglacial Rebound (PGR) is a strong function of geographic location; the surface of the solid earth

is rising as high as 10 mm/yr at sites that were once ice covered and as low as -2 mm/yr at sites immediately peripheral to the margins of the major ice sheets. The PGR horizontal motions are usually less than 1 mm/yr [Mitrovica and Forte, 1997; Peltier, 1998].

PGR is usually estimated from the deglaciation history and earth's response models. In the absence of vertical tectonic motion, the sea level history  $S(\phi, \lambda, t)$  can be expressed as the following sea-level equation [Peltier and Tushingham, 1991]:

$$S = \rho_l \frac{\phi}{g} * L_l + \rho_w \frac{\phi}{g} * S - \frac{1}{A_0} \int_{ocean} \left( \rho_l L_l * \frac{\phi}{g} + \rho_w S * \frac{\phi}{g} \right) - \frac{M_l(t)}{\rho_w A_0} \quad (4.18)$$

The first two terms are the Earth's responses to the loss of land ice  $L_l(\phi, \lambda, t)$  and increase of ocean water; the third term is related to the ocean basin change due to changes of ice and water loading; the last term is related directly to ocean water increase from global ice melting history  $M_l(t)$ .

Crucial for accurate PGR prediction are the Earth's internal radial viscoelastic structure, required to determine Green's function  $\phi$ , and the space-time history of deglaciation  $L_l(\phi, \lambda, t)$ . The Earth model assumes an elastic lithosphere, like model 1066B determined by seismology, and two layers of mantle with different viscosity [Peltier and Tushingham, 1991]. In reconstruction of the ice melting history, the usual practice is to establish isochron maps of the limits of the ice sheet as deglaciation proceeds and then predict the thickness using mechanical models for the ice sheets. The current most sophisticated deglaciation history model is ICE-4G [Peltier, 1994],

developed by iteration. The main observational data is relative sea level history in the age range of 0 to 12 ky ago based on radio-carbon dated shorelines. Other relevant data are anomalies in the Earth's rotation and the free-air gravity anomaly over the centers of PGR, which are also used iteratively to determine these functions. An independent test of ice sheet thickness at one location in Canada based on volatile equilibrium studies in sub-glacial volcanoes yields excellent agreement [Dixon *et al.*, 1998].

There is uncertainty in the predictions of surface motions produced by PGR, as discrepancies between different models (e.g., ICE-3G and ICE-4G) are still large. Reasonable changes in mantle depths and viscosity can lead to significant change in PGR predictions [Peltier, 1998]. Rigorous evaluation of such model errors is not yet possible, although our current GPS velocities yield a crude test.

### **4.3 Results**

Table 4.2 lists north and west velocity components in the global reference frame (ITRF96) and errors (one standard error) for the 20 sites. Velocity errors are estimated in two ways. The first velocity error was estimated from a pure white noise model when the data were fitted with straight lines, assuming the data points are uncorrelated. The second velocity error was estimated based on a white plus flicker noise model. The second error is about 3-8 times larger than the first error. Table 4.2 also lists the weighted root mean square (wrms) scatters of the daily position estimates about the best fit lines, typically 3-5 mm and 4-7 mm for the north and west components, respectively. Poor performance might be expected at the four Coast Guard beacon sites because of the lower quality

antennas and monuments. But our results show that they have comparable position wrms with the other IGS sites, even though larger rms of phase observations were found in daily GPS analysis. This suggests that these stations can be used for tectonic applications. Most space geodetic data show strong seasonal signals, usually with a period of about one year. For short time series spanning one to three years, such periodic signals can significantly effect the velocity estimation. One way to reduce such periodic signals is to estimate velocity from near evenly sampled time series spanning integer years. But it is difficult to comply in practice. I estimated velocities after removing annual terms and found no significant changes for all sites.

Table 4.2 North, East and Vertical GPS Site Velocities and Errors (mm/yr, ITRF96)

Site ID	$V_n$	$\sigma_n^w$	$\sigma_n^{wf}$	wrms	$V_e$	$\sigma_e^w$	$\sigma_e^{wf}$	wrms	$V_v$	$\sigma_v^w$	$\sigma_v^{wf}$	wrms
ALGO	-0.1	0.1	0.8	2.9	-15.7	0.1	0.7	4.2	2.4	0.4	2.7	10.7
ARP3	-7.9	0.3	1.4	3.6	-11.2	0.6	3.3	7.1	-9.3	1.1	11.7	14.1
BRMU	7.4	0.1	0.8	3.3	-11.6	0.2	0.9	5.9	1.6	0.4	5.7	12.3
CHA1	0.5	0.3	1.1	3.8	-10.1	0.6	2.4	6.8	-0.5	1.1	9.9	13.4
CHUR	-5.7	0.5	1.9	3.5	-17.0	0.7	3.0	4.6	15.8	1.5	5.0	10.2
DET1	-1.9	0.4	2.2	2.9	-11.4	0.8	3.0	5.0	12.5	1.5	4.7	10.2
DRAO	-14.8	0.3	1.3	2.4	-11.7	0.6	2.1	4.1	-1.4	1.4	7.9	9.8
FAIR	-21.3	0.2	0.7	3.6	-7.3	0.3	1.0	4.5	-5.3	0.7	3.4	13.1
FLIN	-13.1	0.4	1.3	2.8	-15.4	0.6	2.7	3.8	8.5	1.5	8.3	10.6
GODE	2.2	0.3	1.2	2.3	-15.9	0.6	1.9	4.1	11.8	1.4	1.4	10.1
MDO1	-8.9	0.3	0.9	2.2	-11.5	0.7	2.8	5.0	5.8	1.6	12.0	11.1
MIA1	0.0	0.3	1.9	4.2	-10.7	0.5	2.9	6.7	-3.6	1.0	11.6	13.4
NLIB	-5.2	0.2	0.7	2.6	-14.7	0.3	1.2	4.7	2.4	0.8	2.9	10.7
PIE1	-10.0	0.1	0.5	2.6	-10.2	0.2	0.9	5.7	3.4	0.4	2.4	10.8
RCM5	1.5	0.3	1.3	4.2	-6.6	0.5	2.6	7.2	-4.8	0.9	9.1	13.7
STJO	7.8	0.2	1.0	4.5	-15.6	0.2	0.9	5.9	-1.5	0.4	3.4	10.6
TMGO	-10.2	0.3	1.3	2.4	-14.8	0.7	1.8	4.9	3.6	1.5	4.7	10.3
WES2	8.7	0.5	1.9	4.0	-21.9	0.6	2.1	5.5	11.5	1.2	3.1	10.5
WHIT	-16.3	0.6	2.8	4.1	-11.1	0.7	2.3	4.6	-2.3	1.5	8.0	9.8
YELL	-12.3	0.2	1.0	3.7	-13.9	0.2	1.0	4.8	-2.6	0.5	3.2	11.7

Note:  $\sigma^w$  is estimated from a pure white noise model, while  $\sigma^{wf}$  is estimated from a white plus flicker noise model.

### 4.3.1 Overall Rigidity of North American Plate Interior

When we fit the 20 sites with one rigid plate model, we found WES2 had extremely large residual velocity ( $9.1 \pm 2.0 \text{mm/yr}$ , N $51^\circ\text{W}$ ) compared to other sites. Based on the site log of WES2, the antenna had been changed several times during the period of our data, usually due to failures caused by lightning [Niell, 1998]. In fact, this site has had antenna changes more frequently than any other site (Table 4.1). Offset errors may have been introduced in one or more replacements of the antenna, making the velocity estimation unreliable given our relatively short time series (Figure 4.2). In following discussion, WES2 is omitted, leaving 19 sites.

#### *Estimation Scheme 0*

The test of overall rigidity can be done with  $\chi^2$  as defined in equation (4.11) to determine whether a plate deforms significantly. Site velocities should be zero within error after subtraction of a reference plate motion that describes the average site motion given perfect data and a rigid plate. The best fitting Euler vectors were estimated from 19 sites with both error schemes. With the error scheme of a pure white noise model, the fitting solution has a chi-square of 1010.8 with degree of freedom equal to 35 (Table 4.3). If the error model is correct and the North America is rigid (i.e. the residuals are all explained by observational errors), the possibility of obtaining such  $\chi^2$  value or higher is less than 0.01%, which suggests that the North America continent has less than 0.01% chance to be rigid; alternately the errors are underestimated. The best fitting Euler vector, derived from

19 sites and the white noise model, gives the predicted velocities and residuals (observed minus predicted velocities) in Table 4.4 and Figure 4.3.

**Table 4.3a Description of Estimation Schemes**

Estimation scheme	0	1	2	3	4	5	6
White plus flicker noise	No	Yes	Yes	Yes	Yes	Yes	Yes
FLIN used	Yes	Yes	No	Yes	No	Yes	No
4 tectonic sites <sup>1</sup> used	Yes	Yes	Yes	No	No	Yes	Yes
PGR corrected <sup>2</sup>	No	No	No	No	No	Yes	No
Only longer than 3 years	No	No	No	No	No	No	Yes

1. Four sites near active tectonic regions are DRAO, FAIR, PIE1 and WHIT.
2. PGR corrections on ALGO, BRMU, DRAO, FAIR, GODE, MDO1, NLIB, PIE1, RCM5, STJO, WHIT and YELL, for which we have data.

**Table 4.3b Euler Vectors for North America Relative to ITRF96**

Estimation Scheme	0	1	2	3	4	5	6
Latitude (°)	1.0	0.4	0.2	-0.3	-1.7	0.0	-0.1
Longitude (°)	-79.8	-79.2	-79.5	-79.8	-79.2	-79.0	-79.0
Rotation rate (°/my)	0.200	0.200	0.199	0.199	0.193	0.199	0.197
Max error (°) <sup>7</sup>	1.8	1.8	1.6	2.8	2.6	1.8	2.5
Min error (°) <sup>7</sup>	0.6	0.7	0.6	0.9	0.8	0.7	1.1
Azimuth (°)	-5.0	-10.8	-10.4	-4.8	-3.7	-14.2	-9.9
Rate error (°/my) <sup>7</sup>	0.006	0.005	0.005	0.009	0.008	0.004	0.007
$\chi^2$	1010.8	44.7	32.1	39.8	27.1	49.1	20.1
Degree of Freedom	35	35	33	27	25	35	11
Reduced $\chi^2$	28.88	1.28	0.97	1.48	1.09	1.40	1.82
Mean residual (mm/yr)	1.9	1.9	1.7	2.0	1.8	1.9	1.3

0. Based on GPS data for ALGO, ARP3, BRMU, CHA1, CHUR, DET1, DRAO, FAIR, FLIN, GODE, MDO1, MIA1, NLIB, PIE1, RCM5, STJO, TMGO, WHIT and YELL.
1. Based on GPS data for ALGO, ARP3, BRMU, CHA1, CHUR, DET1, DRAO, FAIR, FLIN, GODE, MDO1, MIA1, NLIB, PIE1, RCM5, STJO, TMGO, WHIT and YELL.
2. Based on GPS data for ALGO, ARP3, BRMU, CHA1, CHUR, DET1, DRAO, FAIR, GODE, MDO1, MIA1, NLIB, PIE1, RCM5, STJO, TMGO, WHIT and YELL.
3. Based on GPS data for ALGO, ARP3, BRMU, CHA1, CHUR, DET1, FLIN, GODE, MDO1, MIA1, NLIB, RCM5, STJO, TMGO and YELL.
4. Based on GPS data for ALGO, ARP3, BRMU, CHA1, CHUR, DET1, GODE, MDO1, MIA1, NLIB, RCM5, STJO, TMGO and YELL.
5. Based on GPS data for ALGO, ARP3, BRMU, CHA1, CHUR, DET1, DRAO, FAIR, FLIN, GODE, MDO1, MIA1, NLIB, PIE1, RCM5, STJO, TMGO, WHIT and YELL (with PGR corrections).
6. Based on GPS data for ALGO, BRMU, FAIR, NLIB, PIE1, STJO and YELL.
7. One standard error; for 95% confidence error ellipse, multiply axes by 2.45.

**Table 4.4 Predicted and Residual Site Velocities from Estimation Scheme 0<sup>2</sup> (mm/yr)**

Site ID	Predicted			Residual		
	North	East	North	East	Magnitude	Azimuth
ALGO	0.7	-15.7	-0.8	-0.0	0.8	-178.5
ARP3	-6.6	-9.5	-1.3	-1.7	2.1	-128.0
BRMU	5.8	-11.1	1.6	-0.5	1.6	-16.4
CHA1	-0.0	-11.7	0.5	1.6	1.6	72.1
CHUR	-5.5	-18.2	-0.2	1.2	1.2	100.1
DET1	-1.3	-14.6	-0.6	3.2	3.3	101.0
DRAO	-14.3	-12.7	-0.5	1.0	1.1	118.8
FAIR	-20.6	-7.5	-0.7	0.2	0.7	165.6
FLIN	-8.4	-16.6	-4.7	1.2	4.8	166.0
GODE	1.2	-13.7	1.0	-2.2	2.5	-65.3
MDO1	-9.1	-10.0	0.2	-1.5	1.5	-81.0
MIA1	-0.1	-9.3	0.1	-1.4	1.4	-84.7
NLIB	-4.5	-14.2	-0.7	-0.5	0.8	-142.1
PIE1	-10.6	-10.7	0.6	0.5	0.8	40.6
RCM5	-0.2	-9.2	1.7	2.6	3.1	56.9
STJO	10.2	-14.3	-2.4	-1.3	2.7	-151.7
TMGO	-9.6	-12.6	-0.6	-2.2	2.3	-106.3
WHIT	-18.3	-10.8	2.0	-0.3	2.0	-7.9
YELL	-12.7	-16.0	0.4	2.1	2.2	80.5

1. Relative to ITRF-96.

2. Based on all 19 sites and the white noise model. Estimation scheme is detailed in Table 4.3.

3. Magnitude is  $\sqrt{(R_n^2 + R_e^2)}$  where  $R_n$ ,  $R_e$  are the north or east Residuals (Observed - Predicted).

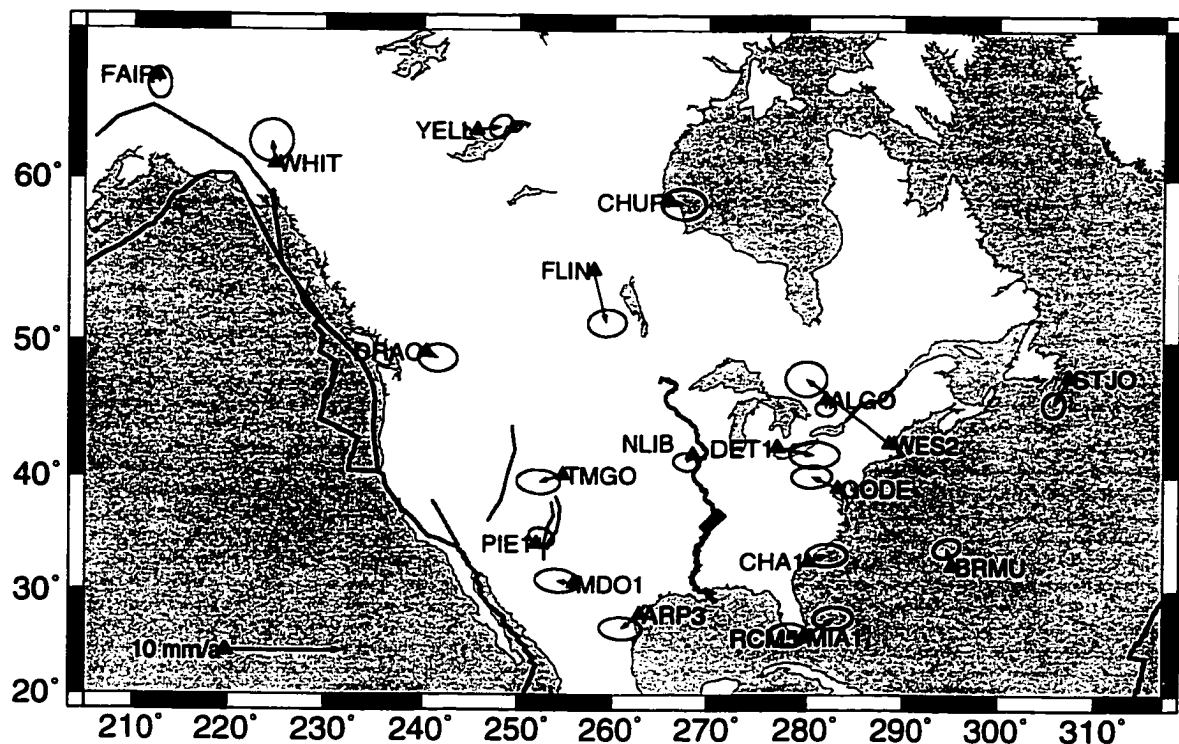


Figure 4.3 Velocity residuals and 95% confidence error ellipses from estimation scheme 0. WES2 is shown for comparison only.

But the errors are obviously underestimated, even though they are scaled with  $\sqrt{\chi^2}$  in linear regression. This can be proved simply with a data decimation experiment [Ryan *et al.*, 1993], in which a time series is divided into a pair of disjoint sets based on some criteria, which is usually a time interval. Site velocity and its variance are estimated from each data set. We can compare the velocity differences normalized with the root of sum of the velocity variances for all pairs. The expectation of such normalized difference is equal to one, if velocity errors are estimated correctly. When the two sets are divided by year, normalized differences range from 0.2 to 7.8 with a mean of 2.3.

*Estimation Schemes 1 and 2*

However, when we use the white plus flicker noise model, the rigid plate hypothesis explains the GPS velocity field with a chi-square of 44.7 with degree of freedom equal 35 (Table 4.3). It indicates that there is 1.5% chance that the North America plate is rigid. The residual velocity of all sites except FLIN is zero within 95% confidence error ellipses (Figure 4.4, Table 4.5). By looking at position time series of FLIN (Figure 4.2), we see significant velocity change in the north component after April 10, 1997. If only data between April 10, 1997 and December 27, 1997 are used, the velocity estimates in ITRF96 are -6.5 and -17.3 mm/yr for north and east components, respectively. The residual velocity is reduced to  $2.23 \pm 1.9$  mm/yr (-35.7°). Perhaps there was some systematic change around April 10, 1997 or long term variation which cannot be detected by our short time series. This suggests that both velocity and error estimates can be biased if the time series is relatively short. If FLIN is removed from the estimation of plate motion, the overall chi-square is reduced to 32.1, with degree of freedom equal to 33, which indicates that the North America plate has a 46% chance of being rigid. The velocity residuals at other sites change by less than 0.2 mm/yr by removing FLIN (Table 4.5, Table 4.6). In the following discussions, we will use the white plus flicker noise model and report results with and without site FLIN.

**Table 4.5 Predicted and Residual Site Velocities from Estimation Scheme 1 (mm/yr)**

Site ID	Predicted		Residual			
	North	East	North	East	Magnitude	Azimuth
ALGO	0.4	-15.8	-0.5	0.1	0.5	171.8
ARP3	-6.8	-9.7	-1.1	-1.5	1.9	-125.3
BRMU	5.5	-11.3	1.9	-0.3	1.9	-8.8
CHA1	-0.3	-11.8	0.8	1.7	1.9	66.2
CHUR	-5.7	-18.2	0.0	1.2	1.2	89.9
DET1	-1.5	-14.7	-0.4	3.3	3.3	96.6
DRAO	-14.4	-12.7	-0.4	1.0	1.0	113.3
FAIR	-20.6	-7.3	-0.7	0.0	0.7	176.8
FLIN	-8.6	-16.6	-4.5	1.1	4.7	165.6
GODE	0.9	-13.8	1.3	-2.1	2.5	-58.7
MDO1	-9.3	-10.1	0.4	-1.4	1.5	-73.1
MIA1	-0.4	-9.4	0.4	-1.3	1.3	-73.2
NLIB	-4.8	-14.3	-0.4	-0.4	0.6	-134.9
PIE1	-10.7	-10.8	0.7	0.6	0.9	37.3
RCM5	-0.5	-9.4	2.0	2.8	3.4	54.9
STJO	9.9	-14.5	-2.1	-1.1	2.4	-152.4
TMGO	-9.8	-12.7	-0.5	-2.1	2.2	-102.0
WHIT	-18.4	-10.7	2.1	-0.4	2.1	-10.7
YELL	-12.8	-15.9	0.5	2.0	2.1	76.1

Similar to Table 4.4. Based on 19 sites and the white plus flicker noise model.

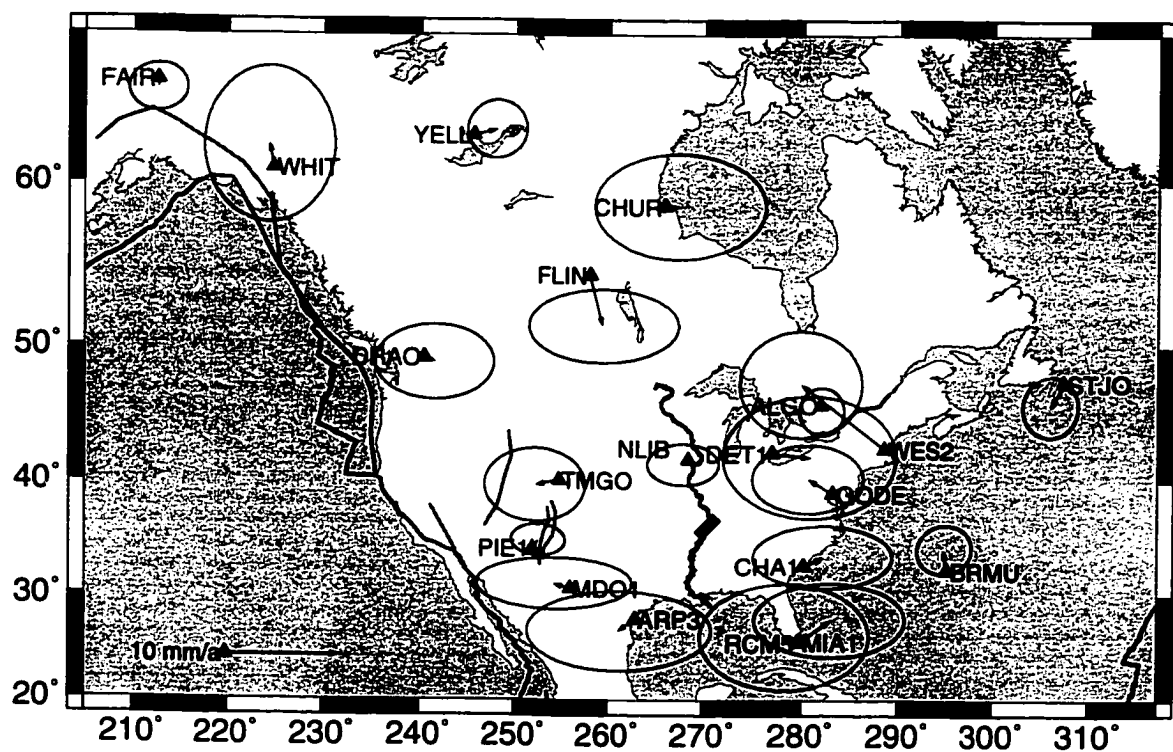


Figure 4.4 Velocity residuals and 95% confidence error ellipses from estimation scheme 1. WES2 is shown for comparison only. Major tectonic features are described in Figure 4.1.

**Table 4.6 Predicted and Residual Site Velocities from Estimation Scheme 2 (mm/yr)**

Site ID	Predicted		Residual			
	North	East	North	East	Magnitude	Azimuth
ALGO	0.6	-15.8	-0.6	0.1	0.7	175.0
ARP3	-6.7	-9.7	-1.2	-1.5	1.9	-130.0
BRMU	5.6	-11.3	1.8	-0.3	1.8	-9.2
CHA1	-0.1	-11.8	0.6	1.7	1.8	70.1
CHUR	-5.5	-18.2	-0.1	1.2	1.2	97.3
DET1	-1.4	-14.7	-0.5	3.3	3.4	98.9
DRAO	-14.2	-12.7	-0.6	1.0	1.2	120.0
FAIR	-20.4	-7.5	-0.9	0.1	0.9	170.3
GODE	1.0	-13.8	1.2	-2.1	2.4	-61.2
MDO1	-9.2	-10.2	0.3	-1.4	1.4	-79.0
MIA1	-0.2	-9.5	0.2	-1.2	1.2	-78.4
NLIB	-4.6	-14.3	-0.6	-0.4	0.7	-143.9
PIE1	-10.6	-10.8	0.6	0.6	0.8	47.1
RCM5	-0.3	-9.4	1.8	2.8	3.4	57.0
STJO	10.0	-14.4	-2.2	-1.1	2.5	-151.9
TMGO	-9.6	-12.7	-0.6	-2.1	2.2	-106.5
WHIT	-18.2	-10.8	1.9	-0.3	1.9	-9.2
YELL	-12.6	-16.0	0.3	2.1	2.1	80.8

Similar to Table 4.4. Based on 18 sites (FLIN removed).

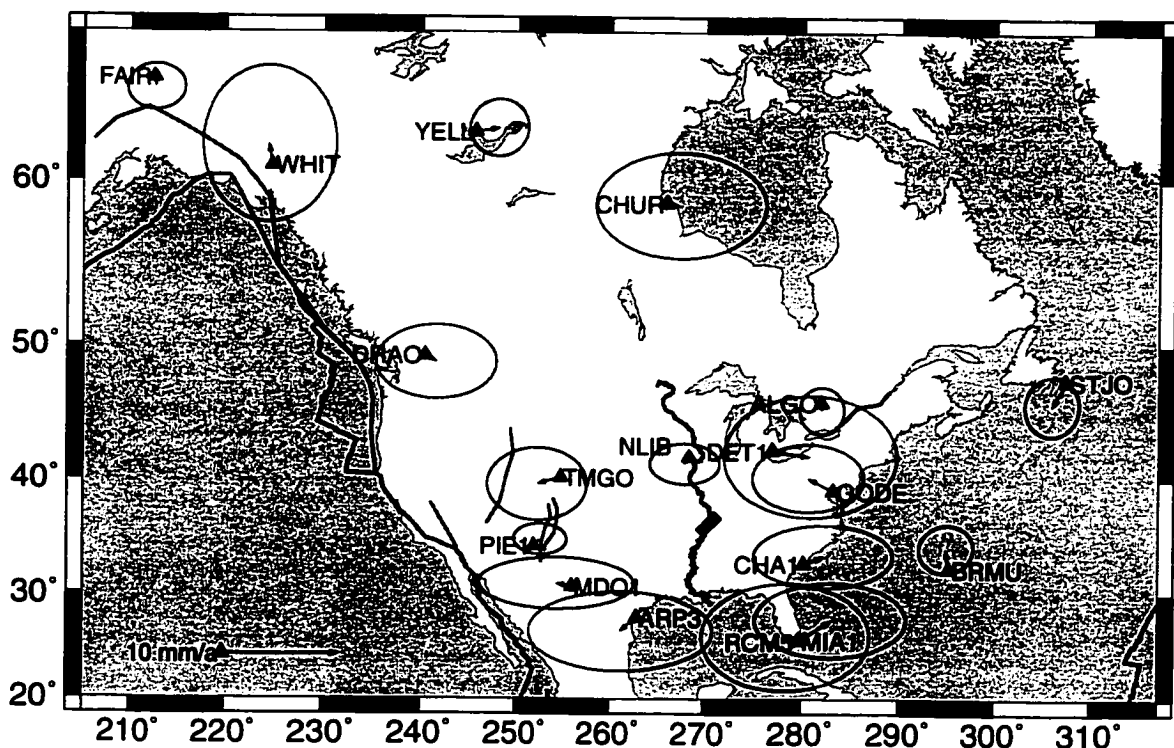


Figure 4.5 Velocity residuals and 95% confidence error ellipses from estimation scheme 2. Major tectonic features are described in Figure 4.1.

#### *Estimation Schemes 3 and 4*

Four sites (DRAO, FAIR, PIE1, and WHIT) are near active tectonic regions associated with the Pacific-North America plate boundary zone (Figure 4.1). For example, PIE1 is near the Rio Grande Rift, adjacent to the southwest boundary of the Basin and Range extensional province. FAIR is about 200 km from the Denali fault, near a zone of seismicity associated with northeast striking left-lateral faults [Page *et al.*, 1995]. However, none of these sites has a velocity that deviates significantly from the rigid plate model (Figure 4.4). Nevertheless, to be conservative, we also did a solution with these sites removed. This solution has a chi-square of 39.8 with a degree of freedom equal to

27. The chance of rigidity becomes 5%, which is little better than the solution with 19 sites. If the 4 sites and FLIN are all removed, the chance of rigidity is 36% (Table 4.3), which is a little smaller than the solution of 18 sites without FLIN. But such changes are trivial.

**Table 4.7 Predicted and Residual Site Velocities from Estimation Scheme 3 (mm/yr)**

Site ID	Predicted		Residual			
	North	East	North	East	Magnitude	Azimuth
ALGO	0.3	-15.9	-0.4	0.2	0.4	153.3
ARP3	-6.9	-9.8	-1.0	-1.4	1.7	-125.5
BRMU	5.4	-11.5	2.0	-0.1	2.0	-2.6
CHA1	-0.4	-12.0	0.9	1.9	2.1	64.2
CHUR	-5.8	-18.2	0.1	1.2	1.2	84.2
DET1	-1.7	-14.8	-0.2	3.4	3.5	94.0
FLIN	-8.7	-16.6	-4.4	1.2	4.6	165.0
GODE	0.8	-13.9	1.4	-2.0	2.5	-53.8
MDO1	-9.4	-10.2	0.5	-1.3	1.4	-67.5
MIA1	-0.5	-9.6	0.5	-1.1	1.2	-63.5
NLIB	-4.9	-14.4	-0.3	-0.3	0.5	-133.2
RCM5	-0.6	-9.6	2.1	3.0	3.7	54.7
STJO	9.7	-14.7	-1.9	-0.9	2.1	-153.9
TMGO	-9.8	-12.8	-0.4	-2.0	2.1	-100.2
YELL	-12.9	-15.9	0.6	2.0	2.1	74.2

Similar to Table 4.4. Based on 15 sites (remove four sites near active tectonic regions: DRAO, FAIR, PIE1 and WHIT).

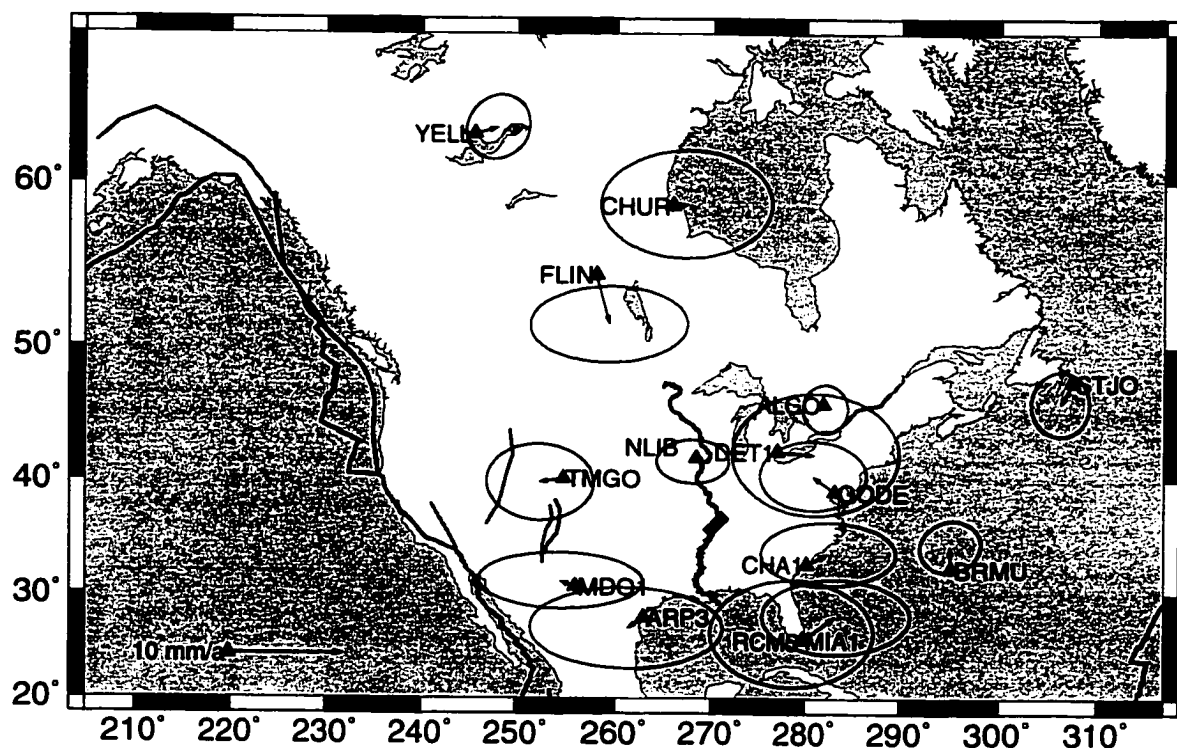


Figure 4.6 Velocity residuals and 95% confidence error ellipses from estimation scheme 3. Major tectonic features are described in Figure 4.1.

**Table 4.8 Predicted and Residual Site Velocities from Estimation Scheme 4 (mm/yr)**

Site ID	Predicted		Residual			
	North	East	North	East	Magnitude	Azimuth
ALGO	0.4	-15.8	-0.5	0.1	0.5	165.9
ARP3	-6.6	-10.1	-1.3	-1.1	1.7	-139.3
BRMU	5.4	-11.6	2.0	0.0	2.0	0.8
CHA1	-0.2	-12.1	0.7	2.0	2.1	69.9
CHUR	-5.5	-18.0	-0.2	1.0	1.1	100.3
DET1	-1.5	-14.8	-0.4	3.5	3.5	97.3
GODE	0.9	-14.0	1.3	-1.9	2.3	-56.0
MDO1	-9.0	-10.5	0.1	-1.0	1.1	-83.3
MIA1	-0.4	-9.9	0.4	-0.8	0.9	-67.0
NLIB	-4.6	-14.4	-0.6	-0.3	0.7	-153.9
RCMS	-0.4	-9.8	1.9	3.2	3.8	58.9
STJO	9.6	-14.6	-1.8	-1.0	2.1	-150.3
TMGO	-9.4	-12.9	-0.8	-1.9	2.1	-112.0
YELL	-12.4	-15.8	0.1	1.9	1.9	87.2

Similar to Table 4.4. Based on 15 sites (DRAO, FAIR, PIE1, WHIT and FLIN are removed).

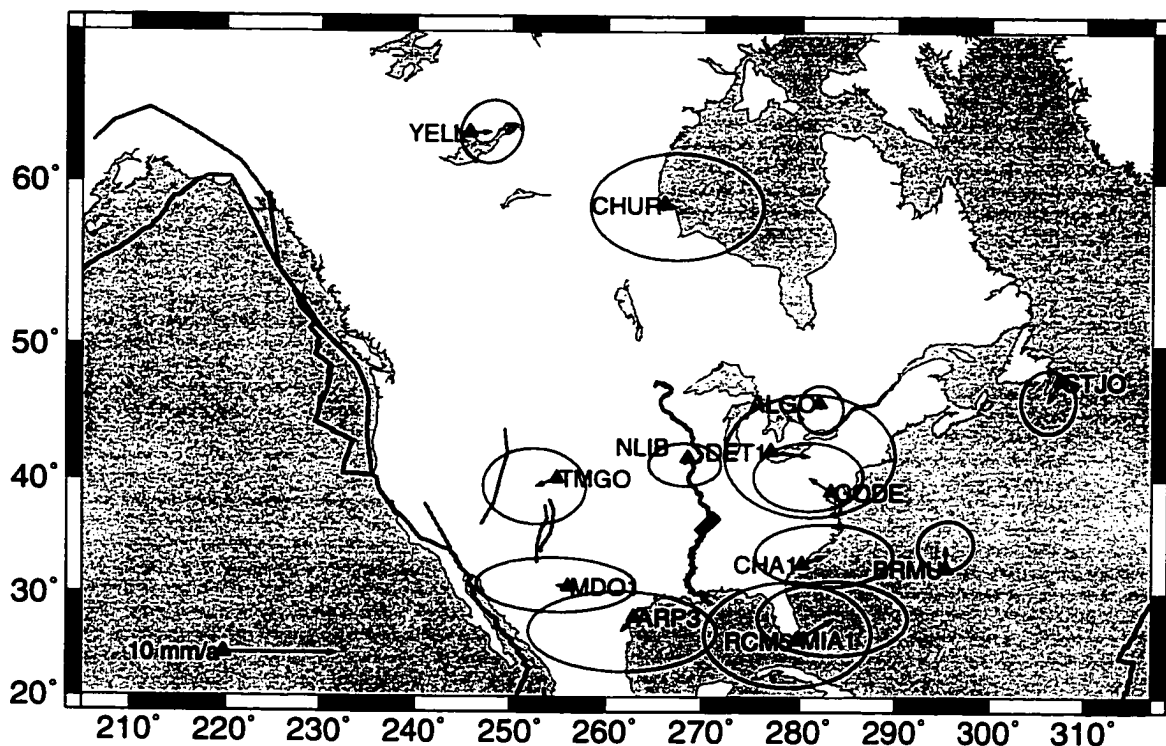


Figure 4.7 Velocity residuals and 95% confidence error ellipses from estimation scheme 4. Major tectonic features are described in Figure 4.1.

#### *Estimation Scheme 5*

The horizontal component of velocity due to postglacial rebound may perturb the measured GPS velocity field. Inspection of velocities predicted by the ICE-4G model [Peltier, 1995; McCarthy, 1996] suggests that horizontal velocities due to post glacial rebound are less than 1.0 mm/yr at sites for which we have PGR corrections (ALGO, BRMU, DRAO, FAIR, GODE, MDO1, NLIB, PIE1, RCM5, STJO, WHIT and YELL). Such corrections are relatively small compared to the residual velocity. We estimated the Euler vector again after the PGR corrections are applied to the observed site velocities, and found a slightly larger chi-square of 49.1 with degree of freedom equal to 35. The chi-

squares before and after PGR correction are not significantly different based on *F*-test, which indicates that our GPS results are not sensitive to PGR corrections. There is also no correlation of predicted PGR motions and GPS velocity residuals without PGR corrections (Figure 4.9).

**Table 4.9 Predicted and Residual Site Velocities from Estimation Scheme 5 (mm/yr)**

Site ID	Predicted		Residual			
	North	East	North	East	Magnitude	Azimuth
ALGO	0.4	-15.9	0.3	-0.1	0.3	-18.15
ARP3	-6.9	-9.8	-1.0	-1.4	1.7	-126.5
BRMU	5.5	-11.4	1.7	-0.2	1.8	-5.2
CHA1	-0.3	-11.9	0.8	1.8	2.0	66.0
CHUR	-5.8	-18.2	0.1	1.2	1.2	87.4
DET1	-1.6	-14.8	-0.3	3.4	3.4	95.4
DRAO	-14.4	-12.7	0.3	0.7	0.8	65.2
FAIR	-20.6	-7.3	-1.0	-0.1	1.0	-172.1
FLIN	-8.6	-16.6	-4.5	1.2	4.6	164.9
GODE	0.8	-13.9	1.4	-2.2	2.6	-57.3
MDO1	-9.4	-10.2	0.3	-1.4	1.4	-77.7
MIA1	-0.5	-9.6	0.5	-1.1	1.2	-68.3
NLIB	-4.8	-14.4	-0.3	-0.3	0.4	-135.0
PIE1	-10.8	-10.9	0.6	0.6	0.8	41.3
RCM5	-0.5	-9.5	1.9	2.9	3.5	56.8
STJO	9.8	-14.6	-2.1	-1.3	2.4	-148.6
TMGO	-9.8	-12.8	-0.4	-2.0	2.1	-101.4
WHIT	-18.4	-10.7	1.7	-0.4	1.8	-12.5
YELL	-12.8	-16.0	0.6	2.5	2.6	76.1

Similar to Table 4.4. Based on 19 sites with PGR corrections.

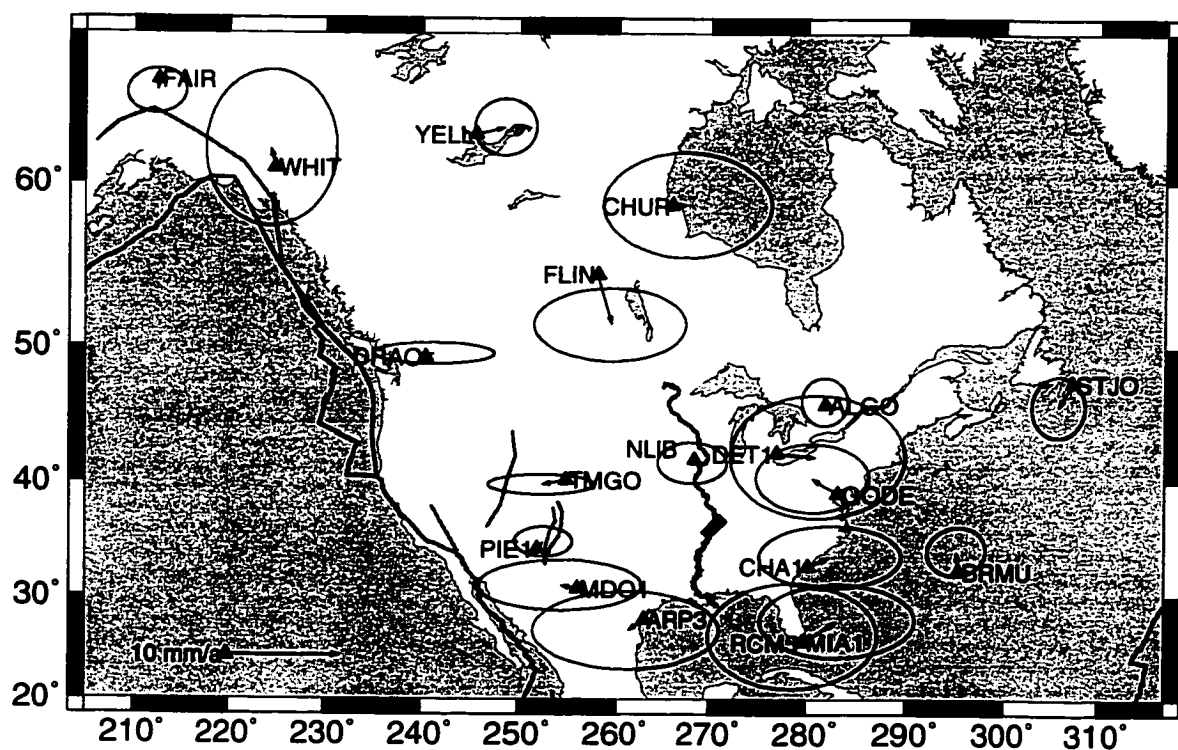
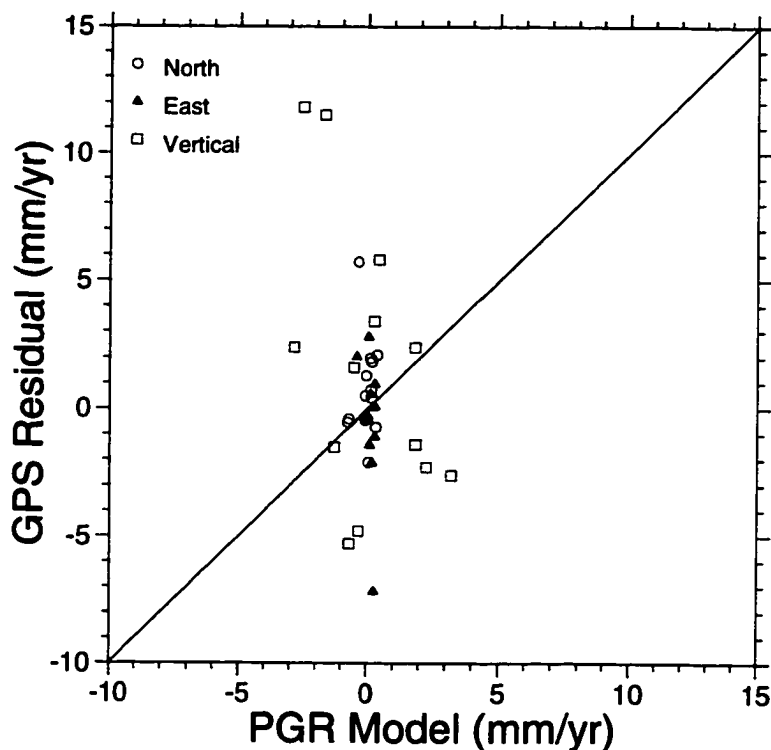


Figure 4.8 Velocity residuals and 95% confidence error ellipses from estimation scheme 5. Major tectonic features are described in Figure 4.1.



**Figure 4.9** Correlation between predicted PGR motions and GPS velocity residuals without PGR corrections, based on 12 sites for which we have PGR velocity predictions.

#### *Estimation Scheme 6*

As we discussed early, the estimates of site velocities and errors can be biased for short time series. Low velocity accuracy can also limit the ability to detect plate non-rigidity. We did a test using only sites which have data longer than three years (ALGO, BRMU, FAIR, NLIB, PIE1, STJO and YELL) (Table 4.10, Figure 4.10). Because of the better velocity accuracy, this solution suggests that there is only a 4.6% chance that the plate is perfectly rigid, which is much smaller than the possibility derived from 18 sites with FLIN removed.

**Table 4.10 Predicted and Residual Site Velocities from Estimation Scheme 6 (mm/yr)**

Site ID	Predicted			Residual		
	North	East	North	East	Magnitude	Azimuth
ALGO	0.4	-15.7	-0.5	0.0	0.5	178.9
BRMU	5.4	-11.3	2.0	-0.3	2.0	-7.4
FAIR	-20.3	-7.3	-1.0	-0.0	1.0	-178.6
NLIB	-4.8	-14.2	-0.4	-0.5	0.7	-132.1
PIE1	-10.7	-10.8	0.7	0.6	0.9	41.1
STJO	9.7	-14.5	-1.9	-1.1	2.2	-149.3
YELL	-12.7	-15.8	0.4	1.9	1.9	78.4

Similar to Table 4.4. Based on 7 sites which have data longer than 3 years.

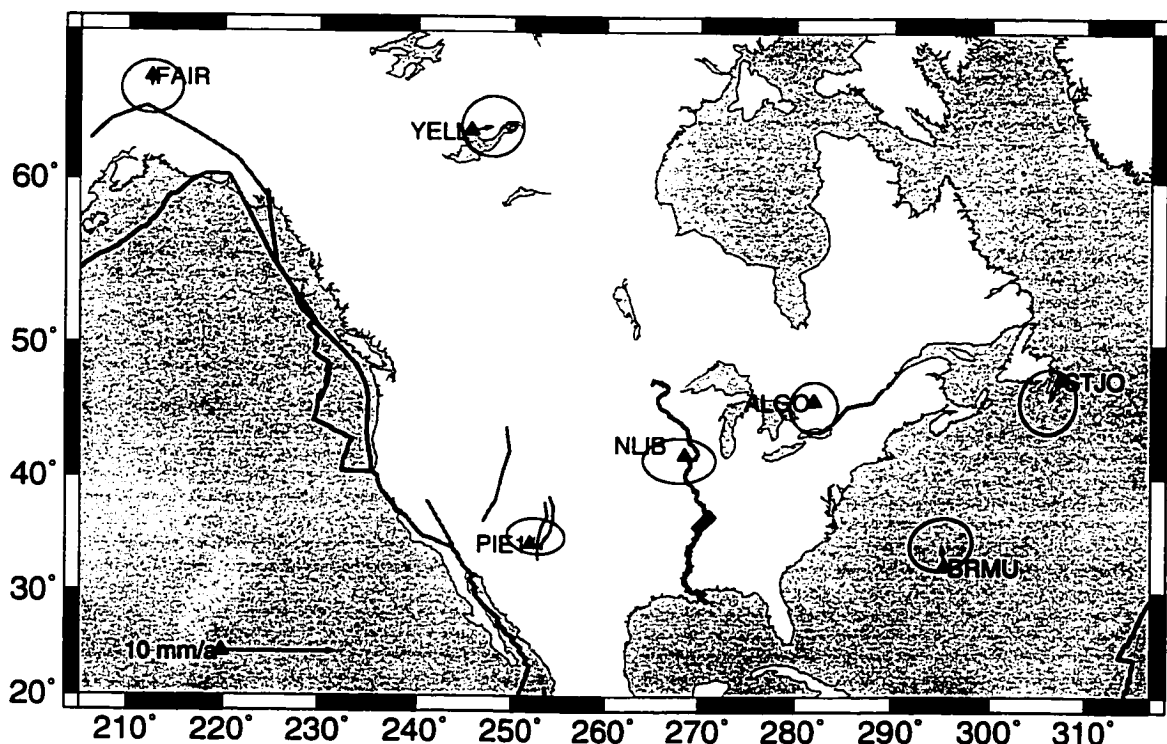


Figure 4.10 Velocity residuals and 95% confidence error ellipses from estimation scheme 6. Major tectonic features are described in Figure 4.1.

Both the pole positions and rotation rates of these plate motion models, estimated from different noise models and site sets, show no significant difference within one standard error (Table 4.3, Figure 4.11), because North America plate motion is well defined by the large number of sites, and the velocity of these sites agrees well with a rigid plate model. When the 4 sites and FLIN are all removed, the resultant Euler pole lies a little far from others, but its 39% error ellipse (one standard error) still overlaps with other error ellipses (Figure 4.11).

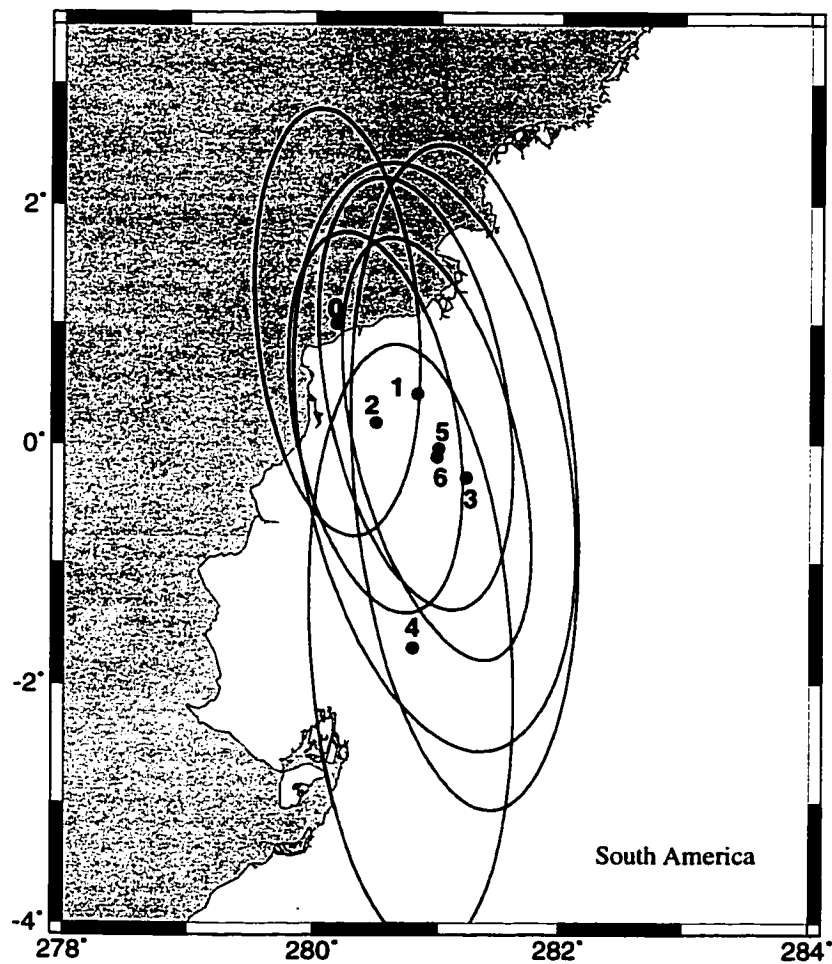


Figure 4.11 Euler pole positions and 39% error ellipses (one standard error) derived from different noise models and site sets. Estimation schemes are described in Tables 4.3.

The average magnitude of residual velocities based on all 19 sites is equal to 1.9 mm/yr (Table 4.5). If we only use sites which have data longer than three years (Table 4.10), the average is 1.3 mm/yr, which is the same result reported by *Dixon et al.* [1996] based on shorter time series. The most important implication of this result is that the interior of the North American plate is rigid, probably to the level of the maximum velocity residual derived from the 7 sites which have data longer than 3 years, and perhaps better because residual magnitudes are positively biased by observation errors [*Argus and Gordon*, 1996]. The agreement between the observed GPS velocities and a rigid plate model is comparable to results from earlier studies fitting velocities from Satellite Laser Ranging and Very Long Baseline Interferometry to rigid plate models [*Robbins et al.*, 1993; *Robaudo and Harrison*, 1993; *Argus and Gordon*, 1996].

#### 4.3.2 Predicted Relative Motion at New Madrid Seismic Zone

Differential motion between eastern and western North America is a possible explanation for New Madrid seismicity, consistent with hypotheses involving plate scale compressive stresses [*Zoback et al.*, 1989], reactivation of an ancient weak zone near New Madrid [*Hildebrand et al.*, 1982], and strain accumulation and subsequent release in earthquakes [*Hamilton and Zoback*, 1982]. On the other hand, one can also imagine local sources of stress leading to motion not manifested on a continental scale, undetected by our continental network. The pattern of seismicity at New Madrid delineates two NE-striking vertical faults linked by a short NW-striking fault [e.g., *Himes et al.*, 1988]. Focal mechanisms [*Hermann*, 1979], geology [*Russ*, 1982] and topography [*Gomberg and Ellis*,

1994] suggest two NE-striking right lateral faults connected by a NW-striking thrust or reverse fault, implying NE motion of the western block relative to the eastern block. Local geodetic data suggest strain accumulation here [Liu *et al.*, 1992; Weber *et al.*, 1996]. To investigate whether this motion occurs on a continental scale, and whether current space geodetic data can resolve it, we split stable North America into two blocks, northwest and southeast, separated by a diffuse zone of intraplate seismicity that runs through the St. Lawrence River Valley (Figure 4.1) southwest towards New Madrid, and continuing southwest through Texas [Goter *et al.*, 1992]. We solved for separate Euler vectors (Table 4.11, Figure 4.12), and predicted relative motion between the two continental blocks at New Madrid.

**Table 4.11 Euler Vectors for Eastern and Western North America Relative to ITRF96**

Estimation scheme <sup>2</sup>	E-1	E-5	W-1	W-2	W-3	W-4	W-5
Latitude (deg)	-1.9	-2.1	-0.1	0.1	-6.0	-8.4	-0.5
Longitude (deg)	-80.7	-80.5	-78.2	-78.8	-75.7	-76.2	-78.2
Rotation rate (deg/my)	0.198	0.199	0.196	0.196	0.182	0.176	0.196
Max error (deg) <sup>1</sup>	4.8	4.8	2.8	2.0	5.9	3.0	2.8
Min error (deg) <sup>1</sup>	1.4	1.4	0.9	0.7	1.3	0.7	0.8
Azimuth (deg)	9.6	9.3	-18.1	-17.9	-14.2	-13.2	-18.4
Rate error (deg/my) <sup>1</sup>	0.018	0.018	0.007	0.005	0.012	0.006	0.006
$\chi^2$	16.7	16.8	23.1	11.4	14.5	2.7	27.6
Degree of Freedom	11	11	19	17	11	9	19
Reduced $\chi^2$	1.52	1.52	1.22	0.67	1.32	0.30	1.45

1. One standard error; for 95% confidence error ellipse, multiply axes by 2.45.

2. Following the estimation schemes described in Table 4.3, the sites are separated into two blocks (E indicates the southeast block. W indicates the northwest block.). Sites used in each solution are:

E-1 based on GPS data for APR3, BRMU, CHA1, GODE, MIA1, RCM5 and STJO. Southeast block has the same site set for the estimation schemes 1, 2, 3 and 4.

E-5 based on the same site set as E-1 with PGR correction on BRMU, GODE, RCM5 and STJO.

W-1 based on GPS data for ALGO, CHUR, DRAO, FAIR, FLIN, MDO1, NLIB, PIE1, TMGO, WHIT and YELL.

W-2 based on GPS data for ALGO, CHUR, DRAO, FAIR, MDO1, NLIB, PIE1, TMGO, WHIT and YELL.

W-3 based on GPS data for ALGO, CHUR, FLIN, MDO1, NLIB, TMGO and YELL.

W-4 based on GPS data for ALGO, CHUR, MDO1, NLIB, TMGO and YELL.

W-5 based on the same site set as W-1 with PGR correction on ALGO, DRAO, FAIR, MDO1, NLIB, PIE1, WHIT and YELL.

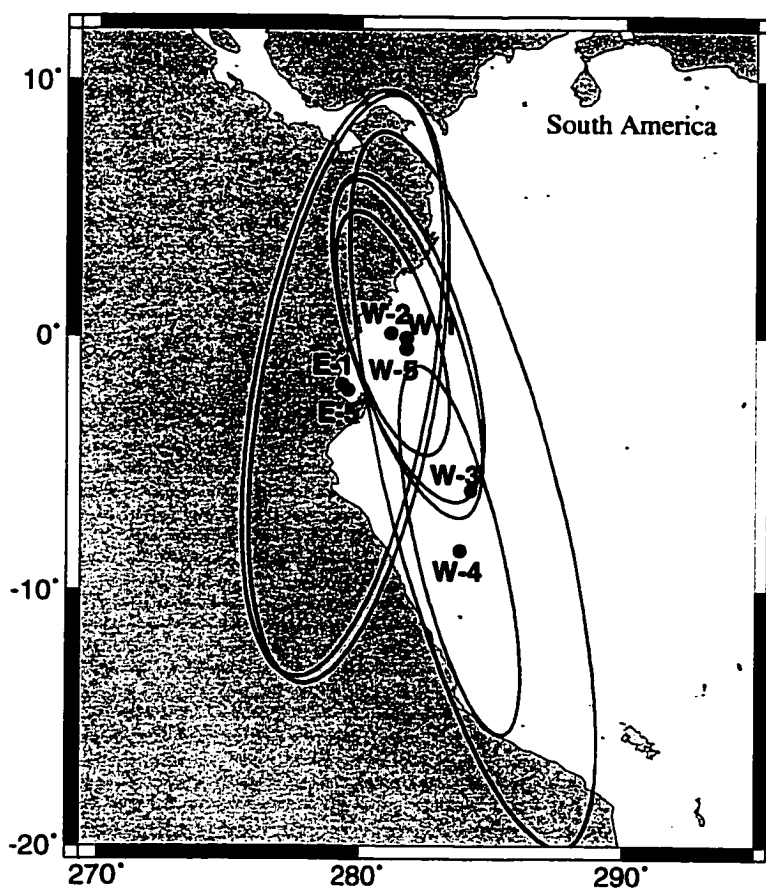


Figure 4.12 Euler pole positions and 95% error ellipses for eastern and western North America Relative to ITRF96. Estimation schemes are described in Table 4.11.

Following the previous section, we investigated the relative motion with five estimation schemes (Table 4.11). The PGR corrections make minor changes on Euler vectors for both eastern and western North America. The biggest difference appears when the FLIN and 4 sites near active zones are removed. But the Euler poles for the eastern and western blocks still overlap at the 95% confidence (Table 4.11, Figure 4.12). Although the variance is reduced in the two-plate model, an *F*-ratio test shows the

reduction is not significant, no more than expected from adding more degrees of freedom. Solving for relative motion at New Madrid ( $36.5^{\circ}\text{N}$ ,  $89.5^{\circ}\text{W}$ ) gives motion of the west block relative to the east block at  $1.2 \pm 0.9$  mm/yr ( $\text{N}41^{\circ}\text{W}$ ) when 11 western sites are used, or at  $1.1 \pm 0.8$  mm/yr ( $\text{N}2.4^{\circ}\text{W}$ ) when five sites (PIE1, FAIR, DRAO, WHIT and FLIN) are removed from the estimation. In all five cases, the relative motion is indistinguishable from zero at 95% confidence, and different in direction from the seismological and geological estimates cited above. The 95% confidence ellipse around the velocity estimate allows less than 2.0 mm/yr of NE motion of the west block relative to the east block (Figure 4.13). Together with the *F*-ratio test and overlapping error ellipses, this suggests that the small misfit of GPS velocities to the single rigid plate model is not due to differential motion at New Madrid.

Table 4.12 Predicted Relative Velocity at New Madrid Seismic Zone (West relative to East)

Estimation scheme <sup>1</sup>	Rate (mm/yr)	Azimuth <sup>2</sup> (degree)
1. All 19 sites	$1.2 \pm 0.9$	$-41 \pm 40^{\circ}$
2. FLIN omitted	$1.1 \pm 0.9$	$-51 \pm 42^{\circ}$
3. Omit 4 active tectonic sites	$1.4 \pm 0.9$	$-8.9 \pm 42^{\circ}$
4. Omit FLIN & 4 sites	$1.1 \pm 0.8$	$-2.4 \pm 42^{\circ}$
5. PGR corrected	$1.1 \pm 0.9$	$-45 \pm 44^{\circ}$

1. Estimation schemes are detailed in Table 4.11 and Table 4.3.

2. Clockwise from North.

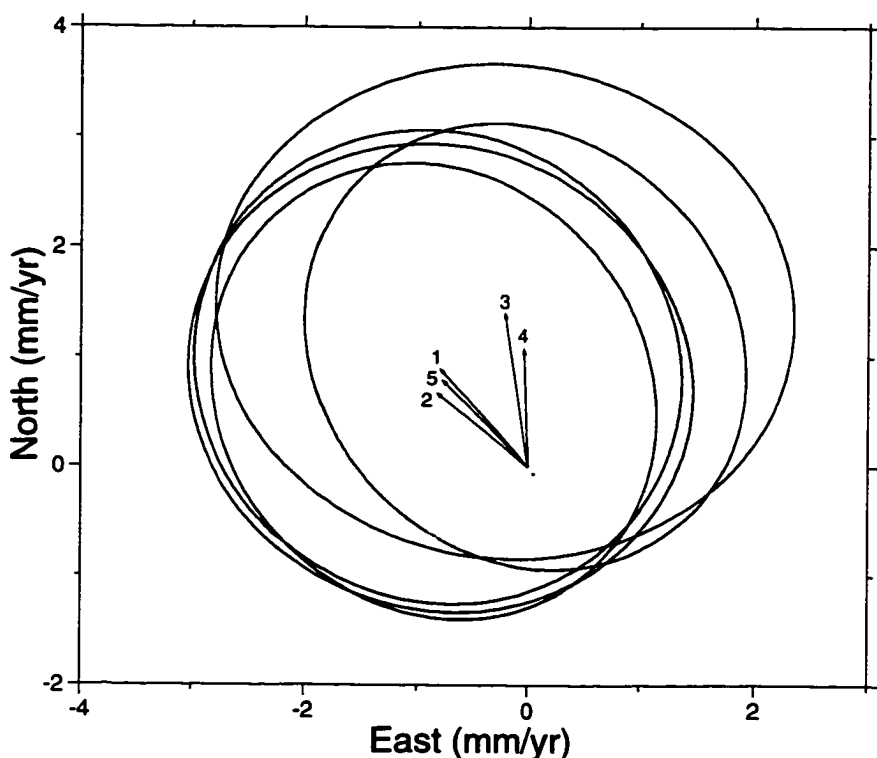


Figure 4.13 Predicted relative velocity and 95% error ellipses at New Madrid Seismic Zone (West relative to East). Numbers indicate the estimation schemes detailed in Table 4.11 and Table 4.3.

Our results have implications for interpretation of local geodetic data. *Liu et al.* [1992] predict 5-7 mm/yr of strike-slip motion across New Madrid. Our data show no evidence for significant motion at these rates manifested on a continental scale.

#### 4.4 Conclusions

Since the velocity residuals do not correlate in any obvious way with post-glacial rebound, Pacific-North America boundary zone tectonics, or differential motion between eastern and western North America at New Madrid, and since the magnitude of the

residuals is smaller than 95% velocity errors for all but two sites (WES2, FLIN; Figure 4.4), we conclude that the single rigid plate model adequately explains the data as it exists today. There may be some chance that small relative motions exist at some locations, but such motions are not significant based on our GPS measurements. The misfits between observed velocities and the rigid plate model do not appear to reflect motion across the New Madrid seismic zone or postglacial rebound, and most likely reflect observational error. Thus, our estimate of the velocity residuals is an upper bound to plate rigidity. The plate is likely to be more rigid than implied by our residuals, and agreement between data and model is limited by observational error.

In the above analysis, all reduced chi-squares are in the range of 0.30 to 1.81, when rigid plate models are fitted to different sets of GPS sites with velocity errors based on the white and flicker noise model (Table 4.3, Table 4.11). The lower bound of plate rigidity is zero residual velocity, and all the velocity residuals are from observational errors. It is also unlikely that any GPS site set tested, deviates significantly from a rigid plate model. Deviation of the errors estimated with the white plus flicker noise model is within about -45% to +35% of unity, and is significantly better than the pure white noise model, which produces much lower values of reduced chi-squares.

## CHAPTER 5 Present-Day Motion across the East African Rift

### 5.1 Introduction

The East African Rift is the Earth's longest active continental rift, and likely played a critical role in human evolution. Although a century of study of rift topography, volcanism, faulting and seismicity documents active extension [e.g., *Gregory*, 1896; *Baker et al.*, 1971; *Shudofsky*, 1984], we still lack an accurate description of relative motion across the rift. Estimation of this motion [*McKenzie et al.*, 1970; *Chase*, 1978; *Le Pichon and Francheteau*, 1978; *Minster and Jordan*, 1978; *Joffe and Garfunkel*, 1987; *DeMets et al.*, 1990; *Jestin et al.*, 1994; *Chu*, 1995] has been challenging for a variety of reasons. The diffuse nature of the rift zone makes direct measurements difficult, while the limited magnetic anomaly data and short transform faults in the Red Sea and Gulf of Aden, which respectively constrain the rate and direction of Nubia-Arabia and Somalia-Arabia motion, make Euler vector estimation difficult. Finally, there is uncertainty in the location and even existence of the Nubia-Somalia-Antarctica triple junction. The rich global data set used for the Nuvel-1 plate motion model, for example, predicts 3 mm/yr of right-lateral motion across the rift, violating geologic constraints [*DeMets et al.*, 1990]. It has thus been unclear whether to regard Nubia and Somalia as distinct plates [*Stein and Gordon*, 1984] or to instead regard the East African Rift as the “failed arm” [*Burke and Dewey*, 1973] of the Afar triple junction, formed during the uplift and extension that created the Red Sea and Gulf of Aden spreading centers. In the latter scenario, the Rift is spreading

slowly (a few mm/yr or less) and may be dying out. One possibility is that the rift is a Precambrian lineament that is periodically reactivated, but is not currently extending at appreciable rates [McConnell, 1980].

## 5.2 Relative Motion Derived from Space Geodetic Measurements

The existence of a global network of semi-permanent space geodetic sites makes it possible to measure the velocities of major plates and crustal blocks with unprecedented accuracy. These data record plate motions over a few years, in contrast to earlier studies using rates of plate motions derived from magnetic anomalies which record plate motions averaged over millions of years. We combined velocity data from the Global Positioning System (GPS) [Dixon, 1991a], Doppler Orbitography and Radiopositioning Integrated Satellite System (DORIS) [Cazenave *et al.*, 1992], Very Long Baseline Interferometry (VLBI) [Ryan *et al.*, 1993], and Satellite Laser Ranging (SLR) [Smith *et al.*, 1990], in global reference frame ITRF-96 [Boucher, 1998]. GPS data were analyzed following Dixon *et al.* [1997a]. DORIS velocities and uncertainties were provided by Soudarin [1997]. VLBI and SLR velocities and uncertainties were taken from Boucher [1998] (Table 5.1).

**Table 5.1 Site Velocities (ITRF-96, mm/yr)**

Site	North	East	System
<i>Nubia</i>			
7501	$18.9 \pm 0.8$	$16.6 \pm 1.0$	VLBI, SLR
ARMA	$22.9 \pm 2.4$	$21.0 \pm 5.7$	DORIS
DAKA	$22.0 \pm 1.6$	$24.0 \pm 3.7$	DORIS
HART	$18.5 \pm 0.2$	$16.7 \pm 0.3$	GPS
HBKA	$15.6 \pm 1.3$	$14.5 \pm 2.7$	DORIS
HELA	$22.2 \pm 1.6$	$30.0 \pm 3.7$	DORIS
LIBA	$22.0 \pm 1.5$	$20.1 \pm 3.5$	DORIS
MAS1	$17.2 \pm 0.1$	$17.0 \pm 0.2$	GPS
TRIA	$25.9 \pm 1.3$	$14.5 \pm 2.5$	DORIS
<i>Somalia</i>			
MALI	$13.7 \pm 0.3$	$27.5 \pm 0.9$	GPS
REUA	$14.7 \pm 3.3$	$10.4 \pm 4.8$	DORIS
SEY1	$9.1 \pm 1.4$	$41.7 \pm 5.1$	GPS

We inverted the data treating Nubia and Somalia as separate rigid plates, found the best fit Euler vector for each plate in ITRF-96, subtracted the Euler vectors to determine the best fit relative Euler vector, and propagated covariance matrices to estimate errors. Our Euler vector and some previous estimates [*Joffe and Garfunkel*, 1987; *Jestin et al.*, 1994; *Chu.*, 1995] are listed in Table 5.2. Quoted errors for VLBI, SLR and DORIS data (Table 5.1) assume white noise (time-independent) behavior. For consistency, we used the same assumption for GPS data, which may underestimate total error [*Johnson and Agnew*, 1995] because the Least Square estimation is affected not directly by the formal data errors, but instead by the relative accuracy (weight). To compensate for the overall error underestimation, the covariance matrix of the estimated Euler vector was scaled by

the reduced chi-square value. We also inverted only the GPS data and obtained similar results ("GPS only"; Table 5.2), albeit with larger errors. The motion of the Nubian plate is well constrained by 9 space geodetic sites, while there are only three sites on the Somalia plate and these sites have relatively large residuals in fitting to a rigid plate model. In order to test how sensitive our estimated relative motion is to the velocity measurements at individual sites, we also derived solutions by omitting MALI or SEY1 ("no MALI" and "no SEY1" in Table 5.2). Table 5.3 shows the predicted motions across the rift (Somalia relative to Nubia) based on different relative Euler vector estimates. When SEY1 is omitted, the relative motions appear slower, but the differences are not significant. When MALI is omitted, the solution is significantly degraded, which may indicate that SEY1 has too few measurements, and DORIS data (REUA) usually have lower accuracy than other techniques. More measurements and geodetic sites are required on the Somalia plate to derive an accurate estimate of the relative motion.

For the remainder of this paper, we use the results from all data, noting that the DORIS data contribute significant information in spite of their larger formal errors. Predicted motions across the rift are shown in Figure 5.1 and are similar to predictions of a model for plate motions over the last 3 Ma [*Chu, 1995*].

**Table 5.2 Euler Vectors Describing Relative Motion Between Nubia and Somalia**

	Pole position		$\omega$ (°/my)	Error ellipse <sup>1</sup>			$\sigma_w$ (°/my)
	°N	°E		$\sigma_{\max}$ (°)	$\sigma_{\min}$ (°)	$\xi_{\max}$ (°)	
This study (All data)	-46.6	13.7	0.072	46	8	36	0.064
This study (GPS only)	-46.3	14.6	0.075	55	12	35	0.094
This study (no SEY1)	-51.9	3.7	0.060	72	11	45	0.122
This study (no MALI)	-17.6	53.5	0.810	4	2	7	0.358
Joffe & Garfunkel [1987]	-6.9	33.0	0.09				
Jestin et al. [1994]	-55.7	19.8	0.054				
Chu [1995]	-63.7	27.2	0.065				

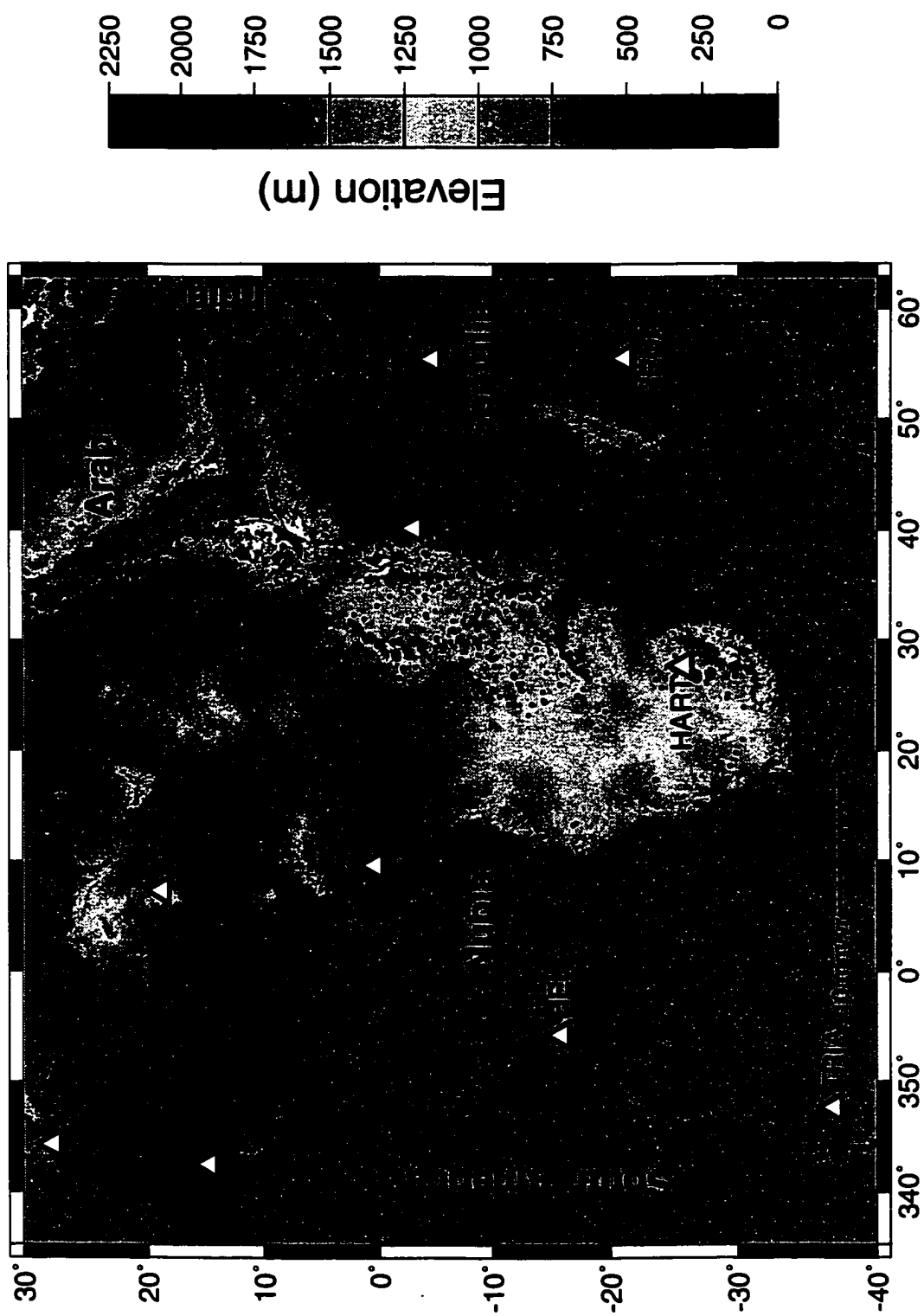
1.  $\xi_{\max}$  is orientation of long axis, degrees clockwise from north. Error ellipses are one standard error; for 95% confidence error ellipse, multiply by 2.45.

**Table 5.3 Predicted Motions across the Rift (Somalia Relative to Nubia) (mm/yr)**

Locations	$\phi=10^\circ, \lambda=45^\circ$	$\phi=0^\circ, \lambda=38^\circ$	$\phi=-10^\circ, \lambda=36^\circ$
All data	$7.1 \pm 3.2 (114 \pm 9^\circ)$	$6.2 \pm 2.0 (111 \pm 12^\circ)$	$5.3 \pm 2.3 (114 \pm 13^\circ)$
GPS only	$7.4 \pm 4.5 (113 \pm 14^\circ)$	$6.5 \pm 2.6 (111 \pm 17^\circ)$	$5.5 \pm 3.3 (113 \pm 18^\circ)$
No SEY1	$6.3 \pm 6.4 (115 \pm 13^\circ)$	$5.8 \pm 2.4 (114 \pm 19^\circ)$	$5.1 \pm 3.8 (116 \pm 15^\circ)$
No MALI	$43.3 \pm 17.7 (73 \pm 5^\circ)$	$35.4 \pm 15.1 (50 \pm 8^\circ)$	$28.1 \pm 12.9 (27 \pm 13^\circ)$

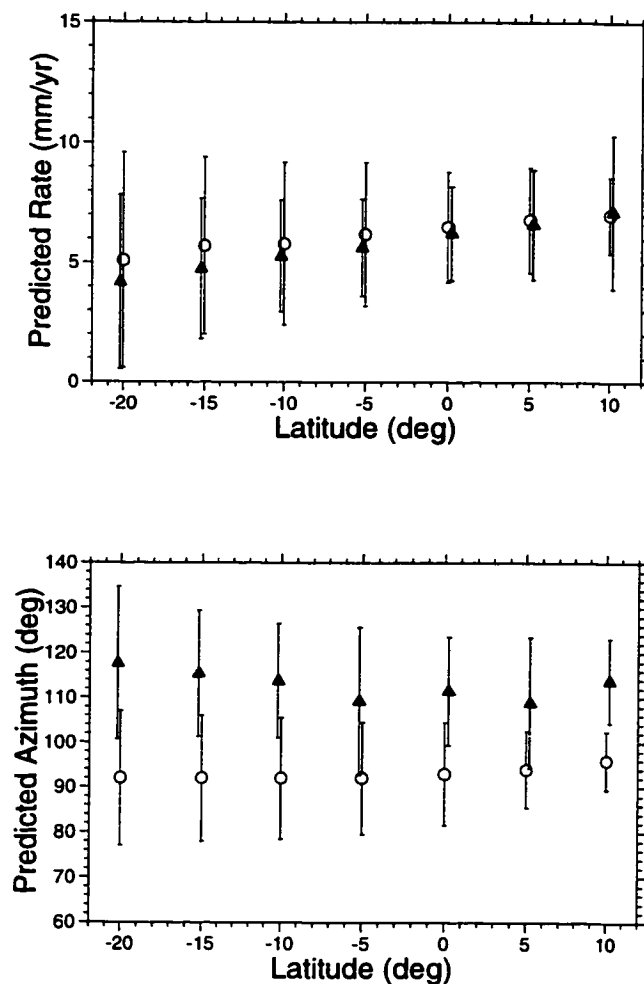
The numbers in parentheses are azimuth clockwise from north. Quoted errors are standard errors.

Figure 5.1 Topography, shallow seismicity (<50 km,  $M \geq 3.0$ , small dots) and lithospheric plates within and adjacent to Africa, and location of space geodetic sites used in this study. Predicted motion and error ellipse (one standard error) for Somalia relative to Nubia from space geodesy (all data) are shown at three locations along the East African Rift, outlined by high topography and diffuse seismicity. (next page)



### 5.3 Discussion and Conclusions

Establishing the overall extension direction in a geologically complex region like the East African Rift can be difficult. Earthquake tension axes reflect this complexity and exhibit a wide range of values, from NE-SW to E-W to NW-SE [Shudofsky, 1984]. Most geological studies predict extension directions between E-W [e.g., Morley, 1988] and NW-SE [e.g., Scott *et al.*, 1989; Rosendahl *et al.*, 1992]. Our Euler vector predicts an extension direction for most of the rift ( $N106^{\circ}$ - $112^{\circ}E$ ) intermediate between E-W and ESE-WNW, within the range of most previous studies. Our azimuth uncertainty depends on location, but for most of the rift is better than  $\pm 15^{\circ}$  (one standard error). Our predicted azimuth disagrees at one standard error with the direction between NW-SE and NNW-SSE proposed based on analysis of remote sensing imagery [Chorowicz *et al.*, 1994], but agrees with Chu's [1995] model, which is based on magnetic anomaly data (Figure 5.2).



**Figure 5.2** Comparison of extension rates and azimuths across the East African Rift, predicted from this study (present) and Chu's [1995] model (0-3 Ma). Error bars are one standard deviations.

Rate estimation has also proven difficult. A rate of 3-5 mm/yr across the north end of the Ethiopian Rift has been reported based on five years of geodimeter surveys [Mohr *et al.*, 1978]. A combination of geodimeter and GPS data yields an extension rate of  $1\pm 2$  mm/yr across part of the north Ethiopian rift, consistent with either very slow extension or episodic extension [Asfaw *et al.*, 1992]. Because the extension zone is wide and extension

on any individual portion may be episodic, local surveys may not capture the total extension. Our Euler vector predicts about 7 mm/yr of extension in the northern Ethiopian rift, considerably faster than the local estimates, perhaps reflecting this near versus far field effect. Our estimate agrees well with the most recent plate motion model [Chu, 1995] which is also based on data that records the full extension (Figure 5.2).

Our results have important implications for rifting history. Geologic data indicating only a few tens of km of extension across the rift, coupled with age estimates suggesting that rifting began in late Oligocene or early Miocene time, are generally interpreted as indicating relatively slow extension over this interval. The estimated 35-40 km of total extension in northern Kenya since rift initiation at 28-34 Ma [Hendrie *et al.*, 1994] predicts an average rate of 1.0-1.4 mm/yr. Similarly, an estimated maximum extension of 25 km in southern Ethiopia since 20 Ma [Ebinger *et al.*, 1993] implies an average extension rate no higher than 1.25 mm/yr. However, the extension rate is unlikely to have been constant over these long periods. Comparison of our results to those for different time periods suggests that extension has been accelerating since about 5-6 Ma (Figure 5.3). This acceleration may reflect a large scale change in plate motions. At about 6 Ma, spreading slowed on the southern mid-Atlantic Ridge, the western boundary of Nubia [Brozena, 1986], and the absolute motion of the African plate changed [Pollitz, 1991].

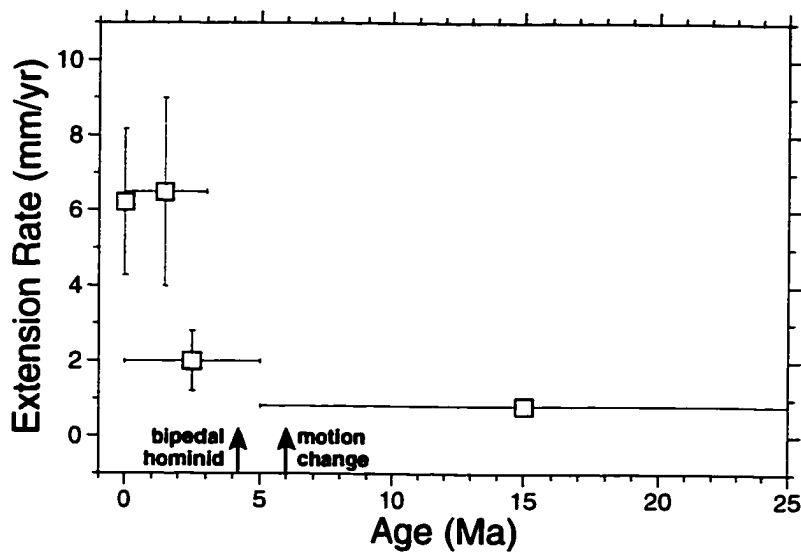


**Figure 5.3** Extension rate across the East African Rift near the equator as a function of time. Data from Hendrie *et al.* [1994] (5-25 Ma; 0-5 Ma), Chu [1995] (0-3 Ma), and this study (present day; all data). Vertical bars represent one standard error for rate estimate, horizontal bars represent averaging period. Vertical arrows show (right) time of change in absolute motion of African plate (6 Ma) [Pollitz, 1991] and (left) age of earliest known bipedal hominid (4.2 Ma) [Leakey *et al.*, 1995].

This tectonic history has implications for conditions within the East African Rift during a critical period for hominid evolution (Figure 5.3). The earliest known record of bipedal hominids is dated at 4.2 Ma within the Rift [Leakey *et al.*, 1995], implying that this characteristic developed prior to 4.2 Ma, probably in or near the rift. The first documented use of tools is nearly 2 million years later, at 2.5 Ma [Semaw *et al.*, 1997], implying evolutionary advantages to upright posture beyond tool use. Darwin [1871] speculated that bipeds originated due to a "change in the surrounding conditions". Although climate change, such as the greater variability after 2.8 Ma associated with global cooling and northern hemisphere glaciation [deMenocal, 1995], is considered an important factor in hominid evolution [Brain, 1981; Vrba, 1988], global climate change is

probably less important for the origin of bipedalism prior to 4.2 Ma, because global climate was relatively stable around this time [Kennett, 1995]. Topographic relief and volcanic activity probably increased as the rift extension rate increased, significantly impacting local rift environments, including microclimates (e.g., rain shadows). While the temporal correlation of accelerated rifting and bipedalism may be coincidental, it also is possible that there is direct cause and effect: bipeds may have evolved because they were more mobile over increasingly rugged rift terrain, and freer to use their hands to carry young and harvest food in the diverse, challenging and geologically active rift environment.

## **Chapter 6 Future Directions and Summary**

### **6.1 Prospects for Observing Absolute Sea Level Change and Coastal Subsidence with GPS**

Global sea level change and coastal subsidence have important social and economical impact. Precise GPS observations can be used to investigate the problems by directly measuring the motion of land surface in a global geocentric reference frame.

#### **6.1.1 Absolute Sea Level Change**

There is growing appreciation that global surface temperatures may be rising as a result of increased atmospheric CO<sub>2</sub> and other gases of anthropogenic origin. One consequence of this warming may be sea level rise, with important long-term consequences for low-lying coastal regions around the world. Global warming, and hence global sea level rise, may have accelerated during the past few decades, as the concentration of greenhouse gases has markedly increased. There has also been speculation that rapid melting of the unstable West Antarctic ice sheet could lead to catastrophic rise in global sea level on the order of several meters over a few centuries [Oerlemans, 1989; Alley and Whillans, 1991]. During the last interglacial (about 120 ky ago) global mean sea level may have been 5-6 m higher than today with global temperature only a few degrees higher. People are eager to know how much sea level will change in the next several hundred years, and its possible relation with human activity or

natural causes.

In the past hundred years or so, tide gauges have been used as the most direct way to estimate changes in sea level. These instruments can be considered as yard sticks mounted on a pier, with a mechanism to damp out wave motions and other short term variations, and recording devices to automate the data collection process. Most recent models of global eustatic sea level rise are based on tide gauge data, and suggest a rate of  $\sim 1.6 \pm 0.6$  mm/yr [e.g., *Barnett*, 1990; *Trupin and Wahr*, 1990; *Douglas*, 1991; *Peltier and Tushingham*, 1991], with no significant acceleration [*Douglas*, 1992].

Unfortunately, there is considerable uncertainty about even the present rate of sea level rise. The major problems are the contamination of tide gauge data by vertical land movements and the geographical bias in the distribution of the usable tide-gauge data. There are a variety of local and regional processes that could conceivably corrupt local relative sea level (RSL) measurements or corrupt the interpretation of these measurements in terms of secular absolute sea level change (relative to earth's center of mass). It is well established that sea level trends obtained from tide gauge records shorter than about 50-60 years strongly reflect inter-decadal sea level variation. However, trends from even the longest records may show a large scatter, some of which may arise from vertical crustal movements at tide gauge sites.

To convert a measurement of relative sea level change to absolute sea level change, it is necessary to measure the motion of the pier relative to the center of mass of the earth, and subtract this motion from the measurement of relative sea level change recorded by the tide gauge. Piers may rise or sink relative to the center of mass of the

earth because they are built on poorly compacted material, or petroleum, natural gas or ground water extraction is going on nearby. Second, the region may be rising or sinking due to tectonic effects, for example isostatic rebound associated with erosion, or plate interaction near a subduction zone. Third, the region may be slowly adjusting up or down due to post-glacial rebound (PGR), which is detailed in Chapter 4. Different estimates of global sea level change may arise also from different treatments (models) of PGR.

#### 6.1.2 Coastal Land Subsidence in the Mississippi Delta Area

Land loss due to relative sea level rise is pervasive in low slope coastal areas, like the Mississippi delta area, and is aggravated by high levels of local subsidence. Regional subsidence and river modifications can have far greater impact on the relative mean sea level of most deltas than global sea level rise. Subsidence should also be suspected near large cities on river plains or deltas due to sediment compaction, and at sites where fluid withdrawal is significant. The primary factors are rapid relative sea level rise induced by delta-plain subsidence and a deficit of terrigenous wetland sediment. Because of tremendous loss of wetlands and increased incidence of upland flooding, subsidence in the Mississippi River delta has become a major issue. It appears to be caused by various natural and human-induced processes, including groundwater withdrawal, hydrocarbon extraction, river diversion, and sedimentation erosion processes. Because of the low slope of coastal areas in this region, these processes lead to abnormally high rates of land loss in Louisiana and Texas. The Mississippi delta plain is experiencing the most severe land loss and barrier island erosion in North America. In Louisiana alone, the current rate of coastal

and wetland loss is estimated at more than 100 km<sup>2</sup> per year. Two tide gauge stations, Eugene Island and Bayou Rigaud, have been reporting from the 1930s to present and they indicate an increase in rate of subsidence beginning about 1960 [Penland and Ramsey, 1990]. Understanding and mitigating these effects is crucial to the state's economy.

The long term pattern of subsidence in the northern Gulf coastal region is due to a combination of eustatic sea level change, sediment compaction, superimposed by geosynclinal (tectonic) downwarping (sharp differential movements across coastal slump fault systems), and local subsidence near several cities. The challenge here is to directly measure the land subsidence component (which can only be inferred from tide gauge data) and to separate out the various causes of subsidence (which cannot be done at all with tide gauge data). GPS is an excellent way to do this.

### 6.1.3 Preliminary Results from GPS Network for Measurement of Absolute Sea Level Change and Coastal Subsidence

Starting at the end of 1995, we analyzed GPS data from US Coast Guard beacon sites (now 13 sites, Table 6.1, Figure 6.1) in the Southeastern U.S. We now have 1.2 to 2.5 years of data from permanent sites in this region. The site velocities and errors are listed in Table 6.1. Among the eight coastal sites that have time series greater than 2.0 years, seven sites show subsidence, although only one of these (EKY1) is significant at the 95% confidence level (Table 6.1).

Because of time-correlated noise (Chapter 3), the velocity uncertainties are still large, especially for the vertical component which is critical for the tide gauge calibration.

Based on the analysis of GPS noise in Chapter 3, I predict that about 10 years of GPS data with the present quality may be required to achieve accuracy of  $\pm 1$  mm/yr in the vertical component, which is needed to calibrate the tide gauge data. There is also some evidence that the power-law dependence of time-correlated noise in Equation (3.1) may not extend to very low frequency [Langbein, 1998], i.e. the noise may be less correlated below some frequency. If such a power roll-off at low frequencies occurs for GPS, it may be possible to achieve  $\pm 1$  mm/yr in less than 10 years. On the other hand, it will probably take 10 years to document such a roll-off in GPS time series.

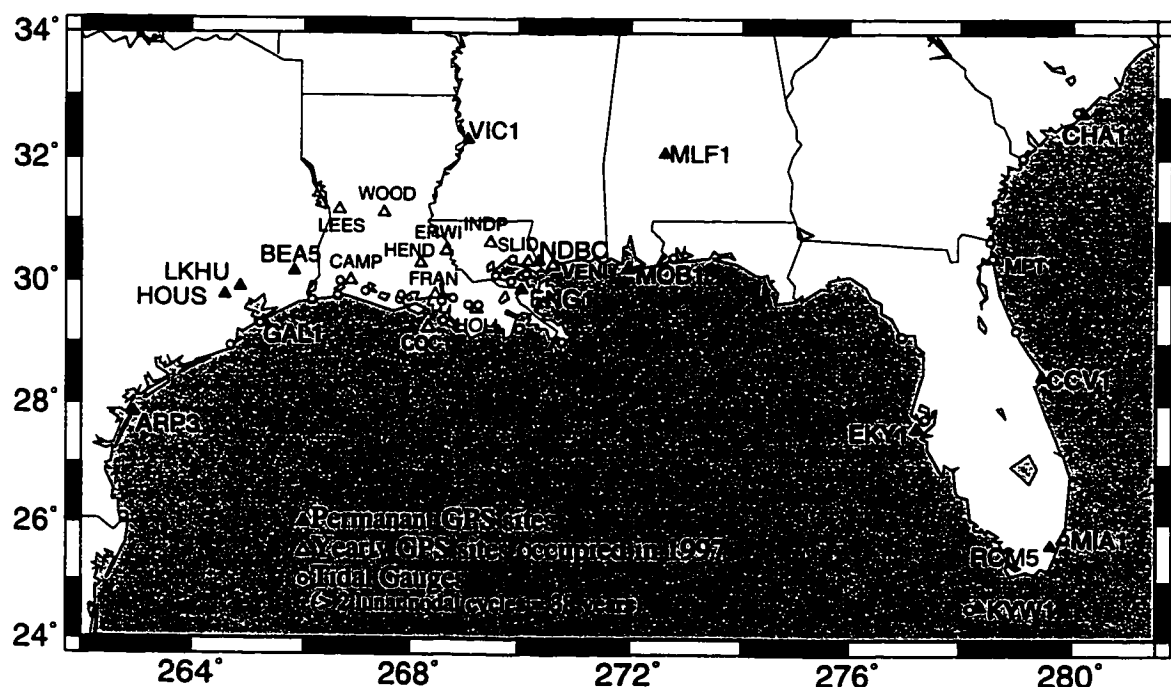


Figure 6.1 GPS sites and tide gauges in the Southeastern U.S.

Table 6.1 North, East and Vertical Velocities and Errors of Permanent GPS Sites

Site	Span	$V_n$	rms	$\sigma_n^w$	$\sigma_n^{wf}$	$V_e$	rms	$\sigma_e^w$	$\sigma_e^{wf}$	$V_v$	rms	$\sigma_v^w$	$\sigma_v^{wf}$
ARP3	2.1	-7.1	3.6	0.3	1.5	-11.8	7.2	0.6	2.9	-9.4	13.9	1.0	5.5
BEAS	1.9	-4.0	5.0	0.3	2.2	-3.2	10.6	0.8	4.6	-14.0	21.4	1.5	9.2
CCV1	1.9	-0.1	3.8	0.3	1.7	-14.9	6.4	0.5	2.8	1.5	13.8	1.0	6.0
CHA1	2.3	0.7	3.6	0.3	1.4	-11.1	6.7	0.5	2.6	-1.3	13.1	0.9	4.9
EKY1	2.0	2.0	4.5	0.3	1.9	-61.7	16.1	1.2	6.8	-18.3	14.7	1.1	6.1
ENG1	2.0	-9.1	4.7	0.4	2.0	-16.3	7.3	0.6	3.1	4.3	14.7	1.0	6.1
GAL1	1.9	-3.2	3.5	0.3	1.5	-12.9	6.7	0.5	2.9	-9.9	12.2	0.9	5.3
HOUS	1.2	-5.7	3.9	0.7	2.8	-14.5	8.3	1.7	6.0	-13.3	16.5	3.1	11.8
KYW1	1.2	2.8	4.2	0.6	3.0	-12.0	7.2	1.1	5.1	-8.2	13.6	2.1	9.7
LKHU	2.1	-1.7	4.0	0.3	1.7	-12.6	6.7	0.5	2.8	-8.5	13.7	1.0	5.7
MIA1	2.3	0.9	4.3	0.3	1.6	-11.2	6.7	0.4	2.5	-3.5	13.4	0.9	5.0
MLF1	1.2	-1.1	3.3	0.5	2.4	-15.6	5.8	0.9	4.2	3.5	11.5	1.8	8.3
MOB1	1.8	-1.8	3.7	0.3	1.8	-12.7	6.5	0.6	3.1	-2.0	13.0	1.0	6.1
NDBC	1.2	-1.8	3.6	0.5	2.6	-15.5	6.9	1.0	5.0	0.8	14.0	2.1	10.1
RCMS	2.5	1.5	4.2	0.3	1.3	-6.6	7.2	2.6	0.5	-4.8	13.7	0.9	9.1
VIC1	2.3	-6.7	3.2	0.2	1.2	-13.0	6.3	0.5	2.4	-1.4	12.6	0.9	4.7

Note:  $\sigma^w$  (mm/yr) is estimated from a pure white noise model, while  $\sigma^{wf}$  is estimated from a white plus flicker noise model. Velocities (mm/yr) are in ITRF-96. Spans are in years and rms is in mm.

To complement the existing GPS network, we also set up several GPS sites in the Mississippi delta and Florida. Twelve sites were occupied in 1997 (Figure 6.1, Table 6.2) and are planned for yearly occupation. The 12 sites have been reoccupied with other new sites in 1998. Although velocity estimates of these yearly sites are less accurate than permanent sites, they will yield better spatial resolution, which is important for the coastal subsidence investigation.

Table 6.2 Site Positions and Errors<sup>1</sup> Estimated from GPS Measurements in 1997

Site	Date	Latitude (°)	$\sigma_n$	Longitude (°)	$\sigma_e$	Height (m)	$\sigma_v$
CAMP	97MAR19	30.008997637	4.4	-93.128722218	10.5	-26.7229	24.7
	97MAR20	30.008997633	3.8	-93.128722075	10.3	-26.7207	24.4
	97MAR21	30.008997695	4.1	-93.128722049	12	-26.7190	25.5
COCI	97MAR25	29.260953483	3.7	-90.656621065	11.7	-25.5694	24.2
	97MAR26	29.260953512	3.3	-90.656621272	9.8	-25.5660	20.9
	97MAR27	29.260953507	3.7	-90.656621218	15.3	-25.5861	23.8
ERWI	97MAR21	30.502797477	3.6	-91.317157480	9.8	-21.4225	23.4
	97MAR22	30.502797419	4.1	-91.317157580	10.5	-21.4107	24.4
	97MAR23	30.502797432	4.1	-91.317157523	11	-21.3967	25.2
FRAN	97MAR28	29.801810435	3.4	-91.525515244	9	-25.8522	21.5
	97MAR29	29.801810444	2	-91.525515159	5.7	-25.8797	14.6
	97MAR30	29.801810476	5.2	-91.525515190	15.1	-25.8923	32.4
HEND	97MAR26	30.312627146	8.5	-91.794851513	24.3	-25.1482	40.3
	97APR06	30.312627185	3.3	-91.794851613	9.5	-25.1900	21.6
	97APR13	30.312627122	4	-91.794851133	11.2	-25.1835	23.2
HOLL	97MAR22	29.572419941	3.9	-90.763090587	9.7	-24.1107	22.9
	97MAR23	29.572419952	3.2	-90.763090488	9.4	-24.1057	21.6
	97MAR24	29.572419959	3.4	-90.763090549	10.4	-24.1122	21.7
INDP	97MAR26	30.647172666	3.7	-90.504473593	10.4	-1.3333	20.9
	97MAR27	30.647172661	3.7	-90.504473443	10	-1.3310	21
	97APR04	30.647172645	7.5	-90.504473409	12.3	-1.3789	32.8
LEES	97APR01	31.167571641	2	-93.342207418	5.5	55.4243	13.8
	97APR02	31.167571671	2	-93.342207408	5.4	55.4072	13.7
	97APR03	31.167571653	2.1	-93.342207436	5.7	55.3966	14
	97APR04	31.167571640	2.1	-93.342207541	5.7	55.3993	14.1
	97APR05	31.167571609	2.5	-93.342207636	7	55.3993	17.7
MPT1	97MAR31	30.393275033	3	-81.431332023	9.8	-28.7315	21.1
	97APR01	30.393275028	3.2	-81.431331998	10.4	-28.7395	22
SLID	97MAR23	30.334526447	6.4	-89.826063793	13.8	-21.7123	35.6
	97MAR24	30.334526468	2.3	-89.826063821	7.3	-21.4825	16.7
	97MAR25	30.334526504	3.8	-89.826063847	10.6	-21.7266	29.7
VENI	97APR10	29.280220429	9.8	-89.359511644	17.8	-26.1444	39.6
	97APR11	29.280220736	2.9	-89.359511528	8.1	-26.0287	19.7
	97APR16	29.280220766	4	-89.359511671	9.3	-26.0333	23.5
	97APR17	29.280220769	3	-89.359511551	8	-26.0208	21.9

Site	Date	Latitude (°)	$\sigma_n$	Longitude (°)	$\sigma_e$	Height (m)	$\sigma_v$
WOOD	97APR03	31.130371220	2.2	-92.500269165	6.3	14.6615	15.5
	97APR04	31.130371230	2.1	-92.500269243	6.3	14.6409	15.9
	97APR05	31.130371180	2.4	-92.500269358	7.2	14.6343	17.4

1. One sigma error in mm.
2. Positions are in ITRF-96.

## 6.2 Summary

From the analysis of noise in GPS time series, I found that the noise characteristics of north, east and vertical components can be best modeled by a combination of white noise plus flicker noise. Both white and flicker noise amplitudes increase in the order north, east and vertical. GPS sites in the southern hemisphere are not significantly noisier than sites in northern hemisphere, which indicates that the current GPS orbits and the ITRF global reference frame are well defined in the southern hemisphere. I found that white noise in the vertical component is relatively higher for tropical sites, which may reflect the high water vapor variation in tropical zones. For the 23 GPS sites, which have about 3 years of data, the velocity error may be underestimated by factors of 5-11 if a pure white noise model is assumed. The range of reduced chi-squares in the investigation of North America rigidity also supports the white plus flicker noise model. Velocity error ranges from -45% to 35% of the value predicted for an appropriate model with accurate error estimates. Because of the time-correlated noise GPS measurements, we will need longer time than initially thought to achieve required accuracy for some geophysical studies, for example, absolute sea level change. Short sampling interval is also less efficient if there is time-correlated noise, and has no effect on random walk noise.

Our investigation of North American plate rigidity shows that the residual velocities are zero within 95% error ellipses except WES2 and FLIN. WES2 has had too many antenna changes in the data period. FLIN has only 1.5 years of data. The derived residual velocities do not reflect Post Glacial Rebound, Pacific-North America boundary zone deformation, or relative motion across New Madrid Seismic Zone. The North American plate is likely more rigid than implied by the GPS derived residuals, because velocity magnitude is positively biased by observational error.

The present-day extension rate derived from space geodetic data across the East African Rift is faster than the rate derived from local surveys, which do span the entire rift. However, our result agrees with predictions from magnetic anomaly data over last 3 Ma, which records the full extension. Extension rates over different time periods suggest acceleration since about 5-6 Ma ago. The time coincides with a change in the absolute motion of the African plate.

## APPENDIX

## Acronyms

A-S	Anti-Spoofing
BARD	Bay Area Regional Deformation Network
C/A code	Coarse/Acquisition code
CORS	Continuously Operating Reference Station
DORIS	Doppler Orbitography and Radiopositioning Integrated Satellite System
EDM	Electronic Distance Measuring
GIPSY/OASIS II	GPS Inferred Positioning SYstem/Orbit Analysis and Simulation Software, version 2
GM	Geocentric Gravitational Constant
GPS	Global Positioning System
IAU	International Astronomical Union
IERS	International Earth Rotation Service
IGS	International GPS Service for Geodynamics
ITRF	International Terrestrial Reference Frame
ITRF96	International Terrestrial Reference Frame published in 1996
JPL	Jet Propulsion Lab
MLE	Maximum Likelihood Estimation
NNR-NUVEL1A	No-Net-Rotation NUVEL-1 modified
NOAA	National Oceanic and Atmospheric Administration
NUVEL-1	A plate motion model developed at the Northwestern University
P-code	Precise code
PGR	Post Glacial Rebound
PRN	PseudoRandom Noise
RSL	Relative Sea Level
S/A	Selective Availability
SLR	Satellite Laser Ranging
SRIF	Square-Root Information Filter
SVN	Space Vehicle Number
TAI	International Atomic Time
TCG	Geocentric Coordinate Time
TOPEX	Ocean Topographic Experiment
UM/RSMAS	The University of Miami, Rosenstiel School of Marine and Atmospheric Sciences
UT1	Universal Time
UTC	Universal Time Coordinated
VLBI	Very Long Baseline Interferometry
WVR	Water Vapor Radiometer

## REFERENCES

- Agnew, D.C., The time-domain behavior of power-law noises, *Geophys. Res. Lett.*, 19, 333-336, 1992
- Alley, R. B., and J. M. Whillans, Changes in the west Antarctic ice sheet, *Science*, 254, 959-963, 1991
- Argus, D. F. and M. B. Heflin, Plate motion and crustal deformation estimated with geodetic data from the Global Positioning System, *Geophys. Res. Lett.*, 22, 1973-1976, 1995
- Argus, D. F. and R. G. Gordon, Tests of the rigid-plate hypothesis and bounds on intraplate deformation using geodetic data from Very Long Baseline Interferometry, *J. Geophys. Res.*, 101, 13,555 - 13,572 1996
- Asfaw, L. M., R. Bilham, M. Jackson, P. Mohr, Recent inactivity in African Rift, *Nature*, 357, 447, 1992
- Baker, B. H., L. Williams, J. Miller, F. Fitch, Sequence and geochronology of the Kenya Rift volcanics, *Tectonophys.*, 11, 191-215, 1971
- Barnett, T. P., Recent changes in sea level: a summary. In: *Sea Level Change*, 37-51, National Academy Press, 1990
- Bar-Sever, Y. E., N. I. Bertiger, E. S. Davis, and I. A. Anselmi, Fixing the GPS bad attitude: Modeling GPS satellite yaw during eclipse seasons, *Navigation*, 43, 1, 1996
- Blewitt, G., Advances in Global Positioning System technology for geodynamics investigations: 1978-1992, *AGU Monograph: Crustal Dynamics Project*, 1993
- Blewitt, G., M.B. Heflin, F.H. Webb, U.J. Lindqwister, and R.P. Malla, Global coordinates with centimeter accuracy in the International Terrestrial Reference Frame, *Geophys. Res. Lett.*, 19, 853-856, 1992
- Blewitt, G., Carrier phase ambiguity resolution for the Global Positioning System applied to geodetic baselines upto 200 km, *J. Geophys. Res.*, 94, 10 187- 10 203, 1989
- Boucher, C., Z. Altamimi, M. Feissel and P. Sillard, Results and analysis of the ITRF94, *IERS Technical Note 20*, 313p., 1996
- Boucher, C., ITRF96, <http://lareg.ensg.ign.fr/ITRF/itrf96.html>, 1998

Brain, C. K., The evolution of man in Africa: was it a consequence of Cenozoic cooling, *Ann. Geol. Soc. South Africa*, 84, 1-19, 1981

Brozena, J., Temporal and spatial variability of seafloor spreading processes in the northern South Atlantic, *J. Geophys. Res.*, 91, 497-510, 1986

Burke, K., and J. F. Dewey, Plume-generated triple junctions: Key indicators in applying plate tectonics to old rocks, *J. Geol.*, 81, 406-433, 1973

Cazenave, A., J. Valette, and C. Boucher, Positioning results with DORIS on Spot-2 after first year of mission, *J. Geophys. Res.*, 97, 7109-7119, 1992

Chase, C. G., Plate kinematics: the Americas, East Africa and the rest of the world, *Earth Planet. Sci. Lett.*, 37, 355-368, 1978

Chen, G. and T. Herring, Effects of atmospheric azimuthal asymmetry on the analysis of space geodetic data, *J. Geophys. Res.*, 102, B6, 20 489-20 502, 1997

Chorowicz, J., B. Collet, F. Bonavia, T. Korme, Northwest to north-northwest extension direction in the Ethiopian rift deduced from the orientation of extension structures and fault slip analysis, *Geol. Soc Am. Bull.*, 105, 1560-1570, 1994

Chu, D., Studies in plate kinematics: plate motions in East Africa and a comparison of paleomagnetic methods, Ph.D. thesis, Northwestern University, 150 p., 1995

Darwin, C., The descent of man, and selection in relation to sex (citation from p. 433) John Murray, London, 1871

deMenocal, P. B., Plio-Pleistocene African Climate, *Science*, 270, 53-59, 1995

DeMets, C., R. G. Gordon, D. F. Argus, and S. Stein, Effect of recent revisions to the geomagnetic time scale on estimates of current plate motion, *Geophys. Res. Lett.*, 21, 2191-2194, 1994.

DeMets, C., R. G. Gordon, D. F. Argus, and S. Stein, Current plate motion, *Geophys. J. Int.*, 101, 425-478, 1990

Dixon, J. E., H. Enggel, J. M. Moore, and C. J. Hickson, Volatiles in basaltic glasses from a subglacial volcano in Northern British Columbia: Implications for mantle volatiles and ice sheet thickness, *IAVCEI 1998 Meeting*, Cape Town, South Africa, 1998

Dixon, T. H., A. Mao, M. Bursik, M. Heflin, J. Langbein, R. Stein, F. Webb, Continuous monitoring of surface deformation at Long Valley Caldera with GPS, *J. Geophys. Res.*, 102, 12,017-12,034, 1997a

- Dixon, T. H. and A. Mao, A GPS estimate of relative motion between North and South America, *Geophys. Res. Lett.*, 24, 535-538, 1997b
- Dixon, T. H., A. Mao and S. Stein, How rigid is the stable interior of the North America plate?, *Geophys. Res. Lett.*, 23, 3035-3038, 1996
- Dixon, T. H., F. Farina, A. Mao, M. Bursik, R. Stein and G. Marshall, GPS Monitoring Data for active volcanoes available on Internet, *EOS*, Vol 76, No. 1, 1995
- Dixon, T. H., An introduction to the Global Positioning System and some geological applications, *Reviews of Geophysics*, 29, 249-274, 1991a
- Dixon, T. H., G. Gonzalez, S. M. Lichten, and E. Katsigris, First epoch geodetic measurements with the Global Positioning System across the Northern Caribbean plate boundary zone, *J. Geophys. Res.*, 96, B2, 2397-2415, 1991b
- Dixon, T. H. and S. Kornreich Wolf, Some tests of wet tropospheric calibration for the CASA UNO Global Positioning System experiments, *Geophys. Res. Lett.*, 17, 203-206, 1990
- Dong, D., and Y. Bock, GPS network analysis with phase ambiguity resolution applied to crustal deformation studies in California, *J. Geophys. Res.*, 94, 3949-3966, 1989
- Douglas, B. C, Global sea level acceleration, *J. Geophys. Res.*, 97, 12 699 - 12 706, 1992
- Douglas, B. C, Global sea level rise, *J. Geophys. Res.*, 96, 6981-6992, 1991
- Ebinger, C. J., T. Yemane, G. Woldegabriel, J. Aronson, R. Walter, Late Eocene-recent volcanism and faulting in the southern main Ethiopian Rift, *J. Geol. Soc.*, 150, 99-108, 1993
- Gomberg, J. and M. Ellis, Topography and tectonics of the central New Madrid seismic zone: Results of numerical experiments using a three-dimensional boundary element program, *J. Geophys. Res.*, 99, 20299-20310, 1994
- Goter, G. K., G. P. Thelin, and R. J. Pike, Earthquakes in the conterminous United States (1534-1991), USGS Open-File Report 92-327, 1992
- Gregory, J., The Great Rift Valley, London, John Murray, 405p., 1896
- Hamilton, R., and M. Zoback, Tectonic features of the New Madrid seismic zone from seismic reflection profiles, in F. McKeown and L. Pakiser, eds., Investigations of the

New Madrid Missouri earthquake region, *U.S. Geol. Surv. Prof. Paper 1236-L*, 55-77, 1982

Heflin, M., W. I. Bertiger, G. Blewitt, A. P. Freedman, K. J. Hurst, S. M. Lichten, U. J. Lindqwister, Y. Vigne, F. H. Webb, T. P. Yunck, and J. F. Zumberge, Global geodesy using GPS without fiducial sites, *Geophys. Res. Letters*, Vol. 19, No. 2, 131-134, 1992

Heflin, M., <http://sideshow.jpl.nasa.gov/mbh/series.html>, 1997

Hendrie, D. N. Kusznir, C. Morley, C. Ebinger, Cenozoic extension in northern Kenya: quantitative model of rift basin development in the Turkana region, *Tectonophysics*, 236, 409-438, 1994

Herrmann, R. B., Surface wave focal mechanisms for eastern North America earthquakes with tectonic implications, *J. Geophys. Res.*, 84, 3543-3551, 1979

Hildebrand, T., M. Kane and J. Hendricks, Magnetic basement in the Upper Mississippi embayment region - a preliminary report, in F. McKeown and L. Pakiser, eds., *Investigations of the New Madrid Missouri earthquake region, U.S. Geol. Surv. Prof. Paper 1236-L*, 39-53, 1982

Himes, L., W. Stauder and R. Hermann, Indication of active faults in the New Madrid seismic zone from precise location of hypocenters, *Seismol. Res. Lett.*, 59, 123-131, 1988

Jefferson, D. C., M. B. Heflin, M. M. Watkins and F. H. Webb, J. F. Zumberge, Y. E. Bar-Saver, Jet Propulsion Laboratory IGS analysis center report, *International GPS Service for Geodynamics (IGS) 1996 Annual Report*, 183-192, 1997

Jestin, F., P. Huchon, and J. M. Gaulier, The Somalia plate and the East African Rift system: present day kinematics, *Geophys. J. Int.*, 116, 1994

Joffe, S., and Z. Garfunkel, Plate kinematics of the circum Red Sea-a re-evaluation, *Tectonophysics*, 141, 5-32, 1987

Johnson, H. O. and D. C. Agnew, Monument motion and measurements of crustal velocities, *Geophys. Res. Lett.*, 22, 2905-2908, 1995

Johnson, H. O. and F. K. Wyatt, Geodetic network design for fault mechanics studies, *Manuscripta Geodetica*, 19, 309-323, 1994

Kennett, J. P., A review of polar climatic evolution during the Neogene, based on the marine sediment record, in E. Vrba et al., *Paleoclimate and evolution, with emphasis on human origins*, 331-355, Yale Univ. Press, 1995

- King, N. E., J. L. Svart, E. B. Fogelman, W. K. Gross, K. W. Clark, G. D. Hamilton, C. H. Stiffler, and J. M. Sutton, Continuous GPS observations across the Hayward fault, California, 1991-1994, *J. Geophys. Res.*, 100, 20 271- 20 284, 1995
- Koch, K.R., Maximum likelihood estimate of variance components, *Bull. Geod.*, Vol. 60, 329-338, 1986
- Kouba, J. and Y. Mireault, Analysis coordinator report, *International GPS Service for Geodynamics (IGS) 1996 Annual Report*, 55-100, 1997
- Langbein, J., personal communication, 1998
- Langbein, J. and H. Johnson, Correlated errors in geodetic time series: Implications for time-dependent deformation, *J. Geophys. Res.*, 102, B1, 591-604, 1997
- Langley, R., gopher://unbmsvn.csd.unb.ca:1570/1EXEC%3aCANSSPACE, 1997
- Larson, K. M., J. T. Freymueller, and S. Philipsen, Global plate velocities from the Global Positioning System, *J. Geophys. Res.*, 102, 9961-9981, 1997
- LePichon, X. and J. Francheteau, A plate tectonic analysis of the Red Sea Gulf of Aden area, *Tectonophys.*, 46, 369-406, 1978
- Leakey, M. G., C. S. Feibel, I. McDougall, A. Walker, New four-million year hominid species from Kanapoi and Allia Bay, Kenya, *Nature*, 376, 565-571, 1995
- Leffler, L., S. Stein, A. Mao, T. Dixon, M. A. Ellis, L. Ocola, and I. S. Sacks, Constraints on present-day shortening rate across the central eastern Andes from GPS measurements, *Geophys. Res. Lett.*, 24, 1031-1034, 1997
- Lichten, S. M., Estimation and filtering for high precision GPS applications, *Man. Geod.*, 15, 159-176, 1990
- Liu, L., M. Zoback and P. Segall, Rapid intraplate strain accumulation in the New Madrid seismic zone, *Science*, 257, 1666-1669, 1992
- Lomb, N.R., *Astrophysics and Space Science*, 39, 447-462, 1976
- Mao, A., C. G. A. Harrison and T. H. Dixon, Noise in GPS time series, submitted to *J. Geophys. Res.*, 1998a
- Mao, A., T. H. Dixon and S. Stein, Present-day motion across the East African rift, submitted to *Nature*, 1998b

- Mao, A., C. G. A. Harrison and T. Dixon, Monument stability of permanent GPS stations and tide gauges, *Eos Trans. AGU*, 77(76), Fall Meet. Suppl., F153, 1996
- Mao, A., T. Dixon and F. Farina, Monitoring active volcanoes in near-real time with GPS, AGU 1994 Fall Meeting, *EOS*, Vol. 75, No. 44 supplement, p164, 1994
- McCarthy, IERS Conventions 1996, *IERS Technical Note No. 21*, 1996
- McConnell, R. B. A resurgent taphrogenic lineament of Precambrian origin in eastern Africa, *J. Geol. Soc. London*, 137, 483-489, 1980
- McKenzie, D. P., D. Davies and P. Molnar, Plate tectonics, the Red Sea and East Africa, *Nature*, 226, 243-248, 1970
- Mitrovica, J. X. and A. M. Forte, Radial profile of mantle viscosity: Results from the joint inversion of convection and postglacial rebound observables, *Geophys. J. In.*, 102, 2751-2769, 1997
- Mohr, P., A. Girnius, J. Rolff, Present-day strain rates at the northern end of the Ethiopian rift valley, *Tectonophys.*, 44, 141-160, 1978
- Morley, C. K., Variable extension in Lake Tanganyika, *Tectonics*, 7, 785-801, 1988
- Niell, A., personal communication, 1998
- Niell A. E., P. Elosegui, J. L. Davis, I. I. Shapiro, R. T. K. Jaldehag and J. M. Johanson, Reduction of signal multipath effects on GPS estimates of site position, *EOS*, Vol. 75, N0.44, Supplement, p171, 1994
- Norabuena, E., L. Leffler-Griffin, A. Mao, T. Dixon, S. Stein, I. Sacks, L. Ocola, M. Ellis, Space geodetic observations of Nazca-South America convergence along the Central Andes, *Science*, 279, 358-362, 1998
- Nuttli, O., Damaging earthquakes of the central Mississippi Valley, in F. McKeown and L. Pakiser, eds., Investigations of the New Madrid Missouri earthquake region, *U.S. Geol. Surv. Prof. Paper 1236-L*, 15-20, 1982
- Oerlemans, J. A projection of future sea level, *Climate Change*, 15, 151-174, 1989
- Page, R. A., G. Plafker and H. Pulpar, Block rotation in east central Alaska: a framework for evaluating earthquake potential, *Geology*, 23, 629-632, 1995
- Peltier, W. R., A space geodetic target for mantle viscosity discrimination: Horizontal motions induced by glacial isostatic adjustment, *Geophys. Res. Let.*, 25, 543-546, 1998

- Peltier, W. R., VLBI baseline variations from the ICE-4G model of postglacial rebound, *Geophys. Res. Lett.*, 22, 465-468, 1995
- Peltier, W. R., and A. M. Tushingham, Influence of glacial isostatic adjustment in tide gauge measurements of secular sea level change, *J. Geophys. Res.*, 96, 6779-6796, 1991
- Penland, S. and K. Ramsey, Relative sea-level rise in Louisiana and the Gulf of Mexico: 1908 - 1988, *J. Coastal Res.*, vol. 6, no. 2, 323 - 342, 1990
- Pollitz, F. F. Two stage model of African absolute motion during the last 30 million years, *Tectonophys.*, 194, 91-106, 1991
- Press, W.H., B.P. Flannery, S.A. Teukolsky, and W.T. Vetterling, *Numerical Recipes*, Cambridge University Press, 818p, 1992
- Rabbel, W. and H. Schuh, The influence of atmospheric loading on VLBI experiments, *J. Geophys.*, 59, 164-170, 1986
- Robaudo, S. and C. G. A. Harrison, Plate tectonics from SLR and VLBI data, in D. Smith and D. Turcotte, eds., *Contributions of Space Geodesy and Geodynamics, Am. Geophys. U. Geodynamics Series*, 23, 51-71, 1993
- Robbins, J., D. Smith and C. Ma, Horizontal crustal deformation and large scale plate motions inferred from space geodetic techniques, in D. Smith and D. Turcotte, eds., *Contributions of Space Geodesy and Geodynamics, Am. Geophys. U. Geodynamics Series*, 23, 21-36, 1993
- Rocken, C., T. VanHove, and R. Ware, Near real-time GPS sensing of atmospheric water vapor, *Geophys. Res. Lett.*, 24, 3221-3224, 1997
- Rosendahl, B. R., E. Kilember and K. Kaczmarick, Comparison of the Tanganyika, Malawi, Ruka and Turkana rift zones from analyses of seismic data, *Tectonophysics*, 213, 235-256, 1992
- Russ, D. P., Style and significance of surface deformation in the vicinity of New Madrid, in F. McKeown and L. Pakiser, eds., *Investigations of the New Madrid Missouri earthquake region, U.S. Geol. Surv. Prof. Paper 1236-L*, 95-114, 1982
- Ryan, J. W., T. A. Clark, C. Ma, D. Gordon, D. Caprette, W. Hinwich, Global scale tectonic motions measured with CDP VLBI data, in D. Smith and D. Turcotte, eds., *Contribution of Space Geodesy to Geodynamics, AGU Geodynamics Ser.*, 23, 37-49, 1993

Scarge, J.D., *Astrophysical Journal*, 263, 835-853, 1982

Schroeder, M., *Fractals, Chaos, Power Laws*, W.H. Freeman and Company, 429p, 1991

Scott, D. L., B. Rosendahl, C. Burgess, S. Sander, Comment on "Variable extension in Lake Tanganyika", *Tectonics*, 8, 647-650, 1989

Seeber, Guenter, *Satellite Geodesy*, W. de Gruyter, 531 p., 1993

Semaw, S., P. Renne, J. Harris, C. Feibel, R. Bernor, N. Fesseha, K. Mowbray, 2.5 million year old stone tools from Gona, Ethiopia, *Nature*, 385, 333-336, 1997

Shudofsky, G. N., Source mechanisms and focal depths of East African earthquakes using Rayleigh wave dispersion and body wave splitting, *Geophys. J. R. Aston. Soc.*, 563-576, 1984

Smith, D. E., R. Kolenkiewicz, P. J. Dunn, J. W. Robbins, M. H. Torrence, S. M. Klosko, R. G. Williamson, E. C. Pavlis, N. B. Douglas, and S. K. Fricke, Tectonic motion and deformation from satellite laser ranging to LAGEOS, *J. Geophys. Res.*, 95, 22,013-22,041, 1990

Soudarin, L., personal communication, 1997

Stein, S. and R. Gordon, Statistical tests of additional plate boundaries from plate motion inversions, *Earth Planet. Sci. Lett.*, 69, 401-412, 1984

Trupin, A. and J. Wahr, Spectroscopic analyses of global tide gauge sea level data, *Geophys. J. Int.*, 100, 441-453, 1990

vanDam Tonie M., G. Blewitt, M. Heflin, Atmospheric pressure loading effects on Global Positioning System coordinate determinations, *J. Geophys. Res.*, vol. 99, No. B12, 23,939-23,295, 1994

Vigue, Y., S. M. Lichten, G. Blewitt, M. B. Heflin, and P. R. Malla, Precise determination of Earth's center of mass using measurements from the Global Positioning System, *Geophys. Res. Lett.*, 19, 1487-1490, 1992

Vrba, E., Late Pliocene climatic events and hominid evolution, in Evolutionary history of the robust australopithicines, ed F. E. Grine, Aldine, New York, 405-426, 1988

Ward, S., Pacific-North America plate motion: new results from Very Long Baseline Interferometry, *J. Geophys. Res.*, 95, 21 965-21 981, 1990

Ware, R. C. Alber, C. Rocken, and F. Solheim, Sensing integrated water vapor along GPS ray paths, *Geophys. Res. Lett.*, 24, 417-420, 1997

Wdowinski, S., Y. Bock, J. Zhang, P. Fang, and J. Genrich, Southern California Permanent GPS Geodetic Array: Spatial filtering of daily positions for estimating coseismic and postseismic displacements induced by the 1992 Landers earthquake, *J. Geophys. Res.*, 102, B8, 18 057-18 070, 1997

Webb, F., J. Zumberge, An Introduction to GIPSY/OASIS-II, Jet Propulsion Laboratory, California, 1993

Weber, J., S. Stein, and J. F. Engeln, Estimation of strain accumulation in the New Madrid seismic zone from GPS geodesy, to be submitted to *Tectonics*, 1996

Wessel, P., and W. H. F. Smith, New version of the Generic Mapping Tools released, *EOS*, vol 16, pp. 329, 1995

Yunck, T. P., S. C. Wu, S. M. Lichten, and W. I. Bertiger, Toward centimeter orbit determination and millimeter geodesy with GPS, *Proc. 5th Int. Geod. Symp. Satellite Positioning*, vol. 1, 272-281, Las Cruzes, 1989

Zhang, J., Y. Bock, H. Johnson, P. Fang, S. Williams, J. Genrich, S. Wdowinski, and J. Behr, Southern California Permanent GPS Geodetic Array: Error analysis of daily position estimates and site velocities, *J. Geophys. Res.*, 102, B8, 18 035-18 055, 1997

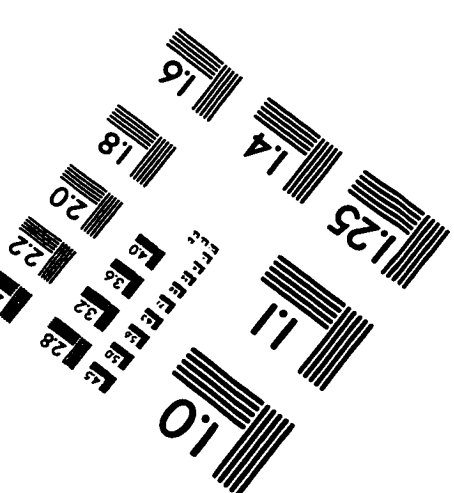
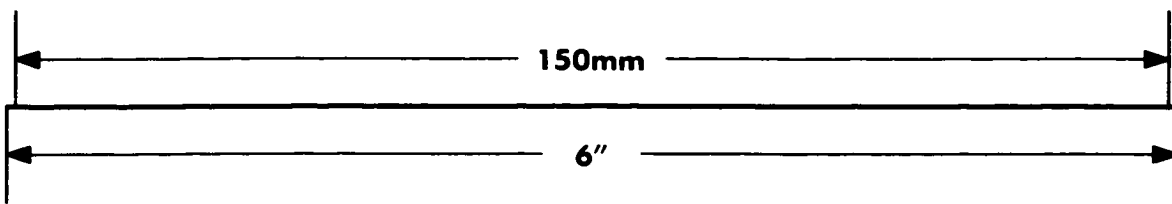
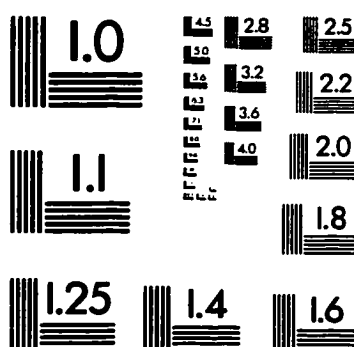
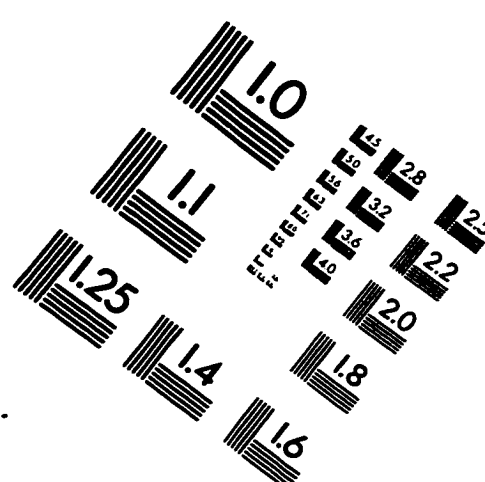
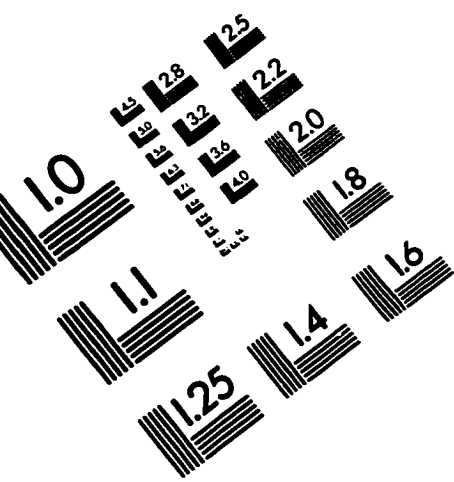
Zoback, M. L., and 28 others, Global pattern of tectonic stress, *Nature*, 341, 291-298, 1989

Zumberge, J. F., M. B. Heflin, D. C. Jefferson, M. M. Watkins, and F. H. Webb, Precise positioning for the efficient and robust analysis of GPS data from large network, *J. Geophys. Res.*, 102, 5005-5017, 1997

## **VITA**

Ailin Mao was born in a village in Zhejiang Province, P. R. China, on September 9, 1965. His parents are Peide Mao and Yongbao Zhu. He is the second son in a family of two boys. He spent the first 14 years of his life in the village, about 110 kilometers south of Shanghai. He first received his education at Xingsheng Elementary and Junior Middle School. In the Spring of 1979, he transferred to the Jiashuang County First High School. In September 1982, he was admitted to the Tongji University in Shanghai, from which he graduated with honors in Surveying Engineering in July 1987 with a Bachelor of Science. In September 1987, he was admitted to the graduate program at Shanghai Astronomical Observatory, Chinese Academy of Sciences, with waiver of the national graduate entry examination. After being granted a Master of Science in Astrometry and Celestial Dynamics in June 1990, he continued to work in Shanghai Astronomical Observatory for three years. In August 1993, he came to USA to pursue a Ph.D. at the Rosenstiel School of Marine and Atmospheric Sciences, University of Miami, Coral Gables, Florida. He was granted a Ph.D. in Marine Geology and Geophysics in June 1998.

# IMAGE EVALUATION TEST TARGET (QA-3)



APPLIED IMAGE, Inc.  
1653 East Main Street  
Rochester, NY 14609 USA  
Phone: 716/482-0300  
Fax: 716/288-5989

© 1993, Applied Image, Inc., All Rights Reserved

